Molecular dynamics studies on the role of chain stiffness in glassy behavior of linear and ring polymers

Shota Goto

MARCH 2025

Molecular dynamics studies on the role of chain stiffness in glassy behavior of linear and ring polymers

A dissertation submitted to

THE GRADUATE SCHOOL OF ENGINEERING SCIENCE

OSAKA UNIVERSITY

in partial fullfillment of the requirements for the degree of

DOCTOR OF PHILOSOPHY IN SCIENCE

by

Shota Goto

MARCH 2025

Abstract

The dynamics of polymers are governed by the chain structure, such as chain length, stiffness, and topology. Although "entanglements" is a key concept for understanding the dynamics of polymer melts, their pictures are much different between linear and ring polymers. Therefore, "topological constraints" are used as a more general expression for the entanglements in polymers independent of the chain topology. Interestingly, "topological glasses" are expected to be formed in ring polymer melts with sufficiently long chain length at the temperature well above the glass transition temperature T_{g}. It should be noted that the chain stiffness will increase the topological constraints in polymers. In this study, we focus on the glassiness of polymers and investigate the effects of chain stiffness on the glassiness both in linear and ring polymers.

Chapter 1 provides the general introduction of the glassiness of polymers and the topological effect on entanglements.

In Chapter 2, we characterized the effects of chain stiffness on the glassiness of linear polymer glasses using molecular dynamics simulations. Amorphous materials exhibit peculiar mechanical and vibrational properties, including non-affine elastic responses and excess vibrational states, *i.e.*, the so-called boson peak. For polymer glasses, these properties are considered to be affected by the stiffness of the constituent polymer chains. Here, we demonstrate the insensitivity of elastic heterogeneity by directly measuring the local shear modulus distribution. We conclude that the chain stiffness does not alter the spatial heterogeneity of the local shear modulus distribution, which yields vibrational and acoustic properties that are controlled solely by the global shear modulus of a polymer glass.

In Chapter 3, we investigate the effect of chain topology on the dynamics of polymer melts with varying chain length. Thus, Rouse mode analysis is performed and compared between ring and linear polymers. Rouse-like behavior is observed in ring polymers by quantifying the chain length dependence of the Rouse relaxation time, whereas a crossover from Rouse to reptation behavior is observed in linear polymers. Furthermore, the non-Gaussian parameters of the monomer bead displacement and chain center-of-mass displacement are analyzed. It is found that the non-Gaussianity

of ring polymers is remarkably suppressed with slight growth for the center-of-mass dynamics at long chain length, which is in contrast to the growth in linear polymers both for the monomer bead and center-of-mass dynamics.

In Chapter 4, we investigate the effect of chain stiffness and monomer density on static and dynamic behaviors of ring polymer solutions. We introduce a bond-breaking method to analyze the local structure and its relaxation, which characterize the relationship between the monomer density dependence of the radius of gyration and the rearrangement of center-of-mass in ring polymers with varying stiffness. Our results demonstrate that the dynamic heterogeneity of rearrangements is coupled with the non-Gaussianity in ring polymer melts, highlighting the importance of bond-breaking method in determining the inter-molecular dynamics of ring polymer melts.

In Chapter 5, we used persistent homology to quantify threading structures of ring polymers and elucidate mechanisms behind topological glasses. Using coordination data from coarse-grained molecular dynamics simulations, we analyzed the topology of the union of virtual spheres centered on each monomer or center of mass. As the radius of each sphere increases, the corresponding points connect, giving rise to topological entities such as edges, loops, and facets. We then analyzed how the number of loops per ring chain and penetrated loops varies with sphere radius, focusing on the effects of chain stiffness and density. The results reveal that loops are larger in stiff ring chains, whereas flexible ring chains do not generate sufficiently large loops to establish a threading structure. The stiffness of ring polymer plays a significant role in the formation of topological glasses in ring polymers.

The general conclusions are presented in Chapter 6.

Contents

Chapter 1

General Introduction

1.1 Topological constraints in polymers

Polymers are ubiquitous in nature and play a significant role in our daily lives, being essential for the production of plastics, fibers, and rubbers. The physical properties, such as the diffusion coefficient and elastic viscosity of polymers, are not only crucial for industrial applications but also play a vital role in biological systems.

The dynamics of polymers are governed by topological constraints (TCs), because of which the viscosity and relaxation time increase drastically with increasing degree of polymerization. Linear polymers in dilute solutions or melts can be described as having conformations of random walks, so-called Gaussian chain. The dynamics of linear polymers are well described by Rouse and Zimm models in dilute solutions and the reptation model in melts [1, 2]. In reptation model, linear polymer chains are confined in tube-like regions by surrounding chains, and the relaxation time is determined by the time required for a Rouse chain to escape from the tube as shown in Fig. 1.1. Recently, another type of topological constraints in polymer has been proposed, namely, ring polymer melts without chain ends [3–7]. Despite extensive research, a thorough understanding of TCs in ring polymer melts remains a significant challenge in polymer physics [8–32] .

Figure 1.1: A conceptual sketch of entanglement in linear polymers. The reptation model describes the dynamics of linear polymers in melts as that the chain highlighted in red is confined in tube-like regions along its contour formed by surrounding chains (gray).

1.2 Polymers in solutions or melts

The static properties of polymers in solutions or melts are often characterized by the Flory exponent ν, which describes the scaling relationship between the radius of gyration R_g and the degree of polymerization N: $R_g \propto N^{\nu}$. The conformations of linear polymers in dilute solutions are well described with self-avoiding walks, which have the Flory exponent $\nu \approx 0.588$ in three dimensions. In melts, the excluded volume interactions between surrounding chains are screened out, resulting in the Flory exponent $\nu = 0.5$. In dilute solution of good solvent, ring polymers behave similarly to linear polymers to take extended conformations compared to Gaussian chain, which have the Flory exponent $\nu = 0.588$. This is concluded both from the theories [33–40] and experiments [41, 42]. It should be noted that nonphantom ring polymers, even in the absence of excluded-volume interactions, adopt swollen conformations when isolated. This finding suggests that TCs, which prevent rings from becoming knotted or concatenated, effectively generate a repulsive interaction between their segments.

In melts, while ring polymers are approximately described as the Gaussian chains at short chain length N, TCs become more significant and complex as the chain length N increases. The lattice animal model is often used to describe the ring polymer in solutions or gels [43,44]. Fig. 1.2 shows

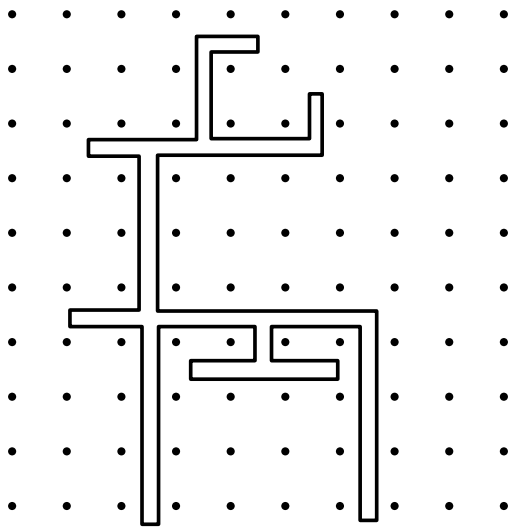

Figure 1.2: A tree-like lattice animal in two dimensions corresponding to a ring polymer in a regularly fixed obstacles.

a schematic of the lattice animal in two dimensions. The ring polymer, due to TCs such as non-crossing conditions, can enclose none of the obstacles, leading to double-folded conformations. This model concludes that the Flory exponent $\nu = 1/3$ for long ring polymers [43,45,46]. Grosberg *et. al.* also proposed the same value of $\nu = 1/3$ from the hypothesis that the equilibrium conformations of ring polymers are the so-called crumpled globule, which each subchain is internally condensed, resulting in a polymer backbone that exhibits self-similarity with a fractal dimension of 3 [47]. Cates and Deutch proposed a conjecture on the scaling exponent $\nu = 2/5$ for ring polymers in melts based on the Flory-type mean field theory [3]. This value is the intermediate between the collapsed conformations ($\nu = 1/3$) and the Gaussian chain ($\nu = 1/2$).

While many theoretical predictions including those not shown above have been suggested for ring polymer melts [35, 37–40, 48], the Flory exponent is reported as $\nu \sim 0.36$ by recent molecular dynamics (MD) simulations with the range of $N \lesssim 5000$ [29, 49], which is consistent with the experimental results [22]. There are predictions, however, that the Flory exponent ν is expected to be 1/3 at the large chain length N, which even the static behavior of ring polymers has not been established yet. Halverson *et. al.* reported the both dynamic and static properties of ring polymer melts with the range of $100 \leq N \leq 1600$ using MD simulations [10, 11]. They found that ring poly-

mers diffuse approximately 10 times faster than linear polymers with the same chain length N and the power law exponent of the diffusion coefficient D of center of mass as a function of N is about -2.4 at long chain length N, which seems consistent with linear polymers in melts. Furthermore, the stress relaxation time of ring polymers does not show the plateau at the intermediate time scale even at the longest chain length $N = 1600$. These results, while the authors maintain that further investigation is required, suggest a decoupling between the translational motion and stress relaxation for the rings, which is probably due to the crumpled globule conformations.

The lattice animal model can also predict the dynamics of ring polymers in a gel [4, 50]. The main idea of this model is that the smaller loops diffuse along larger loops in a self-similar way. It predicts that the longest relaxation time of a non-concatenated ring polymer with N Kuhn monomers is proportional to $N^{5/2}$ and the diffusion coefficient is proportional to N^{-2}. Ge *et. al.* developed the theory based on concepts of self-similar conformations and dynamics of ring polymers in melts [17]. They found that the longest relaxation time as a function of N is proportional to $N^{7/3}$ and the diffusion coefficient is proportional to $N^{-5/3}$, which is resulted from the compact conformations with fractal dimension of 3, so-called a fractal loopy globule, and the conjecture that the overlap parameter of subsections of rings on all length scales is the same and equal to the Kavassalis–Noolandi number $O_{\mathrm{KN}} \approx 10 - 20$ [51–53].

There are several approaches to describe the dynamics of ring polymers in melts based on the analogy with soft-colloidal systems. Sakaue introduced the topological volume fraction to characterize TCs by the competition between inter-ring non-concatenation constraints and the intra-ring constraints involved with self-knotting [48, 54, 55]. It is predicted that the cross-over from the Gaussian chains $\nu = 1/2$ to the crumpled globule $\nu = 1/3$ and the flory exponent $\nu = 2/5$ in the intermediate regimes. Furthermore, the scaling factor of the diffusion coefficient and relaxation time are found, which are in good agreement with the simulation results. Mei *et. al.* construct a microscopic theory for the long-time center-of-mass diffusion constant and intermediate-time non-Fickian transport in dense solutions and melts of ring polymers [20, 20, 23] , based on the polymer reference interaction site model theory [56] and mode-coupling theory [57–59].

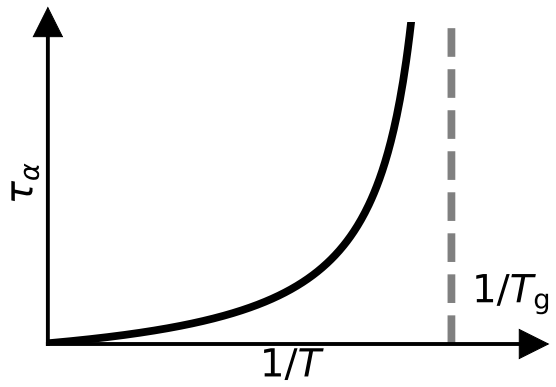

Figure 1.3: Sketch of the non-Arrhenius temperature dependence of the α-relaxation time τ_α as function of the inverse temperature $1/T$.

1.3 Polymer glasses

Polymer glasses are also an important subject in polymer physics [60]. When the temperature of a liquid is continuously lowered while avoiding crystallization, it undergoes a glass transition via a supercooled state. Unlike crystalline solids, glasses posseses a disordered microscopic structures similar to that of liquids. As the temperature approches T_g, the dynamics of supercooled liquids slow down drastically, as illustrated by the tempareture dependence of the α-relaxation time τ_α in Fig. 1.3. This behavior is one of the great mysteries of the glass transition and is characterized by the non-Arrhenius temperature dependence that is well fit by empirical Vogel–Fulcher–Tammann (VFT) equation:

$$\tau_\alpha = \tau_0 \exp\left(\frac{A}{T - T_0}\right), \tag{1.1}$$

where τ_0, A and T_0 are the fitting parameters that depend on the material. The temperature T_0 at which the divergence occurs is called the Vogel temperature and typically located 30 – 50 K below T_g.

Interestingly, despite their long-chain molecular structure, polymer glasses exhibit properties similar to those of small-molecule glasses, including a non-Arrhenius temperature dependence of the α-relaxation time. This is notable given that microscopic structural features are known to play a crucial role in dynamics above T_g. This universality observed across different glass-

forming liquids, including polymers, can be attributed to the packing effect associated with the glass transition occurring at the segmental level in polymers. Thus, the glass transition temperature T_g is independent of the chain length N or its topology such as whether it is linear or ring. However, the chain stiffness, which dependes on the chemical species of monomers, influences thermodynamic properties such as the glass transition temperature T_g and the specific heat.

1.4 Vibrational density of states

The vibrational density of states (vDOS) $g(\omega)$ is the density of vibrational modes of atoms in a solid as a function of frequency ω. Debye model describes the lattice vibrations as phonons and analysically computes the vDOS $g(\omega)$ as

$$g(\omega) = \frac{V}{2\pi^2}\left(\frac{2}{c_T^3} + \frac{1}{c_L^3}\right)^3 \omega^2, \tag{1.2}$$

in three dimensions, where V is the volume of the system and c_T and c_L are the transverse and longitudinal sound velocities, respectively [61]. If the number of particles is N, the vDOS $g(\omega)$ can be normalized as $\int_0^{\omega_D} g(\omega)d\omega = 3N$, where ω_D is the Debye frequency that is the maximum frequency of the phonon modes. Thus, the normalized vDOS $g(\omega)/3N$ can be written as

$$\frac{g(\omega)}{3N} = A_D\omega^2, \tag{1.3}$$

where $A_D = 3/\omega_D^3$ is the Debye lebel. Noting that phonons are bosons, integration of the vDOS $g(\omega)$ over the frequency ω yields the internal energy U and the specific heat C_v, which are proportional to T^4 and T^3, respectively. In glasses, however, there is an excess vibrational modes at low frequency, which is called the Boson peak (BP), and the anomalous thermodynamic behavior at low temperature are related to this BP.

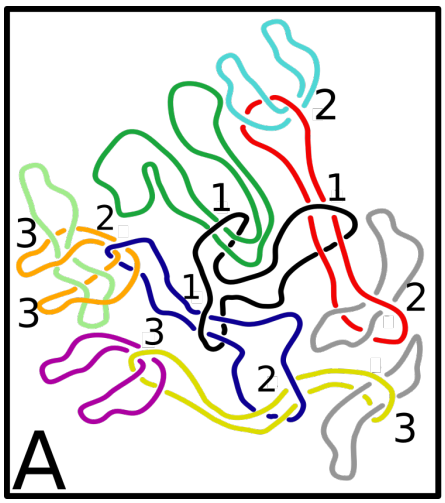

Figure 1.4: A schematic of threading network in ring polymers cited from Ref. [67].

1.5 Topological glasses

Interpenetration of ring polymers, so-called threading, is naively expected to play a crucial role in the dynamics of ring polymers in melts analogous to entanglement in linear polymers. Threading occurs when one ring polymer penetrates the loop of another ring polymer, with the penetrating ring classified as active and the penetrated ring as passive, illustrating the asymmetric and hierarchical nature of the threading network as shown in Fig. 1.4. It has been challenging to quantify and characterize the threading in concentrated solutions of ring polymers especially theoretically, because the topological invariants such as linking number or writhe are not applicable to threading which is not permanent. The several methods quantifying threading have been proposed based on minimal surface [62, 63], geometric analysis [64, 65], and persistent homology [66]. However, the relationship between threading and the dynamics in dense solutions of ring polymers still remains unclear.

Michieletto and Turner reported the glass-like dynamics in ring polymer solutions [68, 69]. They performed pinning MD simulations of ring polymers adopting a slightly sttiffer polymer chain model than the that of Halverson [10, 11] to compute effectively long chain length N. While this model shows the same behavior of the Flory exponent $\nu \approx 1/3$ as Halverson's results, ring polymers

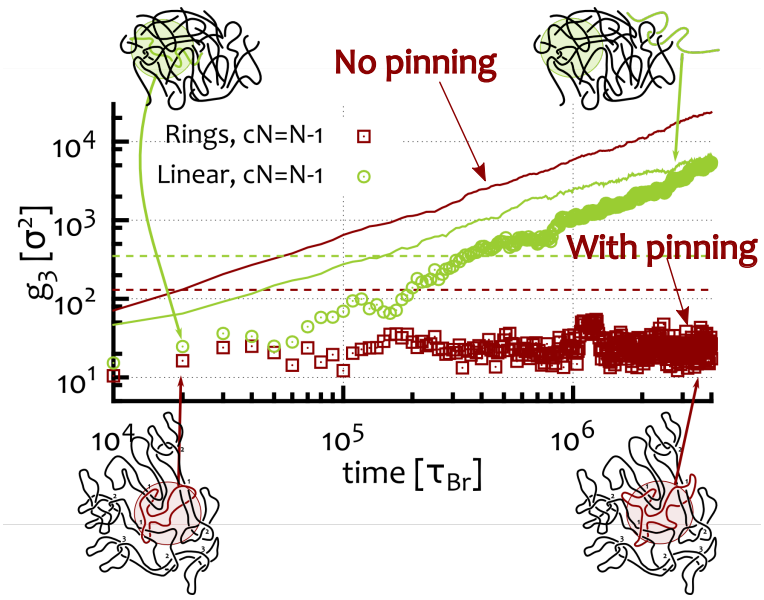

Figure 1.5: Plots of the mean square displacements of the center of mass for linear and ring polymers. Open green circles: A mobile linear chain in a background of pinned (frozen) linear chains. Open red squares: A mobile ring polymer in a background of pinned (frozen) ring polymers. Green curve is for a melt of linear polymers while red line for a melt of ring polymers . Insets sketch melts of linear (top row) and ring (bottom row) polymers. This figure is cited from Ref. [67].

exhibit the expanded conformations and large value of the radius of gyration R_g. The pinning MD is often used to investigate the glass-forming liquids, preventing the collective motion of particles to enhance the packing effect. Fig. 1.5 shows the mean squared displacement (MSD) of the center of mass both for ring and linear polymers with or without pinning. The diffusion in ring polymers are frozen above the critical pinning fraction, although linear polymers can diffuse even if all polymers are pinned except for one. Furthermore, the critical chain length N required to achieve a glassy state without pinning has been estimated to be $N \sim 3500$. This indicates that the TCs between ring and linear polymers are significantly different, and the exist of the glassy state is expected in ring polymers at the long chain length N at the temperature well above the glass transition temperature T_g. Below the glass transition temperature T_g, the particles are too tightly packed to diffuse. In contrast, in this glass-like state obtained by pinning MD, the particles are not packed but the centers of mass of polymer chains are constrained by the TCs, or threading. Thus, the glassy state is called the "topological glass (TG)". Although lots of studies on ring polymers have been reported, the TG has not yet been observed either experimentally and computationally in equilibrium systems.

1.6 Organization of this dissertation

In this study, we performed (MD) simulations of polymer glasses, melts and solutions both for linear and ring polymers by utilizing the Kremer–Grest model. The aim of this study is to elucidate the effects of chain stiffness on the glassiness of polymers and the origin of the TG through capturing the glassy dynamics. Chpater 2 reveals the relationship between the vibrational density of states (vDOS) and the chain stiffness in linear polymer. In Chapter 3, we examine TCs differences with and without chain ends in polymer melts by analyzing the Rouse modes and non-Gaussian parameter (NGP). We found that the both Rouse modes and NGP can characterize the TCs and flexble ring chains show the Gaussian distribution of the displacement. Chapter 4 focuses on the effect of chain stiffness on the rearrengement of center of mass (COM) in ring polymer melts and solutions. By analyzing the bond-breakage dynamics, which quantifies the rearrangement of COM as the virtual bond between two COMs is broken, it is revealed that the chain stiffness causes the glassy dynamics. Furthermore, the density dependence of the mean squared radius of gyration was also investigated. The glassy heterogeneous dynamics and the radius of gyration are found to be correlated. In Chapter 5, we utilize the persistent homology (PH) to quantify the threading structures in ring polymers. The PH identified the asymmetry between active and passive threading. It is possibly to clarify the asymmetry is contributed to dynamic heterogeneity in ring polymers. Thus, developments of threading networks are expected to result in the formation of TG.

Chapter 2

Understanding the scaling of boson peak through insensitivity of elastic heterogeneity to bending rigidity in polymer glasses

2.1 Introduction

Amorphous materials exhibit anomalous mechanical and vibrational properties that have been studied for many years by experimental, numerically, and theoretical methods. The vibrational and acoustical properties of such materials have been investigated in many experiments using neutron, light, and X-ray scattering, *e.g.*, Refs. [70–78]. Using these methods, anomalies in vibrational and acoustic excitations have been detected, including excess vibrational states, the so-called boson peak (BP), and strong damping of sound wave propagation.

To explain these anomalous properties, the heterogeneous elasticity theory was proposed and developed by Schirmacher and co-workers [79–82] (see also Refs. [83, 84] for the theory in the context of the jamming transition and Refs. [85–87] for very recent developments). It is now well-established that amorphous materials exhibit spatial heterogeneity in their local elastic modulus distributions, as supported by numerical simulations [88–90] and experiments [91, 92]. In the theory, elastic moduli heterogeneities are critical in describing anomalies in the vibrational, acoustic, and thermal properties. The theory notably predicts that the BP and the attenuation rate of sound are more significant when moduli distributions are more heterogeneous. This prediction has been

tested and justified by numerical simulations [93–99].

Anomalous behaviours in polymer glasses have also been reported through both experiments [100–106] and numerical simulations [107–112]. In polymer glasses, the bending rigidity of the constituent polymer chains is an important parameter. In our recent work [113], we studied the effects of the bending rigidity on the global elastic moduli (shear modulus G and bulk modulus K) and the vibrational density of states (vDOS) $g(\omega)$ using coarse-grained molecular dynamics (MD) simulations. We demonstrated that the variation of the BP simply follows that of global shear modulus G through the Debye frequency ω_{D}. If this simple scaling behaviour is considered in terms of the heterogeneous elasticity theory, we obtain an important implication that the spatial heterogeneity in local modulus distributions is insensitive to changes in the bending rigidity.

In this study, we examine this correlation by directly measuring the degree of elastic heterogeneity with changes in the bending rigidity. We also study transverse acoustic excitations in the polymer glasses by calculating the dynamic structure factor and examine the connection among the sound velocity, attenuation rate, and the simple scaling behaviour of the BP. Thus, we comprehensively discuss that the effects of bending rigidity in polymer glasses on vibrational and acoustic excitations from the perspective of elastic heterogeneities.

The remainder of this paper is organized as follows. Section 2.2 describes the MD simulation details used to characterise the elastic heterogeneity and the acoustic excitation. In Section 2.3, the numerical results and discussions are presented. Finally, our conclusions are drawn in Section 2.4.

2.2 Simulation method

2.2.1 Simulation model

We performed MD simulations using the Kremer–Grest model [114], which is a coarse-grained bead-spring model of the polymer chain. Each polymer chain comprises L monomer beads of mass m and diameter σ. We studied the case of 200 chains of $L = 50$, such that the system contained $N = 200 \times 50 = 10000$ monomer beads in total, in a three-dimensional cubic box of volume V under

periodic boundary conditions.

In the Kremer–Grest model, three types of inter-particle potentials are utilised. First, the Lennard-Jones (LJ) potential

$$U_{\mathrm{LJ}}(r) = 4\varepsilon_{\mathrm{LJ}}\left[\left(\frac{\sigma}{r}\right)^{12} - \left(\frac{\sigma}{r}\right)^{6}\right], \tag{2.1}$$

acts between all pairs of monomer beads, where r and $\varepsilon_{\mathrm{LJ}}$ denote the distance between two monomers and the energy scale of the LJ potential, respectively. The LJ potential is truncated at the cut-off distance of $r_c = 2.5\sigma$, where the potential and the force (the first derivative of the potential) are shifted to zero continuously [115].

Second, sequential monomer beads along the polymer chain are connected by a finitely extensible nonlinear elastic (FENE) potential:

$$U_{\mathrm{FENE}}(r) = \begin{cases} -\dfrac{\varepsilon_{\mathrm{FENE}}}{2} R_0^2 \ln\left[1 - \left(\dfrac{r}{R_0}\right)^2\right] & (r \le R_0), \\ \infty & (r > R_0), \end{cases} \tag{2.2}$$

where $\varepsilon_{\mathrm{FENE}}$ is the energy scale of the FENE potential, and R_0 is the maximum length of the FENE bond. Following Ref. [111], we employ the values of $\varepsilon_{\mathrm{FENE}} = 30\varepsilon_{\mathrm{LJ}}$ and $R_0 = 1.5\sigma$.

Finally, the bending angle θ formed by three consecutive monomer beads along the polymer chain is controlled by

$$U_{\mathrm{bend}}(\theta) = \varepsilon_{\mathrm{bend}}\left[1 - \cos(\theta - \theta_0)\right], \tag{2.3}$$

where $\varepsilon_{\mathrm{bend}}$ is the associated bending energy. We set the stabilised angle as $\theta_0 = 109.5^\circ$ [111]. In the present work, we utilise a wide range of $\varepsilon_{\mathrm{bend}}$ values: $\varepsilon_{\mathrm{bend}}/\varepsilon_{\mathrm{LJ}} = 10^{-1}$, 1, 3, 10, 30, 10^2, 3×10^2, 10^3, and 3×10^3.

We performed the MD simulations using the Large-scale Atomic/Molecular Massively Parallel Simulator (LAMMPS) [116]. Hereafter, the length, energy, and time are measured in units of σ, $\varepsilon_{\mathrm{LJ}}$, and $\sigma(m/\varepsilon_{\mathrm{LJ}})^{1/2}$, respectively. The temperature is presented in units of $\varepsilon_{\mathrm{LJ}}/k_{\mathrm{B}}$, where k_{B} is the Boltzmann constant. We first equilibrated the polymer melt system at a temperature $T = 1.0$ and

polymer bead number density $\hat{\rho} = N/V = 0.85$. We then cooled the system down towards $T = 0.05$ with a constant cooling rate of $dT/dt = 10^{-4}$, under a fixed pressure of $p = 0$. Finally, the inherent structure at $T = 0$ is generated using the steepest descent method. In our recent work [113], we reported the dependence of the glass transition temperature T_g and the number density $\hat{\rho}$ at zero temperature on $\varepsilon_{\text{bend}}$.

2.2.2 Vibrational density of state and boson peak

The vDOS analysis was performed for the configuration at $T = 0$, which corresponds to the inherent structure. By diagonalizing the Hessian matrix, we obtained the eigenvalues λ^k ($k = 1, 2, \cdots, 3N$), which provide the eigenfrequencies as $\omega^k = \sqrt{\lambda^k}$. The vDOS is defined as

$$g(\omega) = \frac{1}{3N-3} \sum_{k=1}^{3N-3} \delta(\omega - \omega_k), \tag{2.4}$$

where three zero-frequency modes are omitted. The expression of the Hessian matrix of the polymeric system was given in Ref. [113]. The Debye law predicts the vDOS as $g_{\text{D}}(\omega) = \omega^2 A_{\text{D}}$, where $A_{\text{D}} = 3/{\omega_{\text{D}}}^3$ is the Debye level using the Debye frequency $\omega_{\text{D}} = 18\pi^2\rho/(2{c_{\text{T}}}^{-3} + {c_{\text{L}}}^{-3})^{1/3}$. Here, the transverse and longitudinal sound velocities, c_{T} and c_{L}, are given by the bulk modulus K, shear modulus G, and the mass density $\rho = m\hat{\rho}$ as $c_{\text{T}} = \sqrt{G/\rho}$ and $c_{\text{L}} = \sqrt{(K + 4G/3)/\rho}$, respectively. The reduced vDOS $g(\omega)/\omega^2$ thus characterises the excess vibrational modes exceeding the Debye prediction, *i.e.*, the BP.

2.2.3 Global and local shear modulus

The global shear modulus G and bulk modulus K were evaluated from the stress-tensor response to the shear and volume deformations in the "quasi-static" way, respectively, applied to the inherent structure. For perfect crystalline solids, the mechanical equilibrium is maintained during affine deformation. However, the force balance is generally broken down for amorphous solids under applied affine deformations. Thus, further energy minimization causes additional non-affine defor-

mation (relaxation) towards mechanical equilibrium. In other words, G and K are decomposed into $G = G_{\rm A} - G_{\rm NA}$ and $K = K_{\rm A} - K_{\rm NA}$. Here, $M_{\rm A}$ and $M_{\rm NA}$ denote the affine and non-affine components of elastic moduli, with $M = G$ and K, respectively. Our recent work [113] also reported the $\varepsilon_{\rm bend}$ dependence of G and K. In particular, we demonstrated that the bulk modulus K is much larger than the shear modulus G, and thus the shear modulus has important effects on the low-frequency vibrational properties of the polymeric system.

In this study, we further study the *local* shear modulus. Specifically, we measure the spatial distribution of the local shear modulus $G_{\rm m}$, by using the numerical procedure of "affine strain approach", given in Ref. [90]. Note that the analysis completely neglects anharmonic effects and provide zero-temperature limit values of elastic heterogeneities. Briefly, we divided the system into 7×7×7 cubic cells and monitored the local shear stress as a function of the applied shear strain in each local cell. The linear dimension of the cell is approximately $W \approx 3\sigma$. Here, the local strain of the small cell is assumed to be given by the global strain applied to the system. The local shear modulus G_m of cell m was measured as the slope of the local shear stress versus the shear strain. The expression of the local modulus was also given in Ref. [90]. Finally, we collected the G_m values for all the cells to calculate the probability distribution of the local shear modulus $P(G_{\rm m})$. Remark that the average and standard deviation of the local shear modulus distribution is insensitive to the cell size W [90].

As in the LJ glass [88, 90], we found that $P(G_m)$ is well fitted to the Gaussian

$$P(G_{\rm m}) = \frac{1}{\sqrt{2\pi}\delta G_{\rm m}} \exp\left\{\left[-\frac{(G_{\rm m} - G)^2}{2\delta {G_{\rm m}}^2}\right]\right\}, \tag{2.5}$$

where the relative standard deviation $\delta G_{\rm m}/G$ provides a measure of the spatial heterogeneity in the local shear modulus distribution.

2.2.4 Transverse acoustic excitation

The transverse acoustic excitation can be characterised by the (transverse) dynamic structure factor as a function of the wave vector $\boldsymbol{q}$ and frequency ω [93, 96, 117, 118]:

$$S_{\mathrm{T}}(q,\omega) = \left(\frac{q}{\omega}\right)^2 \frac{1}{2\pi} \int \frac{1}{N} \langle \boldsymbol{j}_{\mathrm{T}}(\boldsymbol{q},t) \cdot \boldsymbol{j}_{\mathrm{T}}^{*}(\boldsymbol{q},0) \rangle \exp(i\omega t) dt, \tag{2.6}$$

where $q = |\boldsymbol{q}|$, '$*$' indicates complex conjugation, and $\langle \cdots \rangle$ denotes the ensemble average over the initial time and angular components of $\boldsymbol{q}$. Here, the transverse current is expressed by:

$$\boldsymbol{j}_{\mathrm{T}}(\boldsymbol{q},t) = \sum_{i=1}^{N} [\boldsymbol{v}_i(t) - (\boldsymbol{v}_i(t) \cdot \hat{\boldsymbol{q}})\hat{\boldsymbol{q}}] \exp\left[i\boldsymbol{q} \cdot \boldsymbol{r}_i(t)\right], \tag{2.7}$$

where $\hat{\boldsymbol{q}} = \boldsymbol{q}/q$, and $\boldsymbol{r}_i$ and $\boldsymbol{v}_i (= d\boldsymbol{r}_i/dt)$ represent the position and velocity, respectively, of the monomer bead i. In general, the dynamic structure factor $S(q,\omega)$ exhibits two kinds of peaks: the Rayleigh (elastic) peak and the Brillouin (inelastic) peak. The Rayleigh peak is located at $\omega \to 0$ and is related to the thermal diffusion, while the Brillouin peak is related to the (transverse) sound-wave propagation.

The Brillouin peak in $S_{\mathrm{T}}(q,\omega)$ can be fitted by the damped harmonic oscillator function [93, 96, 117, 118],

$$S_{\mathrm{T}}(q,\omega) \propto \frac{\Gamma_{\mathrm{T}}(q)\Omega_{\mathrm{T}}^2(q)}{[\omega^2 - \Omega_{\mathrm{T}}^2(q)]^2 + \omega^2\Gamma_{\mathrm{T}}^2(q)}, \tag{2.8}$$

which provides information about the propagation frequency $\Omega_{\mathrm{T}}(q)$ and the attenuation rate $\Gamma_{\mathrm{T}}(q)$ as functions of the wave number q. The sound velocity is then given by $c_{\mathrm{T}}(q) = \Omega_{\mathrm{T}}(q)/q$. Note that the sound velocity $c_{\mathrm{T}}(q)$ converges to the macroscopic value $c_{\mathrm{T}} = \sqrt{G/\rho}$ in the long-wavelength limit of $q \to 0$. We numerically calculated the dynamic structure factor $S_{\mathrm{T}}(q,\omega)$ [Eq. (2.6)] of the inherent structure for each bending energy $\varepsilon_{\mathrm{bend}}$ from $\varepsilon_{\mathrm{bend}} = 10^{-1}$ to 3×10^3. Note that the thermal fluctuations are imposed at very low temperature $T = 0.05$, which is small enough that the derived values are consistent with the zero-temperature limit values. The values of $\Omega_{\mathrm{T}}(q)$ and $\Gamma_{\mathrm{T}}(q)$ were then extracted using Eq. (2.8).

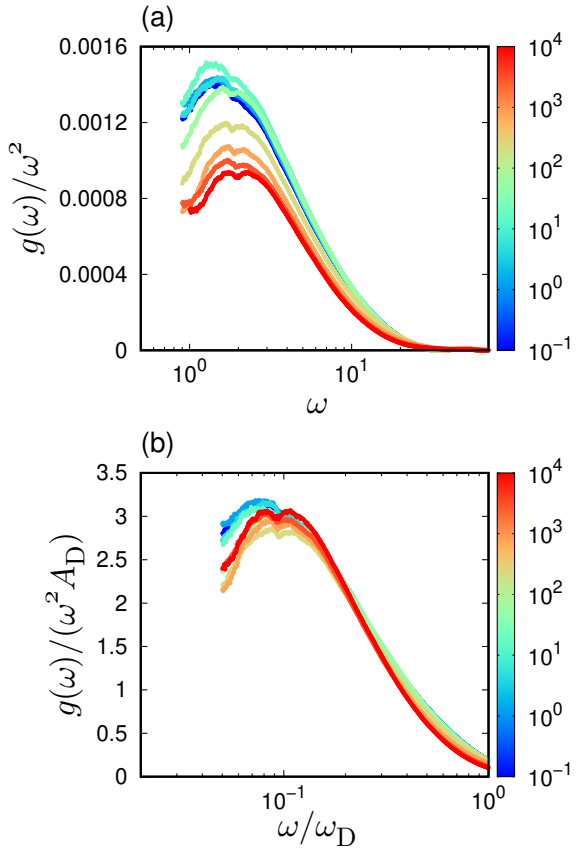

Figure 2.1: (a) The reduced vDOS $g(\omega)/\omega^2$ with changing the strength of bending rigidity $\varepsilon_{\text{bend}}$. (b) The reduced vDOS $g(\omega)/(\omega^2 A_{\text{D}})$ scaled by the Debye level A_{D} as a function of the frequency ω/ω_{D} scaled by the Debye frequency ω_{D}. The color of line indicates the value of bending rigidity $\varepsilon_{\text{bend}}$ according to the color bar.

2.3 Results and Discussion

2.3.1 Scaling of boson peak by the Debye frequency and Debye level

Figure 2.1(a) plots the reduced vDOS $g(\omega)/\omega^2$, showing the BP beyond the Debey level A_{D} for each $\varepsilon_{\text{bend}}$. The BP frequency ω_{BP} is located at $\omega_{\text{BP}} \approx 2$, but it slightly shifts to the higher frequency with increasing the bending rigidity. In addition, the peak height of $g(\omega)/\omega^2$ gradually decreases when $\varepsilon_{\text{bend}}$ is increased. Figure 2.1(b) shows the reduced vDOS $g(\omega)/(\omega^2 A_{\text{D}})$ scaled by the Debye level A_{D} as a function of the frequency ω/ω_{D} scaled by the Debye frequency ω_{D}. This demonstrates the scaling of the BP by the Debye frequency ω_{D} and Debye level A_{D} for various bendig rigidities of

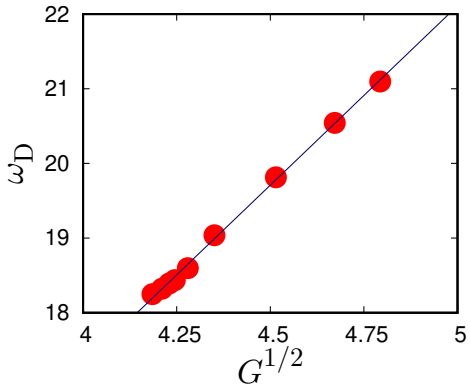

Figure 2.2: Debye frequency ω_D versus square root of global shear modulus G. The straight line is a viewing guide for $\omega_D \propto G^{1/2}$. From left to right, the bending energy changes from $\varepsilon_{bend} = 10^{-1}$ to 3×10^3.

the polymer chain. Note that the scaling property of the BP is also shown for shorter polymer chain with the length $L = 3$ in our previous paper [113].

2.3.2 Debye frequency and global shear modulus

We next examine the relationship between the Debye frequency ω_D and the shear modulus G, which is plotted in Fig. 2.2. As demonstrated in Ref. [113], the bulk modulus K is approximately three to four times larger than the shear modulus G. Thus the term ${c_L}^{-3}$ becomes negligible, and the Debye frequency ω_D can be approximated as

$$\omega_D = \left[\frac{18\pi^2\rho}{2{c_T}^{-3} + {c_L}^{-3}} \right]^{1/3} \simeq (9\pi^2\rho)^{1/3} c_T \propto \sqrt{G}, \tag{2.9}$$

which is mainly governed by the shear modulus G. Figure 2.2 directly demonstrates the relationship of $\omega_D \propto \sqrt{G}$ with changes in ε_{bend}. The density ρ is also changed by changing ε_{bend}, but the effect of density on ω_D is close to negligible [113].

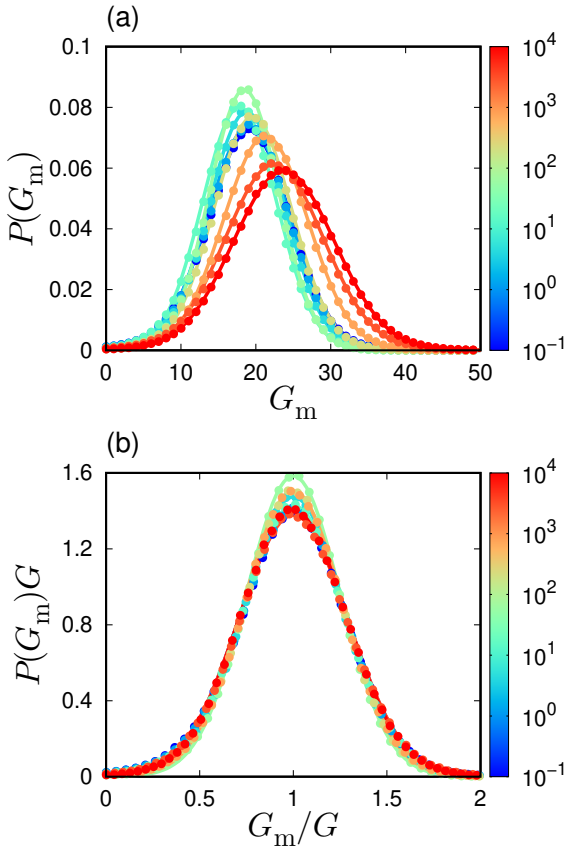

Figure 2.3: (a) Probability distribution of local shear modulus $P(G_m)$. The color of the line indicates the value of the bending energy ε_{bend} according to the color bar. (b) Scaled distribution $P(G_m)G$ as a function of the scaled local shear modulus G_m/G. The straight lines represent the Gaussian distribution functions fitted to each distribution.

2.3.3 Local shear modulus distribution

As demonstrated in Fig. 2.1, the reduced vDOS $g(\omega)/\omega^2$ in the BP frequency ω_{BP} regime was well scaled by using the Debye frequency ω_D and Debye level $A_D = 3/{\omega_D}^3$ This suggests that the frequency and intensity of BP are controlled only by the global sear modulus G. In particular, we obtain the relationship of $\omega_{BP} \propto \omega_D \propto \sqrt{G}$. According to the heterogeneous elasticity theory [79–82], this observation implies that the degree of the shear modulus heterogeneity $\delta G_m/G$ is invariant with changes in the bending energy ε_{bend}: this implication is confirmed below.

We plot the probability distribution of the local shear modulus G_m in Fig. 2.3(a); this plot follows the Gaussian form of Eq. (3.18). Figure 2.3(b) then plots the scaled distribution $P(G_m)G$

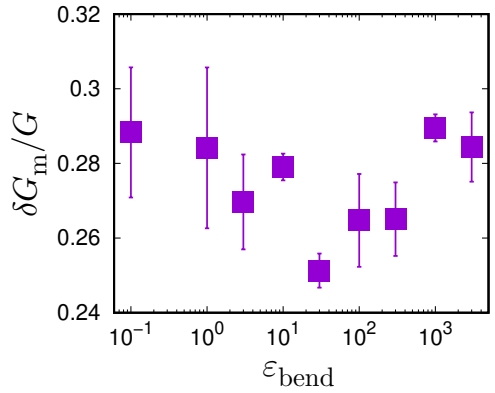

Figure 2.4: Shear modulus heterogeneity $\delta G_{\rm m}/G$ versus bending energy $\varepsilon_{\rm bend}$.

as a function of the scaled local shear modulus $G_{\rm m}/G$, demonstrating the data of $P(G_{\rm m})G$ versus $G_{\rm m}/G$ nicely collapse for different values of $\varepsilon_{\rm bend}$. Because we can transform $P(G_{\rm m})$ (Gaussian form) to

$$P(G_{\rm m})G = \frac{1}{\sqrt{2\pi}\left(\frac{\delta G_{\rm m}}{G}\right)} \exp\left\{\left[-\frac{\left(\frac{G_{\rm m}}{G}-1\right)^2}{2\left(\frac{\delta G_{\rm m}}{G}\right)^2}\right]\right\}, \tag{2.10}$$

this collapse indicates that the scaled standard deviation $\delta G_{\rm m}/G$ remains unchanged for different $\varepsilon_{\rm bend}$ values. This is verified by direct demonstration in Fig. 2.3(b), where $\delta G_{\rm m}/G$ is plotted explicitly as a function of $\varepsilon_{\rm bend}$. Therefore, we can conclude that the bending rigidity of the polymer chain does not alter the degree of the shear modulus heterogeneity. This conclusion justifies the theoretical prediction [79–82] that vibrational excitations including the BP are controlled only by the global elastic modulus under the condition of constant heterogeneities in the moduli distributions.

2.3.4 Transverse acoustic excitation and its link with boson peak

We finally study the transverse acoustic excitation in the frequency regime including the BP. The generalised Debye model [93, 119] yields the reduced vDOS $g(\omega)/\omega^2$ in terms of the propagation frequency $\Omega_{\rm T}(q)$ and the attenuation rate $\Gamma_{\rm T}(q)$, as follows:

$$\frac{g(\omega)}{\omega^2} = \frac{3}{\omega_{\rm D}^3} + \frac{4}{\pi q_{\rm D}^2 c_{\rm T}^2(q)}\left[\frac{\Gamma_{\rm T}(q)}{\omega^2+\Gamma_{\rm T}^2(q)}\right], \tag{2.11}$$

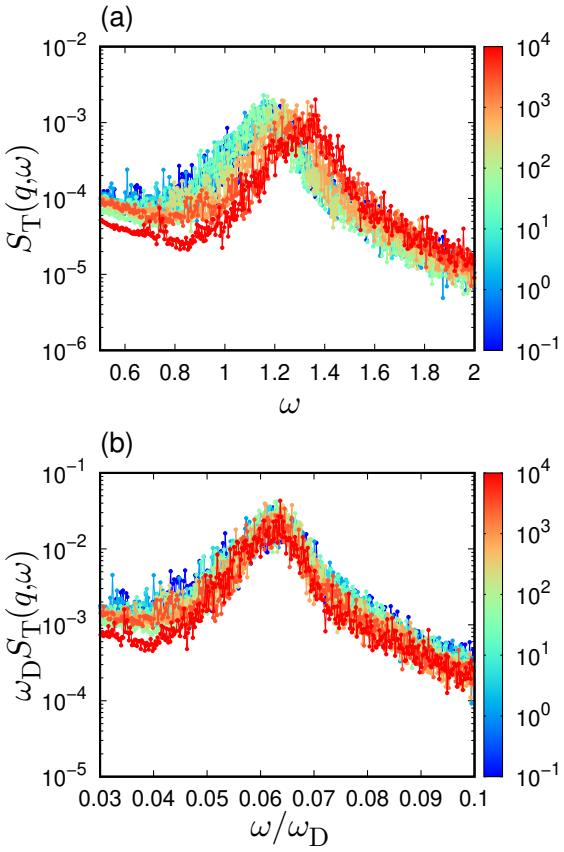

Figure 2.5: (a) Transverse dynamic structure factor $S_T(q,\omega)$ as a function of ω, at the lowest wave number q_{min}. (b) Scaled plot of $S_T(q,\omega)\omega_D$ versus ω/ω_D. The color of the line indicates the value of the bending energy ε_{bend} according to the color bar.

with Debye wavenumber $q_D = (6\pi^2\hat{\rho})^{1/3}$. This form can be scaled by ω_D and $A_D = 3/\omega_D^3$ as:

$$\frac{g(\omega)}{\omega^2 A_D} = 1 + \frac{4}{3\pi q_D^2 \left(\frac{c_T(q)}{\omega_D}\right)^2}\left[\frac{\left(\frac{\Gamma_T(q)}{\omega_D}\right)}{\left(\frac{\omega}{\omega_D}\right)^2 + \left(\frac{\Gamma_T(q)}{\omega_D}\right)^2}\right]. \tag{2.12}$$

Thus, the collapse of the reduced vDOSs $g(\omega)/(\omega^2 A_D)$ for different values of ε_{bend} indicates that c_T/ω_D and Γ_T/ω_D are both independent of the bending energy ε_{bend}.

In addition, Eq. (2.8), which is the damped harmonic oscillator function for the dynamic structure factor $S_T(q,\omega)$, can be scaled by the Debye frequency ω_D:

$$S_T(q,\omega)\omega_D \propto \frac{\left(\frac{\Gamma_T(q)}{\omega_D}\right)\left(\frac{c_T(q)}{\omega_D}\right)^2 q^2}{\left[\left(\frac{\omega}{\omega_D}\right)^2 - \left(\frac{c_T(q)}{\omega_D}\right)^2 q^2\right]^2 + \left(\frac{\omega}{\omega_D}\right)^2\left(\frac{\Gamma_T(q)}{\omega_D}\right)^2}, \tag{2.13}$$

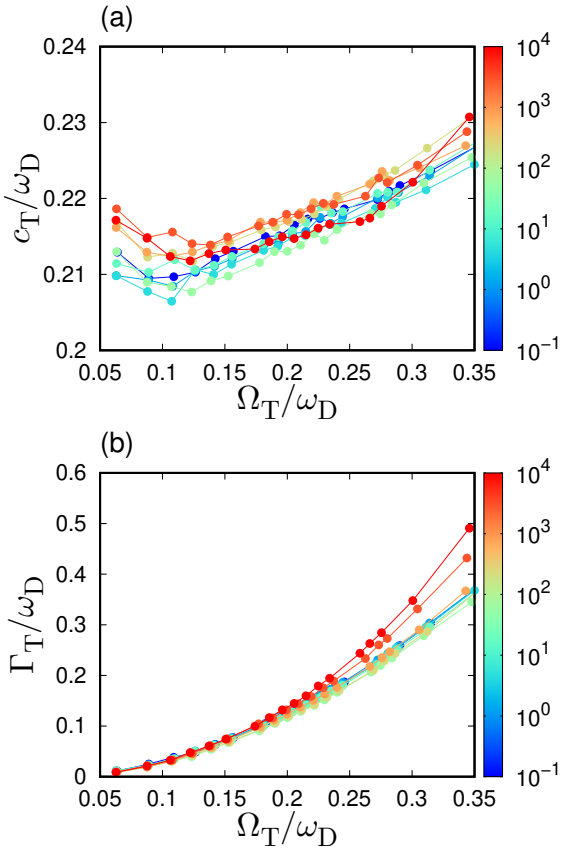

Figure 2.6: (a) Transverse sound velocity scaled by the Debye frequency, c_T/ω_D, versus scaled frequency Ω_T/ω_D. (b) Transverse sound damping scaled by the Debye frequency, Γ_T/ω_D, versus Ω_T/ω_D. The color of the line indicates the value of bending energy ε_{bend} according to the color bar.

which indicates that $S_T(q,\omega)\omega_D$ is simply scaled by ω/ω_D, when c_T/ω_D and Γ_T/ω_D are independent of ε_{bend}. Below we show that these properties of transverse acoustic excitations are true.

Figure 2.5(a) shows the $S_T(q,\omega)$ for different values of ε_{bend}. The wave number q is set to its lowest value $q_{min} = 2\pi(\hat{\rho}/N)^{1/3}$, which ranges from $q_{min} = 0.283$ (for $\varepsilon_{bend} = 0.1$) to 0.295 (for $\varepsilon_{bend} = 3\times10^3$). The frequency of the Brillouin peak shifts to higher values with increasing ε_{bend}. We then plot $S_T(q,\omega)\omega_D$ versus ω/ω_D in Fig. 2.5(b). It is evident that our calculations of $S_T(q,\omega)$ are in accordance with the predicted scaling description of Eq. (2.13).

We also show the sound velocity c_T and attenuation rate Γ_T as functions of the frequency Ω_T in Fig. 2.6. As expected from the scaling property of $g(\omega)$, the data of c_T and Γ_T collapse for different values of ε_{bend}, although small deviations are detected. These collapses are also consistent with the prediction from Eq. (2.12) and are explained in terms of the shear modulus heterogeneity.

The collapses break down in the high frequency regime above the BP frequency, $\Omega_T/\omega_D \gtrsim 0.2 > \omega_{BP}/\omega_D \approx 0.1$. Because the generalized Debye model does not hold above the BP frequency [93, 119], this deviation is not unexpected.

2.4 Conclusion

In conclusion, we have numerically studied elastic heterogeneities and acoustic excitations in polymer glasses, with particular attention to the effects of the bending rigidity of the constituent polymer chains. Our main finding is that the degree of heterogeneity in the local shear modulus distribution is insensitive to changes in the bending rigidity. According to the heterogeneous elasticity theory, for unchanging elastic heterogeneities, the vibrational and acoustic properties of amorphous materials are controlled only by global elastic moduli. Consistent with this theoretical prediction, we demonstrated that the BP and properties of the transverse acoustic excitations are both simply scaled only by the global shear modulus. The present work therefore clarified remarkably simple material property relationships in polymer glasses. These originate from the invariance of the local elastic heterogeneities over an extremely wide range of bending rigidity values for polymer chains. Our results also provide good demonstrations that verify the heterogeneous elasticity theory [79–82], which is among the central theories used to describe the mechanical and vibrational properties of amorphous materials.

We note that effects of polymerization on vibrational properties can be scaled by global elastic moduli [102, 106]. On the contrary, some experiments demonstrate that the pressure-induced shift of BP cannot be explained by the global elastic moduli [100, 101]. From these observations, we speculate that the polymerization effect is insensitive to the elastic heterogeneities as is the bending rigidity, whereas the heterogeneities would be altered by the densification. Furthermore, recent MD simulations revealed antiplasticizer additives significantly modify the local elastic constant distribution in glass-forming polymer liquids [120]. It could be interesting to study how boson peak properties change with evolution of elastic heterogeneities during the antiplasticization process.

At the end of this paper, we would discuss the relationship between the structural relaxation time and the elastic properties. Remarkably, numerical work [121] has proposed and demonstrated a scaling relationship between the structural relaxation time τ_α and the Debye–Waller factor $\langle u^2 \rangle$ for many types of glass-forming systems, including polymer glasses, as $\tau_\alpha \propto \exp\left(a\langle u^2\rangle^{-1} + b\langle u^2\rangle^{-2}\right)$ (where a and b are constants). Because the Debye–Waller factor in the harmonic approximation limit is estimated as $\langle u^2 \rangle = 3T \int_0^\infty g(\omega)/\omega^2 d\omega \propto T{\omega_{\rm BP}}^{-2} \propto TG^{-1}$ (where $\omega_{\rm BP} \propto \sqrt{G}$ is applied) [122], we obtain

$$\tau_\alpha \propto \exp\left(\alpha \frac{{\omega_{\rm BP}}^2}{T} + \beta \frac{{\omega_{\rm BP}}^4}{T^2}\right) \propto \exp\left(\alpha' \frac{G}{T} + \beta' \frac{G^2}{T^2}\right), \tag{2.14}$$

where α, β, α', and β' are constants. This is the idea of the shoving model [123, 124], which characterises the activation energy in terms of the global shear modulus G. Interestingly, Eq. (2.14) has been well demonstrated for polymer glasses by MD simulations, where the plateau modulus $G_{\rm p}$ of the stress correlation function was effectively utilized as the shear modulus [125]. Our results suggest an important condition under which Eq. (2.14) holds. When the spatial heterogeneity in the local shear modulus distribution is unchanged, the excess vibrational excitations, *i.e.*, the BP, are controlled only by the global shear modulus, indicating that the structural relaxation time is also controlled solely by the global shear modulus.

Chapter 3

Effects of chain length on Rouse modes and non-Gaussianity in linear and ring polymer melts

3.1 Introduction

The dynamics of polymer melts are governed by topological constraints, because of which the viscosity and relaxation time increase drastically with increasing degree of polymerization. Linear chain ends play a significant role in determining the slip motion of a single polymer chain, which is characterized by the well-established reptation model [2]. Recently, another type of topological constraints in polymer has been proposed, namely, ring polymer melts without chain ends [3–7].

Various molecular dynamics (MD) simulations have been performed to elucidate the topological constraint effects in ring polymer melts [9–11, 18, 46, 65, 126, 127]. In this regard, the chain length N dependence of dynamical properties is the central topic. Tsolou *et al.* reported MD simulation results of a united-atom model for ring polyethylene melts with N ranging from 24 to 400 [9]. They demonstrated that the Rouse model is approximately appropriate for describing the dynamics, in contrast to the cases of linear polymer analogues. Halverson *et al.* used a coarse-grained bead-spring model for ring polymers with N ranging from 100 to 1600 [10, 11]. The diffusion coefficient D obeys a scaling $D \sim N^{-2.4}$ for large N–interestingly, this is similar to that observed in linear polymer melts. In contrast, the zero-shear viscosity exhibits a chain length dependence $\eta \sim N^{1.4}$, which is weaker than that predicted by the reptation model.

The dynamics of ring polymer melts have been examined using the dynamic structure fac-

tor measured by neutron scattering experiments [15, 22, 128–130]. Brás *et al.* reported the non-Gaussian parameter (NGP) of pure poly(ethylene oxide) (PEO) rings [15]. The NGP characterizes the degree of the deviation of the distribution function of the monomer displacement from the Gaussian distribution, which is important when discussing the relationship between MD simulations and scattering experiments [131]. Notably, the NGP has frequently been analyzed to characterize heterogeneous dynamics, which is attributed to cage effects in glass-forming liquids [132–134]. However, the chain length dependence of NGP in ring polymers remains scarcely analyzed. Furthermore, this analysis can be also important when considering the recent microscopic theory predicting $D \sim N^{-2}$ in ring polymer melts, which was formulated in analogy with the cage effects of soft colloid suspensions [20].

In this study, we performed MD simulations using the Kremer–Grest bead-spring model with different chain lengths ($N = 5 - 400$) for both linear and ring polymer melts. First, we analyzed the Rouse modes and determined the chain length dependence of the relaxation time. Then, we calculated the NGP of the monomer bead displacement, and investigated its chain length dependence. The combined results enable us to thoroughly assess the similarities and differences of the chain-end effects on the dynamics between linear and ring polymer melts.

3.2 Model and simulations

We performed MD simulations using the standard Kremer–Grest model for linear and ring polymer melts, where the polymer chain comprises N monomer beads of mass m and diameter σ [114]. We utilized three types of inter-particle potentials, as follows. The Lennard-Jones (LJ) potential

$$U_{\mathrm{LJ}}(r) = 4\varepsilon_{\mathrm{LJ}}\left[\left(\frac{\sigma}{r}\right)^{12} - \left(\frac{\sigma}{r}\right)^{6}\right] + C, \tag{3.1}$$

acts between all pairs of monomer beads, where r and $\varepsilon_{\mathrm{LJ}}$ denote the distance between two monomers and the energy scale of the LJ potential, respectively. The LJ potential is truncated at the cut-off distance of $r_c = 2.5\sigma$, and the constant C guarantees that the potential energy shifts to zero at $r = r_c$

The bonding potential between two neighboring monomer beads is given by a finitely extensible nonlinear elastic (FENE) potential,

$$U_{\mathrm{FENE}}(r) = -\frac{1}{2}KR_0^2 \ln\left[1 - \left(\frac{r}{R_0}\right)^2\right] \tag{3.2}$$

for $r < R_0$, where K and R_0 represent the spring constant and the maximum length of the FENE bond, respectively. We used the values of $K = 30\varepsilon_{\mathrm{LJ}}/\sigma^2$ and $R_0 = 1.5\sigma$. Finally, the bending angle θ formed by three consecutive monomer beads along the polymer chain is controlled by

$$U_{\mathrm{bend}}(\theta) = k_\theta[1 - \cos(\theta - \theta_0)], \tag{3.3}$$

where k_θ denotes the associated bending energy. We set the bending energy and equilibrium angle as $k_\theta = 1.5\varepsilon_{\mathrm{LJ}}$ and $\theta_0 = 180°$, respectively.

Henceforth, the length, energy, and time are measured in units of σ, $\varepsilon_{\mathrm{LJ}}$, and $\sigma(m/\varepsilon_{\mathrm{LJ}})^{1/2}$, respectively. The temperature is presented in units of $\varepsilon_{\mathrm{LJ}}/k_{\mathrm{B}}$, where k_{B} is the Boltzmann constant. The system contains M polymer chains in a three-dimensional cubic box of volume V under periodic boundary conditions. We studied several combinations of the chain length N and the number of chains M for both linear and ring polymer systems, $(N, M) = (5, 2000)$, $(10, 1000)$, $(20, 500)$, $(40, 250)$, $(100, 200)$, $(200, 100)$, and $(400, 50)$. The number density of the monomer beads $\rho = (N \times M)/V$ and the temperature T were fixed as $\rho = 0.85$ and $T = 1.0$, respectively, throughout the simulations. We performed the MD simulations using the Large-scale Atomic/Molecular Massively Parallel Simulator (LAMMPS) [135]. The NVT ensemble with the Nosé–Hoover thermostat was used with a time step Δt of 0.01. We analyzed the chain length dependence of the radius of gyration and the center-of-mass diffusion coefficient and confirmed that our results reproduce the results reported in previous studies (results not shown) [10, 11]. In addition, we confirmed the entanglement length $N_{\mathrm{e}} \approx 28$ in linear polymer melts with $N = 400$ by using the primitive path analysis [136]. The used code is available from `https://github.com/t-murash/USER-PPA` (see also Ref. [137]).

The Rouse model is the standard model for the polymer chain dynamics, where the normal

coordinates $\boldsymbol{X}_p(t)$, so-called Rouse modes, are constructed from the position of the n-th monomer bead $\boldsymbol{r}_n(t)$ at a time t for $n = 1, 2, 3, \cdots, N$. Here, we provide several expressions in the Rouse model, which we employ to analyze our MD results. The Rouse mode analysis for the linear chain is described in Ref. [138]. Furthermore, the formula for the ring polymer chain was described in previous papers [9, 139, 140]. To make this paper self-contained, we summarize the formulation of the Rouse model for the ring polymer chain in A. The expressions of the normal coordinates $\boldsymbol{X}_{p,\mathrm{linear}}(t)$ and $\boldsymbol{X}_{p,\mathrm{ring}}(t)$ for linear and ring polymer chains can respectively be expressed as

$$\boldsymbol{X}_{p,\mathrm{linear}}(t) = \sqrt{\frac{2-\delta_{p,0}}{N}} \sum_{n=1}^{N} \boldsymbol{r}_n(t) \cos\left(\frac{\pi p(n-1/2)}{N}\right), \tag{3.4}$$

$$\boldsymbol{X}_{p,\mathrm{ring}}(t) = \sqrt{\frac{1}{N}} \sum_{n=1}^{N} \boldsymbol{r}_n(t) \left[\cos\left(\frac{2\pi pn}{N}\right) + \sin\left(\frac{2\pi pn}{N}\right)\right], \tag{3.5}$$

where $p\ (= 0, 1, \cdots, N-1)$ is the mode index, and δ denotes the Kronecker delta. The $p = 0$ mode describes the center-of-mass translation of the chain, whereas the $p > 0$ modes characterize the internal dynamics of the subchains composed of N/p beads.

The static correlation of the Rouse mode $\langle \boldsymbol{X}_p(0)^2 \rangle$ can be related to the mean square distance of two beads b^2 through

$$\langle \boldsymbol{X}_{p,\mathrm{linear}}(0)^2 \rangle = \frac{b^2}{4\sin^2\left(\frac{\pi p}{2N}\right)}, \tag{3.6}$$

$$\langle \boldsymbol{X}_{p,\mathrm{ring}}(0)^2 \rangle = \frac{b^2}{4\sin^2\left(\frac{\pi p}{N}\right)}, \tag{3.7}$$

for linear and ring polymers, respectively. Here, $\langle \cdots \rangle$ denotes an ensemble average.

Each normal coordinate exhibits the Brownian motion in the Rouse model, causing the exponential decay of the autocorrelation function, $\langle \boldsymbol{X}_p(t) \cdot \boldsymbol{X}_p(0) \rangle$. The Rouse relaxation times $\tau_{p,\mathrm{linear}}$

and $\tau_{p,\mathrm{ring}}$ for linear and ring polymer chains are respectively given by

$$\tau_{p,\mathrm{linear}} = \frac{\zeta}{4k\sin^2\left(\frac{\pi p}{2N}\right)}, \tag{3.8}$$

$$\tau_{p,\mathrm{ring}} = \frac{\zeta}{4k\sin^2\left(\frac{\pi p}{N}\right)}, \tag{3.9}$$

where ζ is the effective hydrodynamic friction coefficient and k represents the harmonic spring constant between two neighboring monomer beads. As noted in A k is equal to $3k_{\mathrm{B}}T/b^2$. The differences of $\langle \boldsymbol{X}_p(0)^2 \rangle$ and τ_p between linear and ring polymers appear in the phases of the sine functions. The Rouse modes of p and $N-p$ are degenerate in the case of the ring polymer (see A). Correspondingly, $\langle \boldsymbol{X}_p(0)^2 \rangle$ and τ_p as functions of p are symmetric with respect to the reflection at $p = N/2$. On the other hand, for linear chains, $\langle \boldsymbol{X}_p(0)^2 \rangle$ and τ_p decrease monotonically with p in the Rouse model. In the continuum limit of $p/N \ll 1$, both $\tau_{p,\mathrm{linear}}$ and $\tau_{p,\mathrm{ring}}$ exhibit a scaling behavior $(N/p)^2$ within the Rouse model.

The motions of monomer beads are described typically by the mean square displacement (MSD) averaged over all the monomers of a chain, which is defined as

$$g_1(t) = \langle r^2(t) \rangle = \left\langle \frac{1}{N} \sum_{n=1}^{N} |\boldsymbol{r}_n(t) - \boldsymbol{r}_n(0)|^2 \right\rangle. \tag{3.10}$$

The NGP of the monomer bead displacement is defined by

$$\alpha_2^{\mathrm{mon}}(t) = \frac{3\langle r^4(t) \rangle}{5\langle r^2(t) \rangle^2} - 1, \tag{3.11}$$

which measures non-Gaussianity, *i.e.*, the degree of the deviation of the distribution function of the monomer bead displacement from the Gaussian form during the time interval t. In addition, the MSD of the center-of-mass of chains is examined from

$$g_3(t) = \langle R^2(t) \rangle = \left\langle \frac{1}{M} \sum_{m=1}^{M} |\boldsymbol{R}_m(t) - \boldsymbol{R}_m(0)|^2 \right\rangle, \tag{3.12}$$

where $\boldsymbol{R}_m(t)$ is the position of the center-of-mass of the chain m at time t. The corresponding NGP of the center-of-mass displacement is defined by

$$\alpha_2^{\mathrm{com}}(t) = \frac{3\langle R^4(t)\rangle}{5\langle R^2(t)\rangle^2} - 1. \tag{3.13}$$

The NGP of monomer beads was analyzed via MD simulations of linear polymer melts with the chain length of $N = 5 - 160$ [141]. Furthermore, the NGP of supercooled polymer melts was reported with $N = 10$ [142] and $N = 64$ [143, 144].

3.3 Results and discussion

The normalized autocorrelation function of the p-th Rouse mode is given by

$$\phi_p(t) = \frac{\langle \boldsymbol{X}_p(t) \cdot \boldsymbol{X}_p(0)\rangle}{\langle \boldsymbol{X}_p(0)^2\rangle}. \tag{3.14}$$

The results of the slowest mode $\phi_1(t)$ are plotted in Fig. 3.1 by changing the chain length N for linear (a) and ring (b) polymer melts. For each Rouse mode p, $\phi_p(t)$ is fitted using the Kohlrausch–Williams–Watts (KWW) function, $\exp\left[-(t/\tau_p^*)^{\beta_p}\right]$, with the KWW relaxation time τ_p^*. $\beta_p(< 1)$ represents the degree of non-exponentiality of $\phi_p(t)$ [145]. In Fig. 3.1(c) and (d), β_p is plotted as a function of N/p for linear and ring polymers, respectively. As demonstrated in Ref. [146], β_p deviates from unity and shows a minimum at the slowing down length $N_\mathrm{s} \approx 2$. Another minimum of approximate 0.6 is found at around the entanglement length scale $N_\mathrm{e} \approx 28$ [147, 148]. As seen in Fig. 3.1(d), β_p of ring polymers shows a minimum at $N_\mathrm{s} \approx 4$, which is the same length scale of $N_\mathrm{s} \approx 2$ considering the difference in the phase of the Rouse mode between linear and ring polymers. Furthermore, the non-exponentiality is also found at $N \gtrsim 10^2$ and is weaker for the ring polymers with $\beta_p \approx 0.8$ than for the linear polymers.

In Fig. 3.1(e) and (f), the normalized amplitudes $4\sin^2(\pi p/(2N))\langle \boldsymbol{X}_p(0)^2\rangle$ and $4\sin^2(\pi p/N)\langle \boldsymbol{X}_p(0)^2\rangle$ are plotted as a function of N/p for linear and ring polymers, respectively. As the chain length

scale N/p increases, $4\sin^2(\pi p/(2N))\langle \boldsymbol{X}_p(0)^2\rangle$ of linear polymers levels off beyond the entanglement length scale $N_\mathrm{e} \approx 28$ [147, 148], whereas $4\sin^2(\pi p/N)\langle \boldsymbol{X}_p(0)^2\rangle$ of ring polymers gradually decreases with increasing N/p. This behavior is actually consistent with the observation that the structure of the ring polymer chain becomes more compact than that of the linear polymer. In fact, N dependence of the mean square radius of gyration R_g^2 approaches a scaling of $N^{2/3}$ in ring polymers, which is distinct from the Gaussian behavior $R_\mathrm{g}^2 \sim N$ observed in linear polymers [10].

The effective Rouse relaxation time of the p-th mode is calculated by

$$\tau_p = \int_0^\infty \exp\left[-(t/\tau_p^*)^{\beta_p}\right] dt = \frac{\tau_p^*}{\beta_p}\Gamma\left(\frac{1}{\beta_p}\right), \tag{3.15}$$

where $\Gamma(x)$ is the Gamma function. The Rouse relaxation time τ_p is plotted as a function of N/p in Fig. 3.1 for linear (g) and ring (h) polymer melts. In linear polymer melts, τ_p rapidly deviates from the Rouse regime $(N/p)^2$ as the chain length N is increases. In particular, the power-law behavior $\tau_p \sim (N/p)^{3.4}$ was observed, indicating entanglement effects [147, 148]. This crossover from the Rouse to the reptation behavior was reported in Refs. [147, 148]. τ_p of ring polymers also deviates from the Rouse-like power-law behavior with increasing N/p. However, the exponent becomes 2.4, which is smaller than that of linear polymers for the chain lengths investigated in this study.

Further, it is important to compare the segmental relaxation rate $W_\mathrm{eff} = 3k_\mathrm{B}T/\zeta b^2 = k/\zeta$ between linear and ring polymer melts, which is related to the Rouse relaxation time τ_p (see Eqs. (3.8) and (3.9)). Specifically, we evaluated W_eff using the slowest mode ($p = 1$) by

$$W_\mathrm{eff,linear} = 1/[4\tau_{1,\mathrm{linear}}\sin^2(\pi/2N)], \tag{3.16}$$

$$W_\mathrm{eff,ring} = 1/[4\tau_{1,\mathrm{ring}}\sin^2(\pi/N)], \tag{3.17}$$

for linear and ring polymers, respectively, and the results are plotted in Fig. 3.2. For linear polymers, W_eff exhibits a roughly constant independent of N up to the entanglement length $N_\mathrm{e} \approx 28$. A similar value is also observed for ring polymers, indicating the same Rouse dynamics in melts of linear and ring chains. The power-law behavior $W_\mathrm{eff} \sim N^{-1.4}$ is observed for the longer linear

polymer, which is consistent with the scaling of $\tau_p \sim (N/p)^{3.4}$, as demonstrated in Fig. 3.1(e). Note that N and p are both varied in Fig. 3.1(e), and the scaling at $p = 1$ is rephrased as $\tau_1 \sim N^{3.4}$ at large N. In contrast, $W_{\rm eff}$ of ring polymers shows a weak N dependence and the scaling $W_{\rm eff} \sim N^{-0.4}$ is observed for the longer chain length $N \gtrsim 100$. This exponent corresponds to the scaling of $\tau_p \sim (N/p)^{2.4}$, as observed in Fig. 3.1(f).

The NGPs of the segment displacement $\alpha_2^{\rm mon}(t)$ and the center-of-mass displacement $\alpha_2^{\rm com}(t)$ were investigated using Eqs. (3.11) and (3.13), respectively. Figure 3.3 shows $\alpha_2^{\rm mon}(t)$ for linear (a) and ring (b) polymers. For comparison, the time evolusions of MSD $\langle r^2(t)\rangle$ are displayed in inset of Fig. 3.3(a) and (b). It is seen that $\alpha_2^{\rm mon}(t)$ exhibits peaks of 0.1 for both linear and ring polymers. The peak occurs at $t \approx 1$, beyond which each segment begins to escape from the regime of ballistic motion, $\langle r^2(t)\rangle \sim t^2$, at small times. The height and position $\alpha_2^{\rm mon}(t)$ in the ballistic regime are independent of the chain length N, indicating that the effects of polymer chain ends are negligible in this regime, where the effect of the chain connectivity plays the role on the segmental dynamics [142]. For linear polymers, the second peak appears at a larger time regime, where $\langle r^2(t)\rangle$ approaches the diffusive behavior, as demonstrated in Fig. 3.3(c). The second peak develops for longer time scales with increasing chain length N, which was demonstrated in the previous study [141]. The height of the second peak becomes 0.5 for $N = 400$. This non-Gaussianity can be regarded as the chain end effect with higher mobility due to less topological constrains [149]. Note that the mechanism of non-Gaussianity in linear polymer melts is different from that of the cage effects in glass-forming liquids [132–134]. On the contrary, it is unlikely that $\alpha_2^{\rm mon}(t)$ of ring polymers shows clear peaks for chain lengths up to $N = 400$ despite the diffusive behavior being realized in $\langle r^2(t)\rangle$ at larger time scales (see Fig. 3.3(d)). This implies that all the monomer beads show similar dynamics in ring polymers without chain ends. The non-Gaussianity of the center-of-mass displacement is additionally examined in Fig. 3.3 for linear (c) and ring (d) polymers. The behavior of $\alpha_2^{\rm com}(t)$ is analogous to that of $\alpha_2^{\rm mon}(t)$ both for linear and ring polymers. However, the first peak of $\alpha_2^{\rm com}(t)$ at $t \approx 1$ becomes smaller with increasing N for both linear and ring polymers. This indicates that regardless of the chain connectivity, the center-of-mass dynamics

is more Gaussian for longer chains. Furthermore, $\alpha_2^{\mathrm{com}}(t)$ of ring polymers with $N = 400$ shows a peak of 0.1 at $t \approx 10^6$, which shows very small non-Gaussianity as the chain length is increased.

Finally, to characterize the difference in the NGP between linear and ring polymers in more detail, we calculated the self-part of the van-Hove correlation function $G_s(r,t) = \langle \sum_{n=1}^{N} \delta(|\boldsymbol{r}_n(t) - \boldsymbol{r}_n(0)| - r) \rangle$, *i.e.*, the distribution function of the segmental displacement r at time t. The probability distribution of the logarithm displacement is then defined as $P(\log_{10}(r),t) = \ln(10) 4\pi r^3 G_s(r,t)$ [150–152]. It is defined such that the integral $\int_{x_0}^{x_1} P(x,t)dx$ is the fraction of particles whose value of $\log_{10}(r)$ is between x_0 and x_1. When the Gaussian distribution is assumed as

$$G_s(r,t) = \left[\frac{3}{2\pi\langle r^2(t)\rangle}\right]^{3/2} \exp\left[\frac{-3r^2}{2\langle r^2(t)\rangle}\right], \tag{3.18}$$

with the mean square displacement $\langle r^2(t)\rangle$ at time t, $P(\log_{10}(r),t)$ has a peak of $\ln(10)\sqrt{54/\pi}e^{-3/2} \approx 2.13$ irrespective of time t. In Fig. 3.4, $P(\log_{10}(r),t)$ is plotted for linear (a) and ring (b) polymers with the chain length $N = 400$ by changing t from 1 to 10^6. For a comparison, we also showed $P(\log(10)(r),t)$ determined from the Gaussian distribution Eq. (3.18) at each time. As observed in Fig. 3.4(a), the peak height of $P(\log_{10}(r),t)$ for the linear polymer decreases as t increases. This decrease in the peak indicates that the distribution deviates from the Gaussian behavior and becomes broader, which is also observed in glass-forming liquids [152]. Figure 3.4(b) demonstrates that the peak height of $P(\log_{10}(r),t)$ for ring polymers remains at the Gaussian level, providing clear evidence that the segment displacement follows the Gaussian distribution even for longer time scales.

Furthermore, Fig. 3.4(c) and Fig. 3.4(d) show the probability distributions of the center-of-mass displacement $P(\log_{10}(R),t)$ for linear and ring polymers, respectively. The deviation from the Gaussian form $G_s(R,t) = [3/(2\pi\langle R^2(t)\rangle)]^{3/2} \exp\left[-3R^2/(2\langle R^2(t)\rangle)\right]$ is noticeable for linear polymers, particularly for longer times. Analogous to Fig. 3.4(b), $P(\log_{10}(R),t)$ of ring polymers is in accordance with the Gaussian distribution at any time. Note that small deviation from the Gaussian distribution at long times were observed in Fig. 3.3(d) for the chain length $N = 400$, while the peak

value remains the Gaussian level of 2.13. This observation suggests the possibility that the center-of-mass dynamics of a long ring polymer chain in melts can be influenced by the neighboring rings.

3.4 Conclusion

We presented the MD simulation results using the Kremer–Grest model for linear and ring polymer melts with chain lengths up to $N = 400$. We focused on the chain length dependence of the Rouse relaxation time and non-Gaussianity for characterizing both the segmental and center-of-mass mobility with or without chain ends.

For linear polymers, the deviation from the Rouse model behavior becomes remarkable with increasing the chain length N by showing the scaling $\tau_p \sim (N/p)^{3.4}$, which is consistent with previously reported results [11]. The NGP of the monomer bead dynamics shows two peaks: the first peak appears on the time scale where the MSD escapes from the segmental ballistic motion, whereas the second peak corresponds to the realization of the diffusive behavior of the MSD. This indicates that the segment dynamics becomes spatially heterogeneous because of the higher mobility of chain ends in the linear polymer chain. The NGP of the center-of-mass dynamics also exhibits two peaks, but the first peak becomes weaker due to less chain connectivity effects as the chain length is increased.

For ring polymers, the Rouse-like behavior with the scaling $\tau_p \sim (N/p)^{2.4}$ was observed. Although the peak of NGP was observed at short times similar to that of linear polymers, the non-Gaussianity was found to be strongly suppressed even for a longer time regime. The segmental dynamics in ring polymers without chain ends becomes spatially homogeneous and the mechanism of the chain motion is essentially different from the reptation model for linear polymers. The center-of-mass dynamics in ring polymers also shows the Gaussian behavior, while a very small non-Gaussianity is observed with increasing chain length suggesting cooperative motions between neighboring rings.

As mentioned in Introduction, Brás *et al*. reported the NGP of the center-of-mass dynamics in PEO ring polymers from a neutron scattering experiment [15]. The molecular weight 5 kg/mol was chosen to be 2.5 times larger than the entanglement mass, which approximately corresponds to the chain length $N = 100$ in the present MD simulation study. The NGP from the neutron scattering experiment shows a peak of 0.2-0.3 at around 30 ns, which corresponds to the crossover from a sub-diffusion to diffusion regime. It seems that the experimental result is not in agreement with the present MD simulation result of $\alpha_2^{\mathrm{com}} \approx 0.1$ with $N = 400$. The effects of the chain lengths and the chemical species of the segments need to be studied in further depths to resolve the difference.

A plausible key feature for topological constraints in ring polymers is an inter-ring threading event [67, 68, 153–159]. In particular, Michieletto *et al.* have proposed the "random pinning" procedure, wherein some fractions of rings are frozen, to investigate the role of threadings on the dynamics [156]. They demonstrated that random pinning can enhance the glass-like heterogeneous dynamics in ring polymers. Furthermore, it was reported that the distribution of the center-of-mass displacement deviates from the Gaussian distribution even in a zero "random pinning" field. In contrast, the non-Gaussianity is much weaker in this work, where $\alpha_2^{\mathrm{com}}(t)$ becomes 0.1 with the chain length $N = 400$ without the pinning procedure. One possible interpretation could be that the thermodynamic states analyzed here are different: monomer density $\rho = 0.85$ in this study is frequently used for MD simulations of polymer melts [10, 11], whereas densities in Ref. [156] were chosen up to $\rho = 0.4$. Therefore, further investigation is necessary for a strict assessment with regard to the monomer density dependence of the non-Gaussianity with increasing the chain length N, which is a subject of future study.

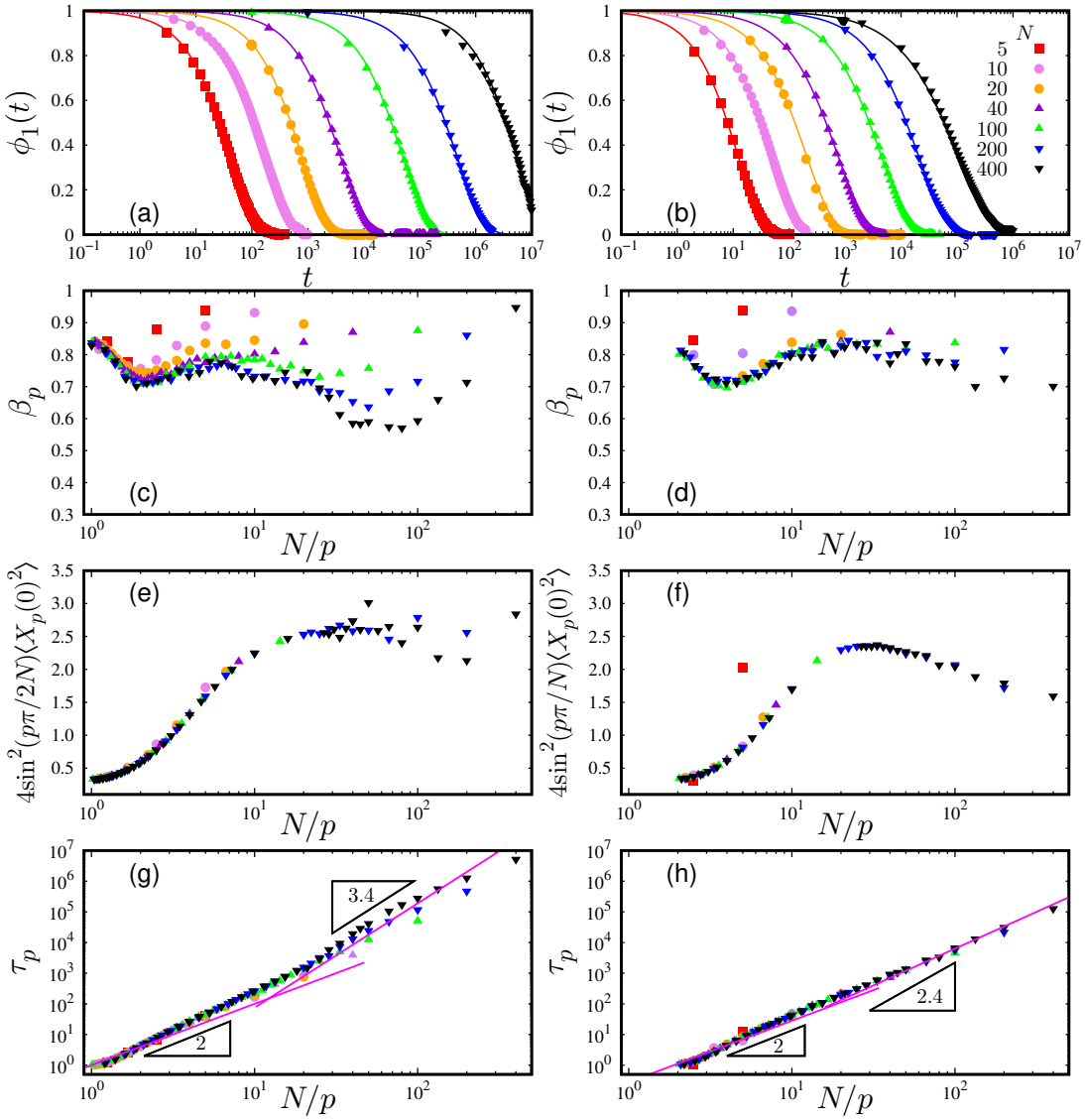

Figure 3.1: Normalized autocorrelation function $\phi_1(t)$ of the Rouse mode $p = 1$ for linear (a) and ring (b) polymers. Symbols and lines represent MD simulation results and the fitting curves using the Kohlrausch–Williams–Watts function, $\exp\left[-(t/\tau_p)^{\beta_p}\right]$. The exponent β_p is plotted as a function of N/p for linear (c) and ring (d) polymers. Normalized amplitude of autocorrelations of the Rouse mode, $4\sin^2(\pi p/(2N))\langle \boldsymbol{X}_p(0)^2\rangle$ (e) and $4\sin^2(\pi p/N)\langle \boldsymbol{X}_p(0)^2\rangle$ (f), are plotted as a function of N/p for linear and ring polymers, respectively. Rouse relaxation time τ_p as a function of N/p for linear (g) and ring (h) polymers. Two scaling behaviors, *i.e.*, the Rouse model behavior $\tau_p \sim (N/p)^2$ and the reptation model behavior $\tau_p \sim (N/p)^{3.4}$, are represented in (g). In (h), $\tau_p \sim (N/p)^2$ is indicated for smaller N/p, whereas the different power-law $\tau_p \sim (N/p)^{2.4}$ is observed for larger N/p. In (d), (f), and (h), the results for $N/p < 2$ are omitted because of the symmetric structure of N/p dependencies on $\langle \boldsymbol{X}_p(0)^2\rangle$ and τ_p (see Eqs. (3.7) and (3.9)). Note that only two points with $p = 1$ and 2 are plotted for $N = 5$ ring polymers, where each ring tends to form a pentagonal structure, causing fluctuations more than other length chains.

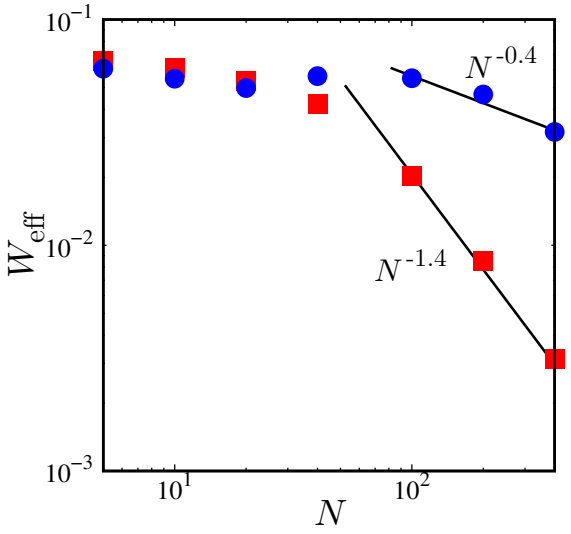

Figure 3.2: Chain length N dependence of the effective segmental relaxation rate $W_{\rm eff}$ for linear (squares) and ring (circles) polymers. Two straight lines are eye guides indicating, $W_{\rm eff} \sim N^{-1.4}$ and $W_{\rm eff} \sim N^{-0.4}$.

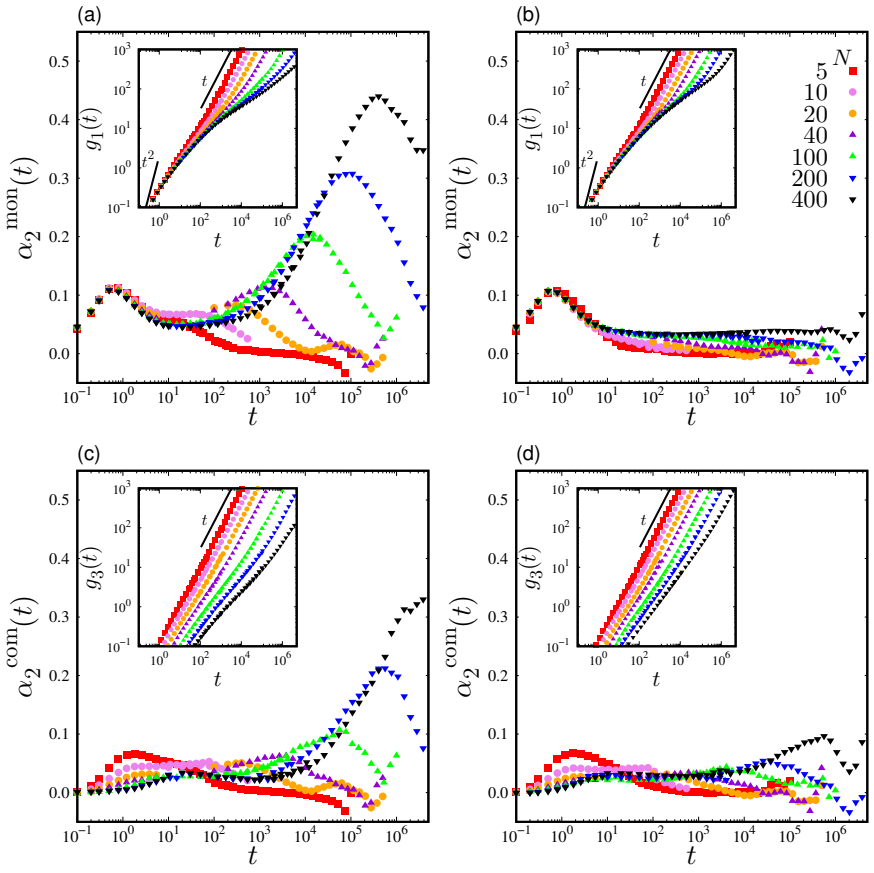

Figure 3.3: Non-Gaussian parameters of monomer beads $\alpha_2^{\rm mon}(t)$ and center-of-mass $\alpha_2^{\rm com}(t)$ for linear [(a) and (c)] and ring [(b) and (d)] polymers. Inset: Mean square displacements of monomer beads $\langle r^2(t)\rangle$ and the center-of-mass $\langle R^2(t)\rangle$. The dotted lines represent ballistic motion ($\sim t^2$) and diffusive behavior ($\sim t$).

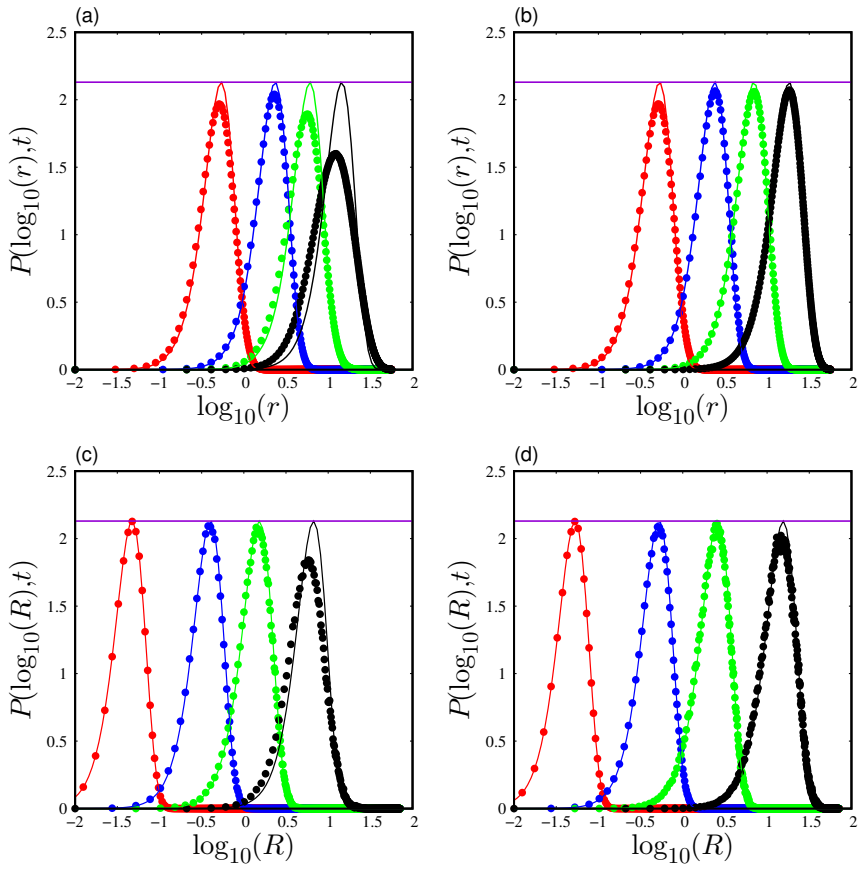

Figure 3.4: Probability distributions of the logarithm displacement of monomer beads and center-of-mass chains, $P(\log_{10}(r),t)$ and $P(\log_{10}(R),t)$, for linear [(a) and (c)] and ring [(b) and (d)] polymers with the chain length $N = 400$. The time t is chosen as $t = 1$, 10^2, 10^4, and 10^6 from left to right. The horizontal line denotes the Gaussian level, $\ln(10)\sqrt{54/\pi e^{-3/2}} \approx 2.13$. The solid curve represent the form using the Gaussian distribution, $G_s(r,t) = [3/(2\pi\langle r^2(t)\rangle)]^{3/2}\exp\left[-3r^2/(2\langle r^2(t)\rangle)\right]$ [(a) and (b)] and $G_s(R,t) = [3/(2\pi\langle R^2(t)\rangle)]^{3/2}\exp\left[-3R^2/(2\langle R^2(t)\rangle)\right]$ [(c) and (d)] at each time.

Chapter 4

Unraveling the Glass-like Dynamic Heterogeneity in Ring Polymer Melts: From Semiflexible to Stiff Chain

4.1 Introduction

The dynamic properties of polymers melts are governed by structural features, such as the chain length N and "topological constraints" (TCs) [1, 2]. In linear polymer melts, entanglement effects are common TCs and play a key role in describing the N dependence of the diffusion constant D. However, defining and characterizing TCs in ring polymers is still challenging due to the absence of chain ends [3, 17, 47, 54, 160, 161].

In ring polymer melts, the simple picture of TCs is that they inhibit each other's dynamics due to inter-ring "threadings" [5, 26, 62, 66]. As N increases, the number of threading configurations also increases, making it more difficult for the system to find the equilibrium configuration to relax the threading. The threading event of large N rings suggests a slowing-down of the dynamics, similar to the slow dynamics in glass-forming liquids, where cage effects are imposed by the local density environment [162]. The concept of "topological glass" has been used to understand the dynamics of ring polymer melts, highlighting the unique role of TCs in these systems compared to the entanglements in linear polymers [25, 27, 55, 67, 68, 155, 156, 159, 163–165]. Interestingly, techniques such as random pinning [68, 156] and activeness [25, 27, 165] have been introduced to

enhance the glassiness in ring polymers through molecular dynamics (MD) simulations.

Dynamic heterogeneity (DH) is a key concept used to describe the significant slowing-down of glass-former liquids as they approach the glass transition temperature [166–168]. The slowing-down is accompanied by the collective structural relaxation of spatially heterogeneous regions that exceeds the molecular size [132, 169–171]. DH is conventionally measured by the non-Gaussian parameter (NGP), i.e., the degree of the deviation from the Gaussian distribution for the molecular displacement within a given time interval [132, 134, 152, 172–174]. The NGP was utilized to quantify the non-Gaussianity in supercooled linear polymer melts [141–143]. In addition, we conducted calculations on the NGP for linear polymer melts by MD simulations using the Kremer–Grest (KG) bead-spring model [24]. The chain lengths varied from $N = 5$ to 400, and the monomer density was set at $\rho = 0.85$ (in the unit of σ^{-3} using the size of the bead σ). Our findings revealed that a notable increase in the peak of the NGP as N increases. This suggests that the dynamics of the system becomes spatially heterogeneous. However, note that the mechanism of non-Gaussianity in linear polymer melts is due to the enhanced mobility of chain ends, which is different from the cage effects observed in glass-forming liquids.

Michieletto *et al*. conducted MD simulations of ring polymers using the KG model and analyzed the center-of-mass (COM) displacement distribution [156]. They found that the non-Gaussian behavior was pronounced even in the absence of random pinning fields, when the monomer density ρ increased with the chain length $N = 500$. This finding is consistent with the experimental observation of polyethylene oxide ring melts by Brás *et al*. [15] However, our previous study, which also used the same model for MD simulations of ring polymer melts, showed that the NGP remained quite small at all time regimes, even when the chain length was increased up to $N = 400$ [24]. It should be noted that the chain stiffness differed between the two studies. Specifically, the bending potential $\varepsilon_\theta(1+\cos\theta)$ (in the unit of energy scale in the Lennard-Jones potential) acts on the bending angle θ formed by three consecutive monomer beads along the polymer chain (refer to Eq. (4.3)). Michieletto *et al*. utilized a stiff ring chain with the bending energy of $\varepsilon_\theta = 5$ for densities up to $\rho = 0.4$. More recently, the glass-like slow dynamics has also been demonstrated at low densities

by increasing the chain stiffness up to $\varepsilon_\theta = 20$ [28]. By contrast, we simulated semi-flexible ring chains with $\varepsilon_\theta = 1.5$ at a higher density of $\rho = 0.85$, which is the same as that used in the MD study by Halverson *et al*. [10, 11, 175]

Thus, there is still much to be explored regarding the influence of chain stiffness on DH in ring polymer melts. To address this gap, we performed MD simulations using the KG model by varying ε_θ and ρ. Our analysis began by examining the NGP, and characterized the effect of chain stiffness on the DH in ring polymer melts. We also investigated the conformation of ring chains by analyzing the radius of gyration, as well as asphericity and prolateness based on the diagonalization of the gyration tensor. Additionally, we introduced the concept of inter-molecular bonds virtually connected by ring COM positions, which enabled us to investigate the rearrangement of inter-molecular connectivity of ring polymers. By combining the results obtained from these analyses, we aim to identify similarities and differences in the effects of chain stiffness and monomer density on ring polymer dynamics.

4.2 Model and Methodology

We employed MD simulations for ring polymer melts utilizing the KG model [114]. Each ring polymer was represented by N monomer beads of mass m and diameter σ. Our system consisted of M polymer chains contained within a three-dimensional cubic box with volume of V and periodic boundary conditions. All monomer beads were subject to three types of inter-particle potentials, namely: the Lennard-Jones (LJ) potential, which acted between all pairs of monomer beads,

$$U_{\mathrm{LJ}}(\boldsymbol{r}) = 4\varepsilon_{\mathrm{LJ}}\left[\left(\frac{\sigma}{r}\right)^{12} - \left(\frac{\sigma}{r}\right)^{6}\right] + C. \tag{4.1}$$

Here r and $\varepsilon_{\mathrm{LJ}}$ represent the distance between two monomer beads and the energy scale of LJ potential, respectively. The LJ potential was truncated at the cut-off distance of $r_{\mathrm{c}} = 2^{1/6}\ \sigma$, and the constant C ensured that the potential energy shifted to zero at $r = r_{\mathrm{c}}$. Additionally, two adjacent

monomer beads along the chain also interacted via the bond potential

$$U_{\text{bond}}(r) = -\frac{1}{2}KR_0^2 \ln\left[1 - \left(\frac{r}{R_0}\right)^2\right], \tag{4.2}$$

for $r < R_0$, where K and R_0 represent the spring constant and the maximum length of the bond, respectively. Note that Eqs (4.1) and (4.2) define the finitely extensible nonlinear elastic (FENE) bond potential of the KG model. We adopted the values of $K = 30\ \varepsilon_{\text{LJ}}/\sigma^2$ and $R_0 = 1.5\ \sigma$. Lastly, we controlled the chain stiffness by incorporating a bending potential

$$U_{\text{bend}}(\theta) = \varepsilon_\theta[1 - \cos(\theta - \theta_0)], \tag{4.3}$$

where the bending angle θ is formed by three consecutive monomer beads along the polymer chain. In this study, we explored two bending energy cases: a semi-flexible chain with $\varepsilon_\theta = 1.5\varepsilon_{\text{LJ}}$ and a stiff chain with $\varepsilon_\theta = 5\varepsilon_{\text{LJ}}$ both with an equilibrium angle of $\theta_0 = 180°$.

We conducted MD simulations using the Large-scale Atomic/Molecular Massively Parallel Simulator (LAMMPS) [135]. Hereafter, the length, energy and time are conventionally represented in units of σ, ε_θ and $(m/\varepsilon_{\text{LJ}})^{1/2}$, respectively. Moreover, the temperature is also presented in units of $\varepsilon_{\text{LJ}}/k_{\text{B}}$, where k_{B} is Boltzmann constant.

We fixed the temperature T, chain length N, number of chains M as $T = 1.0$ and $N = 400$, and $M = 100$, respectively. During all simulations, the temperature was controlled using the Nosé–Hoover thermostat, with a time step of $\Delta t = 0.01$. We varied the monomer density $\rho\sigma^3$ $(= NM\sigma^3/V)$ as 0.1, 0.3, 0.4, 0.5, and 0.55 both for the semi-flexible and stiff chains. Besides, we adopted the monomer density $\rho = 0.85$ for the semi-flexible chain with $\varepsilon_\theta = 1.5$, which was a common choice for MD simulations both for linear [148, 176] and ring [10, 11, 24, 175, 177] polymers. It should be noted that a stiff chain system with $\varepsilon_\theta = 5$ displayed nematic ordering when the monomer densities exceeded $\rho = 0.55$, which is in agreement with the recent MD simulations reported in ref. 30. Therefore, the system of $\varepsilon_\theta = 5$ at $\rho = 0.85$ was excluded from the analysis. For each combination of ε_θ and ρ with the chain length $N = 1,000$, we calculated the Kuhn length l_{k} using $l_{\text{k}} = \langle R^2\rangle/l_{\text{b}}(N-1)$,

Table 4.1: Kuhn length l_k and entanglement length N_e by varying bending energy ε_θ and monomer dnesity ρ. (*: No entanglement effects were observed.)

ε_θ	ρ	l_k	N_e
1.5	0.1	4.1	*
1.5	0.3	3.8	121
1.5	0.4	3.7	85
1.5	0.5	3.0	60
1.5	0.55	3.0	59
1.5	0.85	2.8	28
5	0.1	10	*
5	0.3	7.8	32
5	0.4	7.2	24
5	0.5	6.4	19
5	0.55	6.4	15

in the linear chain melt [178]. Here, $\langle R^2 \rangle$ represents the mean square end-to-end distance of the chain, and $l_b \simeq 0.97$ denotes the average distance between two neighboring beads in the KG model. Another important characteristic is the entanglement length N_e, which we determined through the primitive path analysis [136, 137]. The values of l_k and N_e are presented in Table 4.1. Note that in previous studies, l_k was reported to be $l_k \simeq 2.79$ for $\varepsilon_\theta = 1.5$ at $\rho = 0.85$ and $l_k \simeq 10$ for $\varepsilon_\theta = 5$ at $\rho = 0.1$, respectively [10, 156]. Additionally, N_e was reported to be $N_e \simeq 28$ for $\varepsilon_\theta = 1.5$ at $\rho = 0.85$ and $N_e \simeq 40$ for $\varepsilon_\theta = 5$ at $\rho = 0.1$, respectively [68, 179]. However, we encountered difficulties in estimating N_e at the density $\rho = 0.1$ both for both $\varepsilon_\theta = 1.5$ and 5 due to the absence of entanglement effects with $N = 1,000$.

4.3 Results and Discussion

4.3.1 Mean Square Displacement and Non-Gaussian Parameter

We first analyzed the mean square displacement (MSD) of the COM of ring polymer chains and the NGP of the COM displacement distribution. The mean value of the even power of the COM

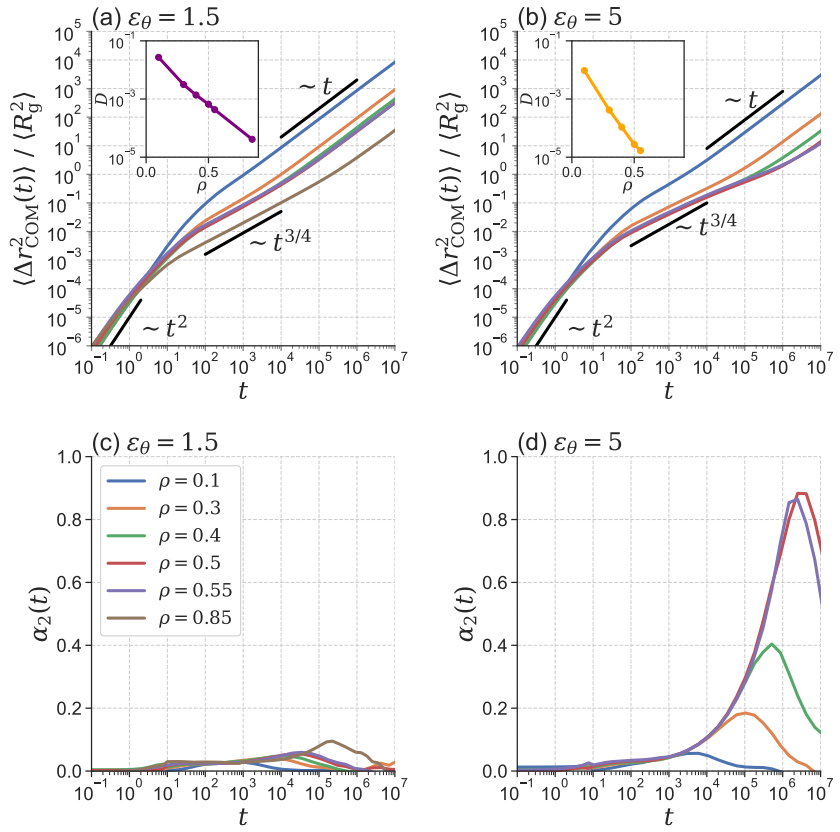

Figure 4.1: Monomer density ρ dependence of MSD $\langle \Delta r^2_{\mathrm{COM}}(t) \rangle$ and NGP $\alpha_2(t)$ for $\varepsilon_\theta = 1.5$ [(a) and (c)] and for $\varepsilon_\theta = 5$ [(b) and (d)], respectively. Note that MSD is scaled by mean square gyration of radius $\langle R^2_{\mathrm{g}} \rangle$. In (a) and (b), the ballistic, sub-diffusive, and diffusive behaviors, $\langle \Delta r^2_{\mathrm{COM}}(t) \rangle \sim t^\alpha$, are represented by black lines with $\alpha = 2$, $3/4$, and 1, respectively. Insets of (a) and (b): semi-log plots of the diffusion constant D as a function of the monomer density ρ, respectively. Note that the monomer density $\rho = 0.85$ was analyzed only for $\varepsilon_\theta = 1.5$.

displacement is defined by

$$\langle \Delta r^{2n}_{\mathrm{COM}}(t) \rangle = \left\langle \frac{1}{M} \sum_{m=1}^{M} |\boldsymbol{R}_m(t) - \boldsymbol{R}_m(0)|^{2n} \right\rangle, \quad (n = 1, 2, \cdots), \tag{4.4}$$

where $\boldsymbol{R}_m(t)$ represents the COM position of m-th polymer chain at time t. Here, $\langle \cdots \rangle$ denotes an average over the initial time. The second order with $n = 1$ corresponds to the MSD. Furthermore, the NGP for the center of mass (COM) displacement $\alpha_2(t)$ is defined by

$$\alpha_2(t) = \frac{3}{5} \frac{\langle \Delta r^4_{\mathrm{COM}}(t) \rangle}{\langle \Delta r^2_{\mathrm{COM}}(t) \rangle^2} - 1. \tag{4.5}$$

The NGP is a typical quantity to characterize DH in glass-forming liquids, which measures the non-Gaussianity, i.e., the degree of the deviation of the distribution function of the COM displacement from the Gaussian form during the time interval t.

The results of MSD and NGP are displayed in Fig. 4.1 by changing the monomer density ρ for $\varepsilon_\theta = 1.5$ [(a) and (c)] and $\varepsilon_\theta = 5$ [(b) and (d)], respectively. As the monomer density ρ increased, the diffusion of ring polymer chains significantly slowed down both for $\varepsilon_\theta = 1.5$ and 5. Moreover, at higher densities, the MSD exhibits a sub-diffusive behavior with $\langle \Delta r^2_{\mathrm{COM}}(t) \rangle \sim t^{3/4}$, followed by diffusion behavior observed at displacements larger than mean square gyration of radius $\langle R^2_{\mathrm{g}} \rangle$. The COM diffusion constant D was determined from the Einstein relation, $D = \lim_{t\to\infty} \langle \Delta r^2_{\mathrm{COM}}(t) \rangle / 6t$. The monomer density ρ dependence of D for $\varepsilon_\theta = 1.5$ and 5 is shown in the insets of Fig. 4.1(a) and (b), respectively. The reduction in diffusion was more pronounced for the stiff chains with $\varepsilon_\theta = 5$ compared to semi-flexible chains with $\varepsilon_\theta = 1.5$ at time scales corresponding to the onset of the diffusion process at the same monomer density. These observations are consistent with the calculations by Michieletto *et al*. [156] and Halverson *et al*. [11] The mean square radius of gyration $\langle R^2_{\mathrm{g}} \rangle$ will be discussed in the next subsection with respect to Fig. 4.2.

As demonstrated in Fig. 4.1(c), the NGP's value of semi-flexible ring chains with $\varepsilon_\theta = 1.5$ remained relatively small ($\alpha_2(t) \lesssim 0.1$) at all investigated times and densities. This suggests that the distribution of the COM displacement $|\boldsymbol{R}_m(t) - \boldsymbol{R}_m(0)|$ follows a Gaussian distribution, which was previously reported in our work. [24] The observation of Gaussian behavior in semi-flexible ring polymers, even at the dense melt density of $\rho = 0.85$, is noteworthy and provides a unique perspective on the dynamics of ring polymers. By contrast, for stiff ring chains, the increase in $\alpha_2(t)$ was more significant, showing peaks in a long time regime that approximately corresponded to the onset time scale of the diffusive behavior with $\langle \Delta r^2_{\mathrm{COM}}(t) \rangle \sim t$, as demonstrated in Fig. 4.1(b) and (d). Namely, the DH was found to be more pronounced in stiff ring chains with $\varepsilon_\theta = 5$, similar to common observations in glass-forming liquids. An analogous glass-like heterogeneous dynamics was reported by Michieletto *et al.*, who analyzed the displacement distribution of stiff ring chains with $\varepsilon_\theta = 5$ up to $\rho = 0.4$ with $N = 500$ [156]. Therefore, the contracting observations in the NGP

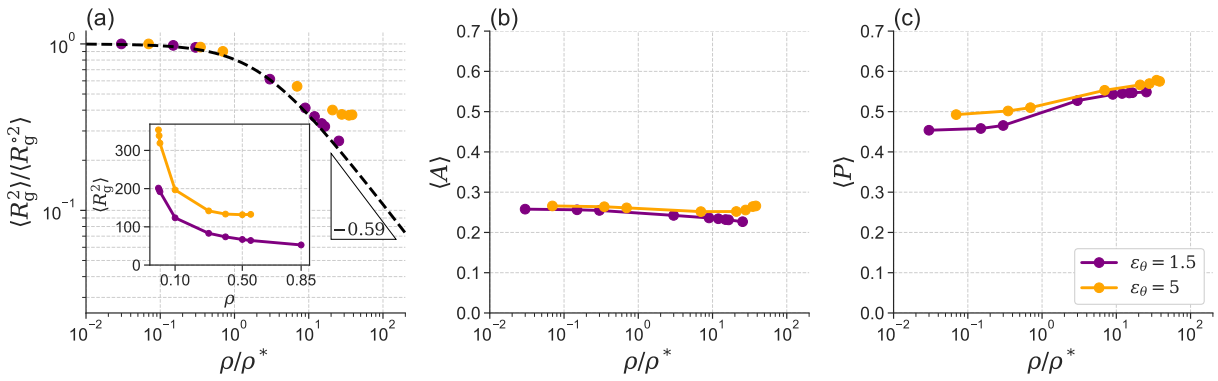

Figure 4.2: Monomer density ρ dependence of chain conformation characteristics: (a) mean square radius of gyration $\langle R_g^2\rangle/\langle R_g^{\circ 2}\rangle$, (b) asphericity A, and (c) prolateness P. In (a), the mean square radius of gyration is normalized by $\langle R_g^{\circ 2}\rangle$, which represents the mean square radius of gyration at a density of $\rho = 0.001$. The raw data of $\langle R_g^2\rangle$ as a function of ρ is also shown in Inset of panel (a). The black dotted line in (a) is the master curve, $\langle R_g^2\rangle/\langle R_g^{\circ 2}\rangle = [1 + 0.45(\rho/\rho^*)]^{-0.59}$. In each panel, the density is scaled density $\rho^* = 3N/(4\pi\langle R_g^{\circ 2}\rangle^{3/2})$.

call for further investigations into the COM mobility, which could entail significant differences between semi-flexible and stiff ring chains.

4.3.2 Conformation of the Ring Chains: Radius of Gyration, Asphericity and Prolateness

It is important to examine the details regarding the conformation of rings and its relationship with the DH both for semi-flexible and stiff chain. The radius of gyration provides a measure of the size of polymer chains. To gain a more sophisticated understanding of the shapes, the principal components the gyration tensor $\boldsymbol{I}$ can be utilized, which allows for examination of the asphericity and prolateness of the polymer chains [180–183]. The gyration tensor for each ring chain is defined as $I_{\alpha\beta} = N^{-1}\sum_{i=1}^{N}\sum_{j=1}^{N}(\alpha_i - \alpha_j)(\beta_i - \beta_j)$, where α_i represents the α element of i-th bead with α, β $(= x, y, z)$. Here, the square radius of gyration R_g^2 can be calculated as the summation of the eigenvalues λ_i $(i = 1, 2, 3)$ of the gyration tensor $\boldsymbol{I}$ as $R_g^2 = \lambda_1 + \lambda_2 + \lambda_3$, where the principle axes of inertia are chosen such that the diagonal elements are ordered as $\lambda_1 \geq \lambda_2 \geq \lambda_3$. Furthermore, the

asphericity A and prolateness P were calculated from the following equations:

$$A = \frac{(\lambda_1 - \lambda_2)^2 + (\lambda_1 - \lambda_3)^2 + (\lambda_2 - \lambda_3)^2}{2(\lambda_1 + \lambda_2 + \lambda_3)^2}, \tag{4.6}$$

$$P = \frac{(2\lambda_1 - \lambda_2 - \lambda_3)(2\lambda_2 - \lambda_1 - \lambda_3)(2\lambda_3 - \lambda_1 - \lambda_2)}{2\left(\lambda_1^2 + \lambda_2^2 + \lambda_3^2 - \lambda_1\lambda_2 - \lambda_1\lambda_3 - \lambda_2\lambda_3\right)^{3/2}}. \tag{4.7}$$

The asphericity takes on values of $0 \leq A \leq 1$, where $A = 0$ corresponds to spherically symmetric object, and $A = 1$ corresponds to a polymer that is fully extended to form a rigid rod shape. The prolateness P is bounded between -1 and 1, where $P = -1$ represents a fully oblate object such as a disk, and $P = 1$ represents a prolate object in the shape of a rigid rod. The gyration tensor was calculated for each chain and the time evolutions of R_g^2, A, P were computed. The mean values $\langle R_g^2 \rangle$, $\langle A \rangle$ and $\langle P \rangle$ were evaluated by taking the average of these quantities over the time series data for each chain. It should be noted that the analysis of the gyration tensor was performed in various simulations of ring polymers [29, 49, 183–188].

Reigh and Yoon reported a universal scaling behavior of $\langle R_g^2 \rangle \sim \rho^{-0.59}$ for long ring polymers by Monte Carlo simulation of a lattice model [49]. This exponent -0.59 is significantly different from the value of -0.25 observed for linear polymers, which was a well-established prediction based on scaling arguments. This observation suggests ring chains form more compact conformations than linear chains. More recently, Cai *et al.* performed MD simulations of ring polymers using the KG model by varying chain lengths N up to 5120, and reported the same scaling behavior of $\langle R_g^2 \rangle \sim \rho^{-0.59}$ [29]. The master curve was heuristically proposed and given by

$$\langle R_g^2 \rangle / \langle R_g^{\circ 2} \rangle = [1 + 0.45(\rho/\rho^*)]^{-0.59}, \tag{4.8}$$

where $\langle R_g^{\circ 2} \rangle$ denotes the mean square radius of gyration in the dilute solutions. In addition, ρ^* corresponds to the overlap density defined by $\rho^* = 3N/(4\pi \langle R_g^{\circ 2} \rangle^{3/2})$. They also compared their simulation results with available experimental data, and found good agreement between simulations and experiments. Note that the ring polymer chains in their simulations were fully flexible because

they did not incorporate any bending potentials.

Figure 4.2(a) shows the relative mean square radii of gyration $\langle R_g^2 \rangle / \langle R_g^{\circ 2} \rangle$ as a function of the scaled density ρ/ρ^*. We estimated $\langle R_g^{\circ 2} \rangle$ as the value of mean square radii of gyration $\langle R_g^2 \rangle$ both for semi-flexible and stiff chains at a density of $\rho = 0.001$. This density corresponds to a sufficiently low scaled density ($\rho/\rho^* < 10^{-1}$), making it appropriate to consider $\rho = 0.001$ as a dilute solution both for semi-flexible and stiff ring polymers. The data for semi-flexible rings with $\varepsilon_\theta = 1.5$ follow the master curve given by Eq. (4.8). However, a deviation from Eq. (4.8) was observed for stiff rings with $\varepsilon_\theta = 5$, indicating that $\langle R_g^2 \rangle$ of stiff ring chains decreases slightly slower than that of semi-flexible ring chains as the density is increased beyond $\rho/\rho^* \gtrsim 10$. The inset in Fig. 4.2 (a) shows the density ρ dependence of the mean square radii of gyrations $\langle R_g^2 \rangle$. This represents that the stiff rings are larger than semi-flexible ones in all densities ρ.

Figure 4.2(b) and (c) show the average asphericity $\langle A \rangle$ and average prolateness $\langle P \rangle$, respectively, as functions of ρ/ρ^*. Interestingly, we found that the values of $\langle A \rangle$ and $\langle P \rangle$ approached saturation regardless of the bending energy ε_θ. In particular, the relatively small values of $\langle A \rangle \simeq 0.2$ suggest that the ring polymer adopt globular conformations, which remain valid across the densities examined. However, slightly large values of $\langle P \rangle \simeq 0.5$ indicate that the rings extend moderately in the direction of longest inertia axis. These imply that the shape of the rings is alomost spherical and relatively insensitive to both ε_θ and ρ, provided that the chain length is sufficiently long compared to the Kuhn length scale.

4.3.3 Inter-penetration of Ring Chains

As shown in Fig. 4.2, while the shape of the polymer remained largely unchanged on average, there was a increase in the mean square radius of gyration $\langle R_g^2 \rangle$ when the chain stiffness increased to $\varepsilon_\theta = 5$. This suggests that the inter-molecular connectivity of ring chains may differs significantly between semi-flexible and stiff chains. To explore this further, we calculated the radial distribution function for the COM of ring chains $g(r)$, and the results are presented in Fig. 4.3 as a function of the scaled length of $r/\langle R_g^2 \rangle^{1/2}$.

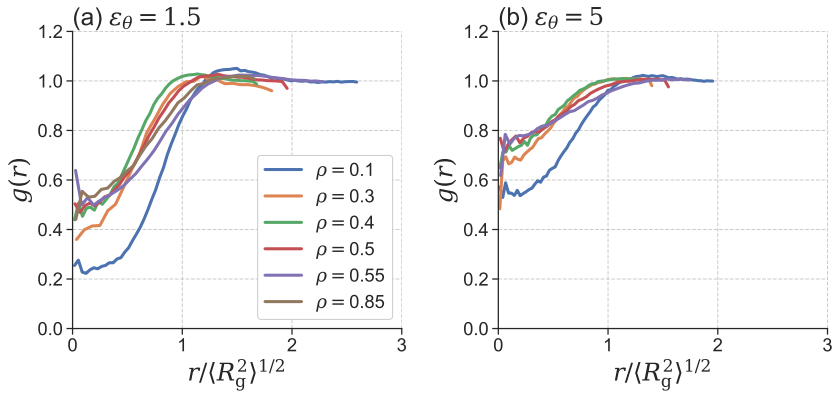

Figure 4.3: Radial distribution function $g(r)$ for COM of ring polymers as a function of the scaled distance $r/\langle R_g^2 \rangle^{1/2}$. Results are shown for $\varepsilon_\theta = 1.5$ (a) and $\varepsilon_\theta = 5$ (b).

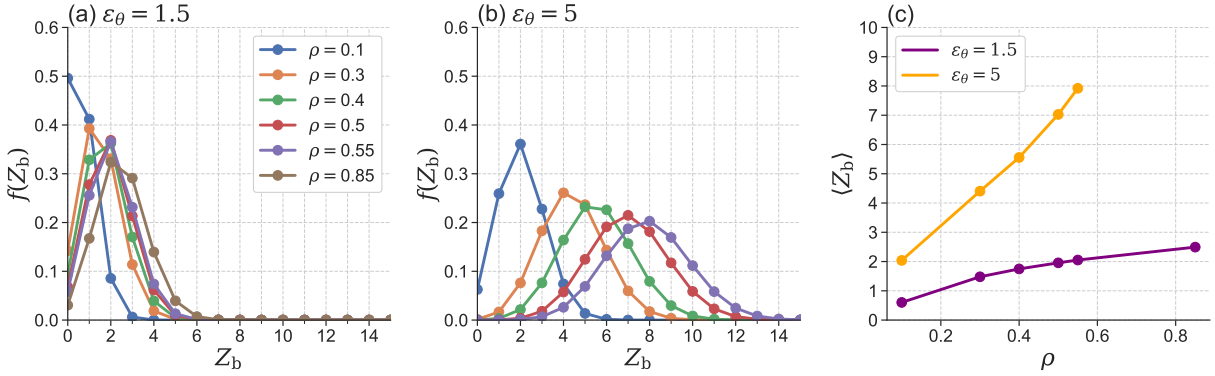

Figure 4.4: Probability distributions of the number of virtual bonds, $f(Z_b)$, for ring polymers of $\varepsilon_\theta = 1.5$ (a) and $\varepsilon_\theta = 5$ (b). The virtual bonds are defined based on Eq. (4.9). Panel (c) shows the monomer density ρ dependence of the mean value of Z_b.

As observed in Fig. 4.3, $g(r)$ allowed us to characterize the degree of inter-penetration of ring polymers. In fact, we did not observe a pronounced peak of $g(r)$, but instead found finite values at the length scale of $r < \langle R_g^2 \rangle^{1/2}$, indicating that there is some degree of inter-penetration between the ring chains. The $g(r)$ became more broad with increasing the monomer density, suggesting that the chains are less separated from each other. Similar results of $g(r)$ were reported for flexible chains without the bending potential by Cai *et al.* [29] Additionally, as shown in Fig. 4.3(b), the degree of the inter-penetration became more significant as the bending energy increased to $\varepsilon_\theta = 5$. This observation is consistent with the larger mean square radius of gyration $\langle R_g^2 \rangle$ of stiff rings with $\varepsilon_\theta = 5$

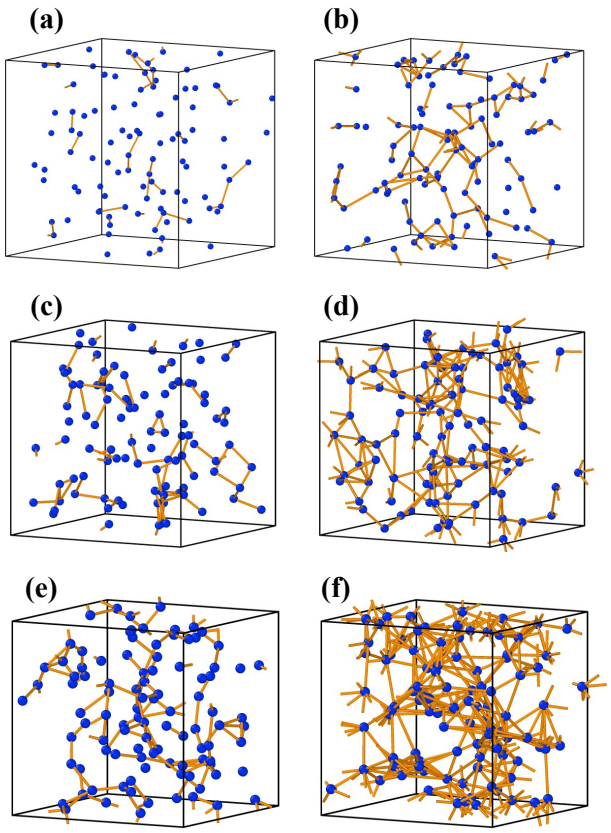

Figure 4.5: Visualization of virtual bonds (yellow lines) between the COM of rings (blue spheres) for $\varepsilon_\theta = 1.5$ [(a), (c) and (e)] and $\varepsilon_\theta = 5$ [(b), (d) and (f)]. The monomer density ρ increases as $\rho = 0.1$, 0.3, and 0.5 from top to bottom.

compared to that of semi-flexible rings of $\varepsilon_\theta = 1.5$ at the same density ρ. The difference in $\langle R_g^2 \rangle$ is also evident in Fig. 4.2, where the curve for $\varepsilon_\theta = 5$ is shifted to higher values of ρ/ρ^* compared to $\varepsilon_\theta = 1.5$. These results suggest that the competition between repulsive forces inside the ring and from adjacent rings plays a crucial role in determining the loop structure. While sufficiently semi-flexible polymers tend to be more compact because the repulsion between neighboring rings overcomes the monomer bead repulsion inside a single chain, the stiff polymers tend to expand due to the long Kuhn length, leading to the inter-penetration of rings.

To analyze the number of inter-molecular connectivity, we considered virtually connected bonds between the COM of ring chains. In particular, for two polymers i and j with the COM positions

$\boldsymbol{r}_i$ and $\boldsymbol{r}_j$, they were considered to be virtually bonded if

$$r_{ij} < A_1 \langle R_g^2 \rangle^{1/2}, \tag{4.9}$$

with the value of $A_1 = 1$. Here, $r_{ij} = |\boldsymbol{R}_i - \boldsymbol{R}_j|$ is the distance between these COM. For each polymer, the number of virtual bonds Z_b, which represents the static coordination number, was counted. Figure 4.4 depicts the probability distribution $f(Z_b)$ for ring polymers of $\varepsilon_\theta = 1.5$ (a) and $\varepsilon_\theta = 5$ (b) at varying the density ρ. In the case of semi-flexible rings with $\varepsilon_\theta = 1.5$, the peak was observed at around 2 for most densities, except for $\rho = 0.1$, where Z_b was predominantly 0, indicating that each ring chain was mostly isolated and did not correlated with each other. However, for stiff rings with $\varepsilon_\theta = 5$, we observed an increase in the peak position and width of $f(Z_b)$ as the density ρ increased. The monomer density ρ dependence of the mean value of Z_b is shown in Fig. 4.4(c). Here, $\langle Z_b \rangle$ can be evaluated by

$$\langle Z_b \rangle = \int_0^{\langle R_g^2 \rangle^{1/2}} 4\pi r^2 \left(\frac{\rho}{N}\right) g(r) dr. \tag{4.10}$$

In cases of $g(r) = 1$ and $\langle R_g^2 \rangle \sim \rho^{-0.6}$, $\langle Z_b \rangle$ may exhibit a scaling behavior of $\langle Z_b \rangle \sim \rho \langle R_g^2 \rangle^{3/2} \sim \rho^{0.1}$ at a fixed chain length N. This suggests that $\langle Z_b \rangle$ increases slowly as the density increases. However, the presence of $g(r) < 1$ for $r < \langle R_g^2 \rangle^{1/2}$, as observed in Fig. 4.3 both for $\varepsilon_\theta = 1.5$ and 5, leads to the deviates from the expected $\langle Z_b \rangle \sim \rho^{0.1}$. Notably, as shown in Fig. 4.2(a), $\langle R_g^2 \rangle$ of $\varepsilon_\theta = 5$ does not follow the $\langle R_g^2 \rangle \sim \rho^{-0.6}$ scaling, resulting in a more pronounced increase in $\langle Z_b \rangle$ with increasing the density.

Moreover, the spatial distribution of inter-molecular connectivity is visualized in Fig. 4.5. For semi-flexible ring polymers with $\varepsilon_\theta = 1.5$, bonds describing the connectivity of COM are sparse irrespective of the monomer density ρ. In contrast, as the density increases, ring polymers with higher stiffness ($\varepsilon_\theta = 5$) exhibit a stronger percolation, indicating a more interconnected network bond. It is noteworthy that there exists a critical coordination number around 3, beyond which the linked ring polymers percolate through the entire system [189].

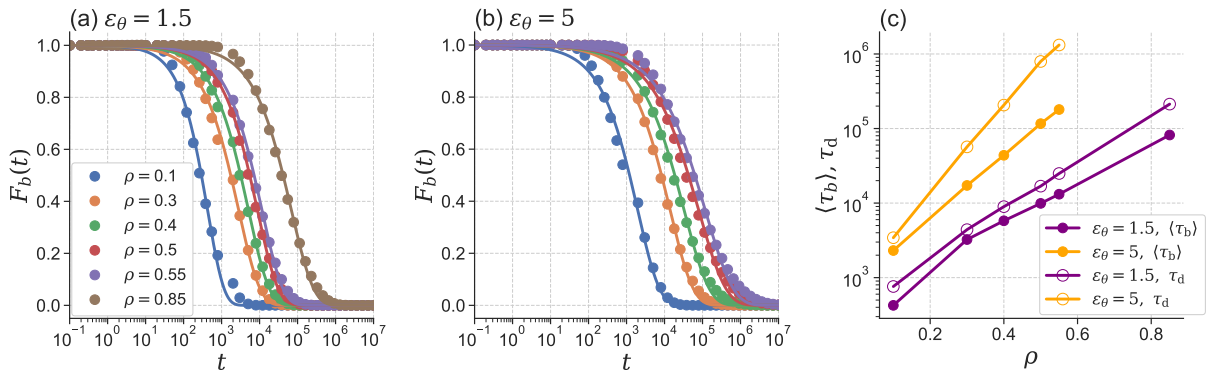

Figure 4.6: Monomer density dependence of the bond correlation function $F_b(t)$ for $\varepsilon_\theta = 1.5$ (a) and $\varepsilon_\theta = 5$ (b), respectively. The solid line represents the fitting result obtained using the stretched exponential function, $F_b(t) \approx \exp\left[-(t/\tau_b)^\beta\right]$. Panel (c) shows the monomer density ρ dependence of the average relaxation time $\langle \tau_b \rangle$ of the bond correlation function $F_b(t)$ and the diffusion time $\tau_d = \langle R_g^2 \rangle / 6D$.

4.3.4 Rearrangements of Inter-molecular Connectivity

To examine rearrangements of inter-molecular connectivity of ring polymers, we analyzed the time evolution of virtual bonds. This reflects the exchange of initially bonded neighbors because the COM motion breaks old bonds and forms new ones. Although the average coordination number $\langle Z_b \rangle$ may remain constant, the neighboring COMs will be replaced with the new ones, thereby reshaping the cages around a tagged COM. A similar methodology, known as the bond-breakage method, is used to study the DH observed in glass-forming liquids [170, 190–193].

The virtual bond between two polymers i and j which had been counted to be formed at an initial time 0 through Eq. (4.9) was considered broken when

$$r_{ij}(t) > A_2 \langle R_g^2 \rangle^{1/2}, \tag{4.11}$$

after a time interval of t. To ensure bond-breaking insensitive to thermal fluctuations, the threshold value of $A_2 = 1.2$ was set slightly larger than A_1=1. The total number of surviving bonds, $N_b(t)$, was calculated from the initial time 0. The bond correlation function, $F_b(t) = \langle N_b(t)/N_b(0) \rangle$, was obtained by averaging over the configurations at $t = 0$. Figure 4.6 shows the results of $F_b(t)$ for

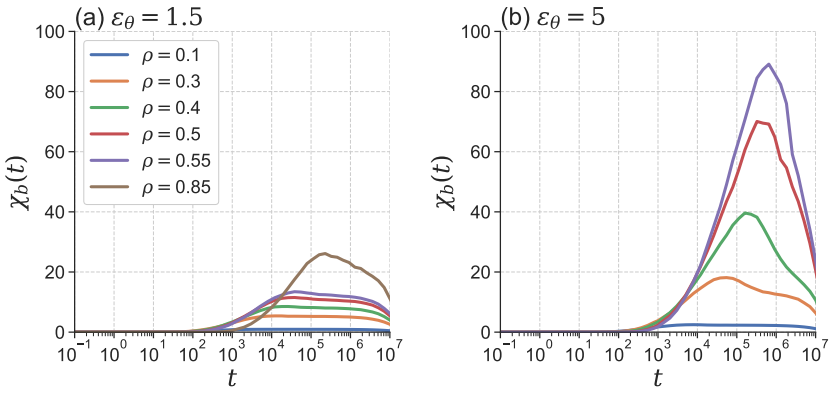

Figure 4.7: Monomer density dependence of the dynamic susceptibility of bond-breakage $\chi_{\mathrm{b}}(t)$ for $\varepsilon_\theta = 1.5$ (a) and $\varepsilon_\theta = 5$ (b), respectively.

$\varepsilon_\theta = 1.5$ (a) and $\varepsilon_\theta = 5$ (b), respectively. The characteristic time scale of $F_{\mathrm{b}}(t)$ is related to that of the rearrangement of the local coordination by the neighboring COMs, according to the definition of the bond. The $F_{\mathrm{b}}(t)$ was fitted to the stretched exponential function $F_b(t) = \exp\left[-(t/\tau_{\mathrm{b}})^{\beta}\right]$, where the exponent β represents the degree of the deviation from the exponential decay with $\beta = 1$. The average relaxation time $\langle\tau_{\mathrm{b}}\rangle$ was then calculated from $\langle\tau_{\mathrm{b}}\rangle = \int_0^\infty F_b(t)dt$, and estimated by $\langle\tau_{\mathrm{b}}\rangle = (\tau_{\mathrm{b}}/\beta)\Gamma(1/\beta)$ with the Gamma function $\Gamma(\cdots)$. Figure 4.6(c) shows $\langle\tau_{\mathrm{b}}\rangle$ as a function of the monomer density ρ. Our results demonstrate the increase in the average relaxation time $\langle\tau_{\mathrm{b}}\rangle$ of $F_{\mathrm{b}}(t)$ as the monomer density ρ increased, both for $\varepsilon_\theta = 1.5$ and $\varepsilon_\theta = 5$. The increase in $\langle\tau_{\mathrm{b}}\rangle$ apparently obeys an exponential trend as a function of ρ, except at the dilute density of $\rho = 0.1$ for $\varepsilon_\theta = 1.5$, where the average coordination number $\langle Z_{\mathrm{b}}\rangle$ is less than 1, indicating that polymer rings are nearly isolated (see Fig. 4.4(c)). Furthermore, we observed a more pronounced increase in $\langle\tau_{\mathrm{b}}\rangle$ for stiff ring polymers with $\varepsilon_\theta = 5$, which is in accordance with the monomer density ρ dependence of $\langle Z_{\mathrm{b}}\rangle$ (see again Fig. 4.4(c)).

Another significant time scale to consider is the diffusion time, τ_{d}, defined as $\tau_{\mathrm{d}} = \langle R_{\mathrm{g}}^2\rangle/6D$, which corresponds to the time at which the MSD reaches the length scale of the mean square radius of gyration $\langle R_{\mathrm{g}}^2\rangle$. The monomer density dependence of τ_{d} is illustrated in Fig. 4.6(c). It is observed that for semi-flexible rings with $\varepsilon_\theta = 1.5$, τ_{d} increases in a similar manner to $\langle\tau_{\mathrm{b}}\rangle$, while for stiff rings with $\varepsilon_\theta = 5$, τ_{d} exhibits a significant increase and becomes decoupled from $\langle\tau_{\mathrm{b}}\rangle$ as

the density ρ increases. These observations suggest the COM diffusion of stiff rings is not solely driven by local bond rearrangements, but requires a cooperative mechanism.

We then examined the collective effects of bond rearrangements in ring polymers. For this purpose, the dynamic susceptibility of bond-breakage was calculated by the fluctuation function of the number of broken-bonds at different time intervals, t [191]. The number of the breakage-bond $B_i(t)$ between two times 0 and t for the i-th polymer was counted based on the conditions given in Eqs. (4.9) and (4.11). The degree of bond-breakage correlations can be characterized by the susceptibility $\chi_{\mathrm{b}}(t)$, which is defined as

$$\chi_{\mathrm{b}}(t) = \frac{1}{M}\left\langle \sum_{i=1}^{M}\sum_{j=1}^{M} \delta B_i(t)\delta B_j(t) \right\rangle, \tag{4.12}$$

where $\delta B_i(t) = B_i(t)/2 - \langle B(t)\rangle$ represents the deviation from the average number of broken bonds. The average number of broken bonds can be estimated as $\langle B(t)\rangle = \langle \sum_{i=1}^{M} B_i(t)/2\rangle/M$. Note that the factor 1/2 avoided double-counting of the bond-breakage between polymers i and j. Figure 4.7 illustrates the susceptibility of bond-breakage, $\chi_{\mathrm{b}}(t)$, for different values of ε_θ and ρ. For semi-flexible rings with $\varepsilon_\theta = 1.5$, the $\chi_{\mathrm{b}}(t)$ shows relatively small values, whereas the peak of χ_{b} became pronounced ($\chi_{\mathrm{b}} \sim 30$) at the highest density $\rho = 0.85$ investigated. In contrast, for stiff rings with $\varepsilon_\theta = 5$, the peaks show significant development with increasing monomer density, particularly at the time regimes where the MSD nearly reaches the diffusive behavior. At the density of $\rho = 0.55$, the peak height reaches $\chi_{\mathrm{b}} \sim 90$. Therefore, the observed NGP behavior in Fig. 4.1(c) and (d) is related to DH, which is also characterized by the bond-breakage susceptibility, $\chi_{\mathrm{b}}(t)$. Interestingly, the results of $\alpha_2(t)$ and $\chi_{\mathrm{b}}(t)$ suggest that ring polymers with $\varepsilon_\theta = 1.5$ exhibit spatial homogeneous dynamics, even in the sub-diffusion regime. In this perspective, the inter-chain interactions in semi-flexible ring polymer melts display notable characteristics, while stiff ring polymer melts exhibit interactions reminiscent of "entanglements" in linear polymer melts.

Mei *et al.* have recently developed the polymer interaction site model (PRISM) as a microscopic theory for dense ring polymer melts [20, 194]. This theory proposes a partially inter-penetrating,

two-step fractal structure model for each ring chain and provides a master curve for the chain length N dependence of the COM diffusion constant D. Although the PRISM theory has shown good agreement with MD simulations data for semi-flexible ring polymers with ε_θ = 1.5 [11], deviations from the master curve have been observed for stiff rings of ε_θ = 5 [156]. To gain a deeper understanding of the underlying mechanism of emergence of DH in ring polymers melts, a combined effort between theory and simulation may be necessary. In particular, our MD simulation results analyzing DH can provide insights into the deviation from the master curves reported in ref. 20, and may facilitate a generalization of the theory by incorporating an activated hopping process [23].

4.4 Conclusion

In conclusion, our MD simulations of ring polymer melts using the KG model have provided insights into the dynamics of semi-flexible and stiff ring chains. By analyzing the NGP in the distribution of the COM displacement, we have found that more stiff ring chains exhibit a peak in the NGP in long time regimes, which increases with the monomer density. This suggests that the dynamics of stiff ring chains are affected by strong inter-molecular interactions and that the motion of the COM is correlated with each other. In contrast, more semi-flexible ring polymers exhibit relatively small non-Gaussianity, indicating that the COM mobility is almost uncorrelated with each other. The difference in non-Gaussianity between the two types of ring polymers suggests that the nature of the inter-molecular interactions changes significantly depending on the degree of chain stiffness.

The behavior of the radius of gyration R_g in relation to ρ depends on the stiffness of the ring polymer chains. In the case of more semi-flexible rings, the R_g follows a master curve described by Eq. (4.8). However, this curve does not apply to stiff ring polymer melts. The deviation from the master curve can be explained by the competition between the shrinkage caused by the excluded volume of neighboring polymers and the expansion due to the chain stiffness. Specifically, semi-

flexible ring polymers tend to adopt a compact globule conformation due to the excluded volume interaction with their neighbors, while more stiff rings expand due to the long Kuhn length.

We have also analyzed the dynamics of bond-breakage between the COM of rings defined by using averaged radius of gyration, $\langle R_g^2 \rangle^{1/2}$. The network of virtual bonds in stiff rings are percolating, while those in semi-flexible rings are sparsely distributed. Furthermore, the results for the dynamic susceptibility of bond-breakage are consistent with the non-Gaussianity in the displacement distribution, indicating that the DH of bond-breakage is coupled with the non-Gaussianity in diffusion in ring polymer melts. Furthermore, it is crucial to investigate the dynamics of ring-linear blend melts [137, 195–198]. In practical terms, the analysis of the bond-breakage is particularly well-suited for this system, enabling the assessment of the inter-connectivity dynamics of polymer chain COMs.

Threading is commonly discussed in ring polymer melts, but the relationship with the bond-breakage dynamics remains unclear. Further investigation into the properties of threading in ring polymer melts with varying chain stiffness is warranted. Finally, we have found that semi-flexible ring polymers exhibit sub-diffusion yet Gaussian distribution with unique dynamics. We suggest that the microscopic theory based on the PRISM for ring polymer melts will be useful for understanding the diffusion mechanisms of these systems. Drawing on another crucial insight from ref. 189, we put forward the notion that the value of $\langle Z_b \rangle = 3$ acts as a threshold for the percolation of virtual bond networks and the emergence of DH in ring polymers. To gain deeper insights, further analysis is required, including the cluster size distribution by varying the chain stiffness ε_θ and extending the study to longer chain length N. Currently, we are pursuing the application of persistent homology analysis to explore this perspective further [66].

Chapter 5

Persistent Homology Reveals the Origin of Topological Glasses in Ring Polymer Melts

5.1 Introduction

Ring polymers exhibit distinctive properties compared to their linear counterparts [3, 5, 54, 199]. One key feature thought to define topological constraints in ring polymers is the interpenetrating structure known as "threading". Threading occurs when one ring polymer penetrates the loop of another ring polymer, with the penetrating ring classified as active and the penetrated ring as passive, illustrating the asymmetric and hierarchical nature of the threading network. For sufficiently long rings, this threading network can evolve, eventually leading to the formation of "topological glasses," where the relaxation time is expected to increase drastically with respect to the extent of threading [55, 67, 68, 163].

Analyzing threading and clarifying its relationship with glass-like properties is crucial. While several approaches for quantifying threading have been proposed, including methods based on minimal surface [62, 63] and geometric analysis [64, 65], Landuzzi et al. introduced a method for quantifying the threading of ring polymers using persistent homology (PH) [66]. PH is a mathematical tool that characterize topological features such as "loops" from point cloud [200–202]. Specifically, Landuzzi et al. investigated threading structures using PH from MD simulations with the Kremer–Grest (KG) model [114] for ring polymers. Of particular interest was the chain length N dependence of ring polymers up to $N = 2048$ at a monomer number density of 0.1, incorporating

a bending potential $U_{\mathrm{bend}}(\theta) = \varepsilon_\theta(1 + \cos\theta)$, where θ represents the angle formed by consecutive bonds and $\varepsilon_\theta = 5$ (see Eq. (5.3) for details). This bending potential effectively models the polymers as worm-like chains, analogous to the Kratky–Porod model [203].

We recently performed MD simulations using the KG with two types of ring polymers: semi-flexible ($\varepsilon_\theta = 1.5$) and stiff ($\varepsilon_\theta = 5$) rings with a fixed chain length $N = 400$ to investigate the influence of chain stiffness on their dynamic properties [204]. The rearrangement dynamics of the center of mass (COM) were analyzed, with a focus on dynamic heterogeneity to clarify glassy behavior. Our results demonstrated that stiff ring polymers exhibit pronounced glassy behavior accompanied by dynamic heterogeneity, whereas semi-flexible ring polymers display homogeneous dynamics characterized by a Gaussian distribution of COM displacement. This distinction suggests that the dynamic properties of ring polymers are fundamentally influenced by the chain stiffness, emphasizing the need to examine threading structures across varying degrees of chain stiffness.

The purpose of this study is to elucidate the influence of the chain stiffness and monomer number density of ring polymers on their threading structures. We first analyze the connectivity of COM using PH. Subsequently, we characterize the active and passive threading structures between pairs of ring chains through PH. Through these analyses, we clarify the topological characteristics of ring polymers and their relationship to glassy behavior, informed by insights gained from the rearrangement dynamics of COM.

5.2 Methods

We employed MD simulations for ring polymer melts utilizing the KG model. Each ring polymer is represented by N monomer beads, each with mass m and diameter σ. The system comprises M ring chains contained within a three-dimensional cubic box with volume of V, with periodic boundary conditions. The monomer beads interact through three types of inter-particle potentials: the Lennard-Jones (LJ) potential governs the interaction between all pairs of monomer beads and

is defined as

$$U_{\mathrm{LJ}}(r) = 4\varepsilon_{\mathrm{LJ}}\left[\left(\frac{\sigma}{r}\right)^{12} - \left(\frac{\sigma}{r}\right)^{6}\right] + C, \tag{5.1}$$

where r is the distance between two beads, $\varepsilon_{\mathrm{LJ}}$ is the depth of the potential well, and C is a constant that shifts the potential at the cut-off distance of $r_{\mathrm{c}} = 2^{1/6}\,\sigma$. Two adjacent monomer beads along the chain also interacted via the finitely extensible nonlinear elastic (FENE) bond potential

$$U_{\mathrm{LENE}}(r) = -\frac{1}{2}KR_0^2 \ln\left[1 - \left(\frac{r}{R_0}\right)^2\right], \tag{5.2}$$

for $r < R_0$, where K and R_0 represent the spring constant and the maximum length of the bond, respectively. We used the values of $K = 30\varepsilon_{\mathrm{LJ}}/\sigma^2$ and $R_0 = 1.5\sigma$. Lastly, the chain stiffness is controlled by incorporating a bending potential

$$U_{\mathrm{bend}}(\theta) = \varepsilon_\theta[1 - \cos(\theta - \theta_0)], \tag{5.3}$$

where θ is the bending angle formed by three consecutive monomer beads along the polymer chain. In this study, the bending energy was set as $\varepsilon_\theta/\varepsilon_{\mathrm{LJ}} = 0$, 1.5, 2, 3, 4, and 5, with an equilibrium angle of $\theta_0 = 180°$.

All MD simulations were performed using the Large-scale Atomic/Molecular Massively Parallel Simulator (LAMMPS) [135]. Length, energy and time are represented in units of σ, ε_θ and $(m/\varepsilon_{\mathrm{LJ}})^{1/2}$, respectively. Additionally, the temperature is expressed in units of $\varepsilon_{\mathrm{LJ}}/k_{\mathrm{B}}$, where k_{B} is Boltzmann constant. We fixed the temperature T, chain length N, number of chains M as $T = 1.0$ and $N = 400$, and $M = 100$, respectively. Throughout the simulations, temperature was controlled using the Nosé–Hoover thermostat, with a time step of $\Delta t = 0.01$. The monomer number density $\rho\sigma^3$ $(= NM\sigma^3/V)$ was varied as 0.1, 0.2, 0.3, 0.4, and 0.5 for each degree of chain stiffness. Henceforth, ρ will be referred to as density.

Here, we briefly outline PH: A set of coordinates such as beads of chains or COM, denoted as $\{\boldsymbol{r}\} = \{\boldsymbol{r}_1, \boldsymbol{r}_2, \ldots, \boldsymbol{r}_\kappa\}$, is used as input data, where κ is the number of coordinates. At each coordinate,

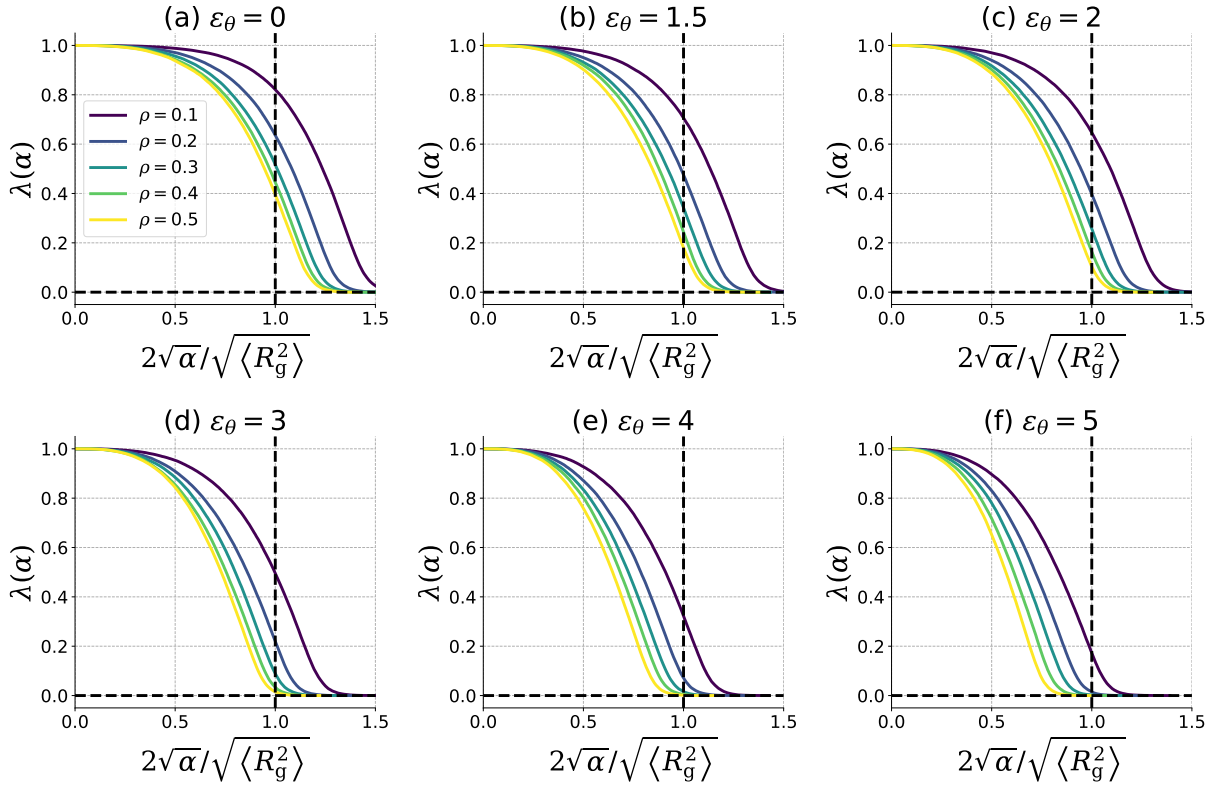

Figure 5.1: Density ρ dependence of $\lambda(\alpha)$ as a function of $2\sqrt{\alpha}/\sqrt{\langle R_g^2 \rangle}$ by varying the bending energy $\varepsilon_\theta = 0$ (a), $\varepsilon_\theta = 1.5$ (b), $\varepsilon_\theta = 2$ (c), $\varepsilon_\theta = 3$ (d), $\varepsilon_\theta = 4$ (e), and $\varepsilon_\theta = 5$ (f). The horizontal and vertical dashed lines represent $\lambda = 0$ and $\alpha = \langle R_g^2 \rangle / 2$, respectively.

assign a virtual sphere with radius $\sqrt{\alpha}$, where α is a parameter. Initially, when $\alpha = 0$, all points are treated as disconnected components. As α increases, the spheres begin to overlap, and connected components form, creating edges and facets. During this process, the topological features varies discontinuously with respect to α, *i.e.*, the loops will appear and disappear. We record the radii for appearance and disappearance as b (birth) and d (death) respectively for each hole, and introduce persistence diagram (PD) as a collection (b, d) of all holes. In this context, a zero-dimensional hole represents a connected component, while a one-dimensional hole represents a loop. PD captures not only the topological features at a specific radius, *i.e.*, a threshold of connection, but also how these features change as the threshold increases. All analysis were performed using the HomCloud [205].

5.3 Results and Discussion

The first analysis aims to reveal the connectivity of the COM coordinates of ring polymer chains using PH. The number of connected components at a given α, denoted as $\beta_0(\alpha)$ and referred to as the zero-th Betti number, is calculated. As the radius of the virtual sphere with a radius of $\sqrt{\alpha}$ expands, spheres will connect each other and finally become one lump. Thus, $\beta_0(\alpha)$ converges to unity as α approaches infinity. We define the function representing the decrease in $\beta_0(\alpha)$ as

$$\lambda(\alpha) = \left\langle \frac{\beta_0(\alpha) - 1}{\beta_0(0) - 1} \right\rangle, \tag{5.4}$$

where $\langle \cdots \rangle$ represents the statistical average over the snapshot configurations generated by MD simulations; note that $\beta_0(\alpha)$ can be determined for each snapshot. Accordingly, this function takes the value $\lambda(\alpha = 0) = 1$ and $\lambda(\alpha \to \infty) = 0$. The density ρ dependence of $\lambda(\alpha)$ is plotted in Fig. 5.1 by varying the bending energy ε_θ. In the plot, the horizontal axis is represented by $2\sqrt{\alpha}/\sqrt{\left\langle R_g^2 \right\rangle}$ with the mean square gyration of radius $\left\langle R_g^2 \right\rangle$ of the ring chains. Note that the COM distance between any pair of two ring polymers, i and j, is related as $r_{ij} = 2\sqrt{\alpha}$ when the rings are in contact, since the radius of the sphere in the PH analysis is $\sqrt{\alpha}$.

Figure 5.1 demonstrates that $\lambda(\alpha)$ decreases and converges to zero at a specific length scale α. This behavior indicates percolation, where clusters are formed by virtually connected COMs. The characteristic length scale is $\alpha = \left\langle R_g^2 \right\rangle / 2$, where a virtual bond is considered to have formed if the distance r_{ij} between the COMs of ring polymer pair (i, j) satisfies $r_{ij} \leq \left\langle R_g^2 \right\rangle$ (see horizontal lines in Fig. 5.1). For flexible ring chains with $\varepsilon_\theta = 0$, λ takes finite values for $\alpha \leq \left\langle R_g^2 \right\rangle$ across all densities, indicating the presence of numerous small clusters. In contrast, stiff ring chains with $\varepsilon_\theta = 5$ exhibit $\lambda \approx 0$ at $\alpha = \left\langle R_g^2 \right\rangle / 2$, suggesting the formation of percolated networks among COMs of ring chains. Furthermore, the length scale of α exhibiting a plateau of $\lambda \approx 1$ approximately corresponds to the characteristic core length, analogous to the behavior of ring polymers modeled as soft macromolecules. As ε_θ increases, this core length is reduced, as shown in Fig. 5.1. These

findings indicate that in flexible ring chains, the cores are large and overlap each other, but their COMs are not connected with one another. In contrast, for stiff ring chains, the smaller cores and relatively larger radius of gyration lead to an increase in the number of virtual bonds between. Thus, the degree of density and chain stiffness strongly influence the structural and dynamic behavior of ring polymer systems.

For flexible ring polymers with the chain stiffness $\varepsilon_\theta = 0$ in semidilute solutions, molecular dynamics (MD) simulations using the Kremer–Grest (KG) model reveal that the mean square radius of gyration $\left\langle R_g^2 \right\rangle$ as a function of density ρ follows the scaling behavior of $\left\langle R_g^2 \right\rangle \sim \rho^{-0.59}$ [29]. More specifically, using the mean square radius of gyration in the dilute limit, denoted as $\left\langle R_g^{\circ 2} \right\rangle$, and the overlap density $3N/(4\pi\langle R_g^{\circ 2}\rangle^{3/2})$, the scaling relation

$$\frac{\langle R_g^2 \rangle}{\langle R_g^{\circ 2} \rangle} = \left[1 + a \left(\frac{\rho}{\rho^*} \right) \right]^b , \tag{5.5}$$

was proposed. Here, $a = 0.45$ and $b = -0.59$ were the fitting parameters.

Figure 5.2 shows the chain stiffness ε_θ dependence of the relationship between $\langle R_g^2 \rangle / \langle R_g^{\circ 2} \rangle$ and ρ/ρ^* from our MD simulations. Note that $\left\langle R_g^{\circ 2} \right\rangle$ was calculated at $\rho = 0.001$. The results reveal that $\left\langle R_g^2 \right\rangle$ decreases with increasing density ρ and exhibits significant deviation from the scaling of Eq. (5.5) when chain stiffness ε_θ is large, particularly noticeable for $\rho/\rho^* > 1$.This deviation from Eq. (5.5) implies that the influence of density ρ on chain conformation varies depending on the chain stiffness ε_θ.

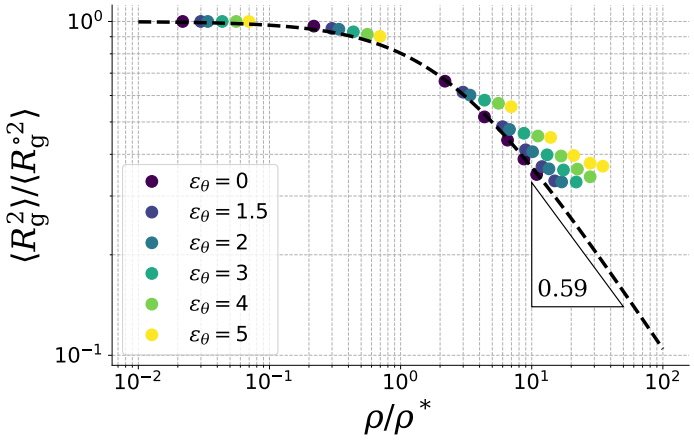

Figure 5.2: density ρ scaled by the overlap density ρ^* dependence of mean square radius of gyration $\left\langle R_g^2 \right\rangle$ scaled by its dilute limit value $\left\langle R_g^{\circ 2} \right\rangle$.

We calculated the radial distribution function, $g(r)$, for center of mass (COM) of ring chains. The results are illustrated in Fig. 5.3. As demonstrated in Fig. 4.3, $g(r)$ exhibits finite values at the length scale $r < \sqrt{\left\langle R_g^2 \right\rangle}$, indicating significant interpenetration between the ring chains. For flexible ring polymers with $\varepsilon_\theta = 0$, $g(r)$ broadens with increasing density ρ, suggesting that the chains become less spatially separated from one another. In addition, for stiff ring polymers with $\varepsilon_\theta = 5$, the degree of interpenetration becomes more pronounced as the density ρ increases. This observation is attributed to the larger mean square radius of gyration, $\left\langle R_g^2 \right\rangle$, compared to that of flexible ring chains with $\varepsilon_\theta = 0$ at the same ρ for dense systems (see Fig. 5.2). An analogous observation with respect to the chain stiffness and density dependence of $g(r)$ for ring polymers was reported in a previous study [13].

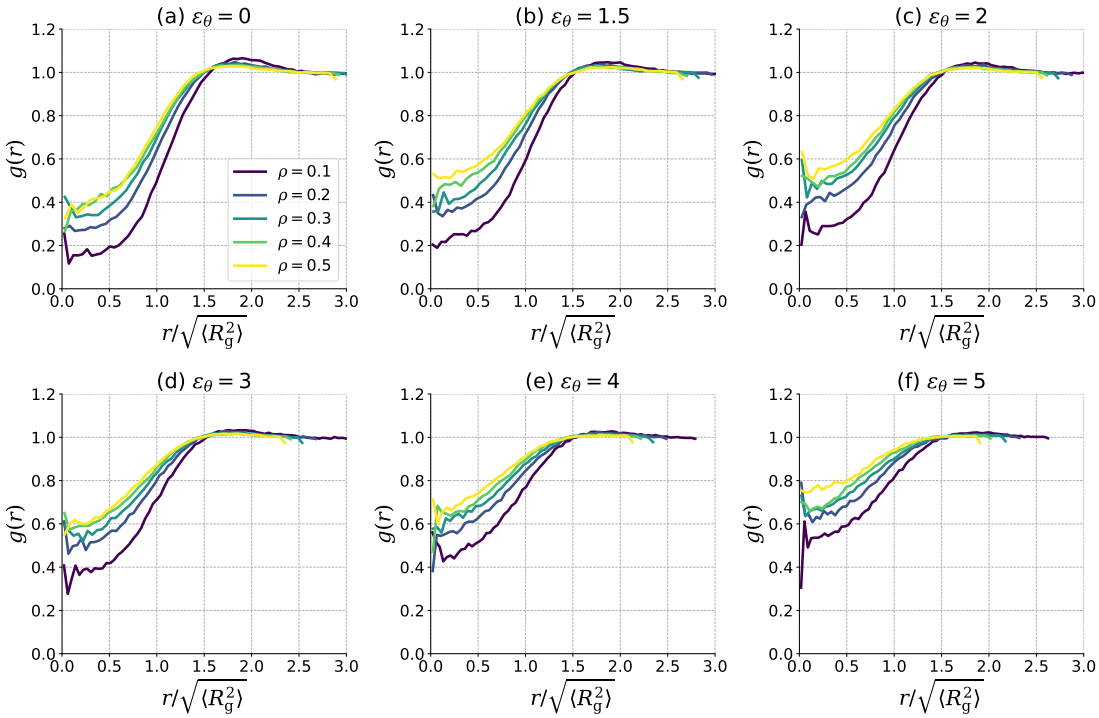

Figure 5.3: Radial distribution function $g(r)$ for COM of ring polymers as a function of the scaled distance $r/\sqrt{\left\langle R_g^2 \right\rangle}$ at $\varepsilon_\theta = 0$ (a), $\varepsilon_\theta = 1.5$ (b), $\varepsilon_\theta = 2$ (c), $\varepsilon_\theta = 3$ (d), $\varepsilon_\theta = 4$ (e), and $\varepsilon_\theta = 5$ (f).

As shown in Figs. 5.2 and 5.3, the influence of density ρ on $\left\langle R_g^2 \right\rangle$ and $g(r)$ significantly varies with chain stiffness ε_θ. To characterized the connectivity between COMs by varying ρ and ε_θ, we introduced a virtual bond between ring polymers i and j. Specifically, if the distance between the COMs of polymers i and j, denoted as r_{ij}, satisfies

$$r_{ij} \leq \sqrt{\langle R_g^2 \rangle}, \tag{5.6}$$

the two polymer chains are considered to be virtually bonded [204]. The number of virtual bond is denoted as Z_b. The average number of virtual bonds can be expressed by

$$\langle Z_b \rangle = \int_0^{\sqrt{\langle R_g^2 \rangle}} 4\pi r^2 \left(\frac{\rho}{N}\right) g(r) \mathrm{d}r. \tag{5.7}$$

Note that the threshold of the virtual bond is less than the contact distance, $2\sqrt{\langle R_g^2 \rangle}$, to emphasize the overlapping between COMs.

Figure 5.4 shows $\langle Z_b \rangle$ as a function of density ρ by varying the chain stiffness ε_θ. The $\langle Z_b \rangle$ is an increasing function of ρ. As ε_θ increases, the slope becomes steeper, indicating a greater dependence on ρ. In contrast, for flexible ring chains with $\varepsilon_\theta = 0$, $g(r/\sqrt{\langle R_g^2 \rangle})$ was found to saturate with increasing ρ, as demonstrated in the previous study [29]. Similarly, $\langle Z_b \rangle$ is also expected to approach saturation towards a finite value. This distinction in the density ρ dependence on the average number of virtual bonds $\langle Z_b \rangle$ implies a significant difference in intermolecular interaction between ring polymers as the chain stiffness ε_θ varies.

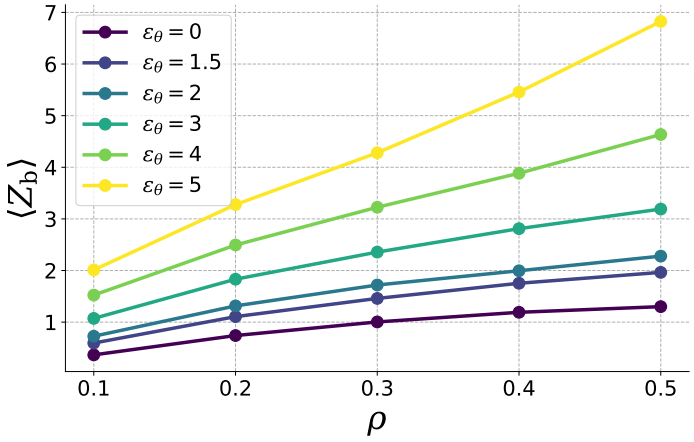

Figure 5.4: Density ρ dependence of the average number of virtual bonds, $\langle Z_b \rangle$ by varying the chain stiffness ε_θ.

The next analysis focuses on the one-dimensional hole, *i.e.* "loop" structure, characterized by PH. Specifically, PH is performed on each individual ring polymer i by using the monomer coordinates as input, which generates a persistent diagram (PD) denoted as PD(i). This analysis reveals the birth and death of topological features such as loops within the structure of the polymer. Furthermore, the "life" of the loop is defined as the vertical distance from the diagonal line in the PD, denoted as $l = d - b$, which quantifies how long during the increase of α the loop persists before disappearing. Thus, larger values of l indicates longer-lived loops, reflecting more stable topologi-

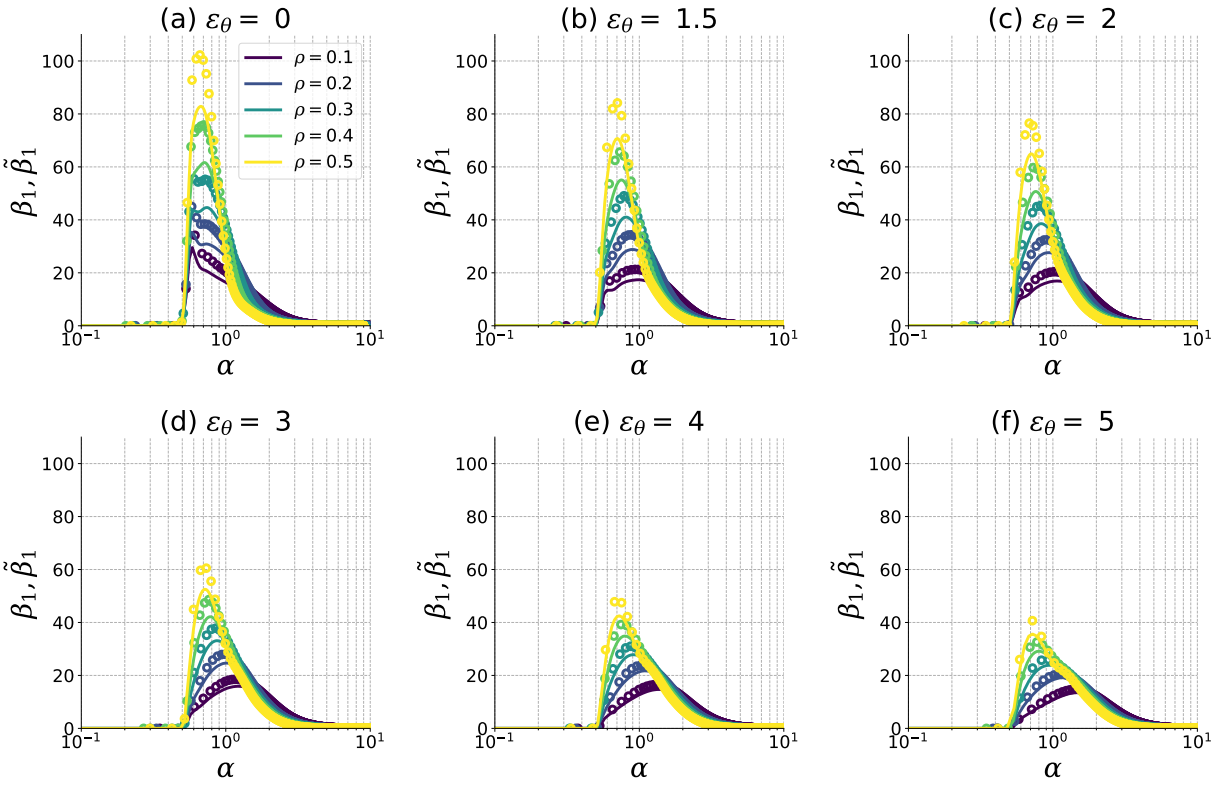

Figure 5.5: Density ρ dependence of $\beta_1(\alpha)$ (points) and $\tilde{\beta}_1(\alpha)$ (solid curves) by varying the bending energy $\varepsilon_\theta = 0$ (a), $\varepsilon_\theta = 1.5$ (b), $\varepsilon_\theta = 2$ (c), $\varepsilon_\theta = 3$ (d), $\varepsilon_\theta = 4$ (e), and $\varepsilon_\theta = 5$ (f).

cal features of the system against the change of threshold. Next, we performed PH for (i, j) pairs of ring polymer chains using the set of their coordinates as input, generating PD denoted as PD$(i \cup j)$. Since threading occurs when the loop of one ring polymer disappears due to penetration by another polymer, PD$(j \to i)$ = PD$(i)\backslash$PD$(i \cup j)$ allows us to quantify the loops being threaded [66]. Here, the set difference operator $\backslash$ represents the subtraction of topological features that vanish when polymer j interacts with polymer i. In this context, polymer i is considered "passive" while polymer j is the "active" participant in the threading process. Thus, this approach quantifies the threading structures between pairs of ring polymers. The probability density distributions of PD(i), PD$(i \cup j)$, and PD$(j \to i)$ with $\varepsilon_\theta = 1.5$ and 5 at densities $\rho = 0.1$ and 0.5 are shown in Fig. B1, B2, B3, and B4 in B.

To analyze the threading structure by varying the density ρ and chain stiffness ε_θ, we quantify

the first Betti number, $\beta_1^{(i)}(\alpha)$, in the PD(i). This is defined by

$$\beta_1^{(i)}(\alpha) = \int_\alpha^\infty \mathrm{d}d \int_0^\infty \mathrm{d}b \sum_k \delta(b - b_k^{(i)})\delta(d - d_k^{(i)}), \tag{5.8}$$

where k refers to the k-th loop on the ring chain i. This $\beta_1(\alpha)$ quantifies the number of loops in the region where $b < \alpha$ and $d > \alpha$, quantifying the number of loops observed at a given α. The average of $\beta_1^{(i)}(\alpha)$ over all ring chains can be expressed as

$$\beta_1(\alpha) = \left\langle \frac{1}{N} \sum_i \beta_1^{(i)}(\alpha) \right\rangle. \tag{5.9}$$

The same calculation can be performed for PD($j \to i$), and the average over all pairs of ring chains (i, j) are denoted as $\tilde{\beta}_1(\alpha)$. This $\tilde{\beta}_1(\alpha)$ measures the number of loops that are being threaded between by other ring chains. Consequently, it is assured that $\beta_1(\alpha) \geq \tilde{\beta}_1(\alpha)$. Furthermore, $\beta_1(\alpha)$ and $\tilde{\beta}_1(\alpha)$ converges asymptotically to zero with respect to each other as α becomes sufficiently large.

Figure 5.5 shows $\beta_1(\alpha)$ and $\tilde{\beta}_1(\alpha)$ for varying ρ and ε_θ. The stiff ring exhibits a broader peak at larger length scales α compared to that of the flexible ring, indicating the presence of large loops. As the density increases, this peak sharpens, with its position shifting to smaller α, signifying the formation of smaller loops. However, the discrepancy in $\beta_1(\alpha)$ and $\tilde{\beta}_1(\alpha)$ between flexible and stiff rings becomes more pronounced with increasing density ρ. This observation aligns with the fact that the density ρ dependence of the mean square radius of gyration $\left\langle R_\mathrm{g}^2 \right\rangle$ exceeds the expected scaling behavior of $\left\langle R_\mathrm{g}^2 \right\rangle \sim \rho^{-0.59}$ for stiff rings as ρ increases (see Fig. S1 in Supporting Information). Finally, for sufficiently large α, the convergence of $\beta_1 \sim \tilde{\beta}_1$ indicates that all large loops are involved in threading.

We further examine the active threading number N_a, which represents the number of rings penetrated by a given ring, and the passive threading number N_p, which denotes the number of

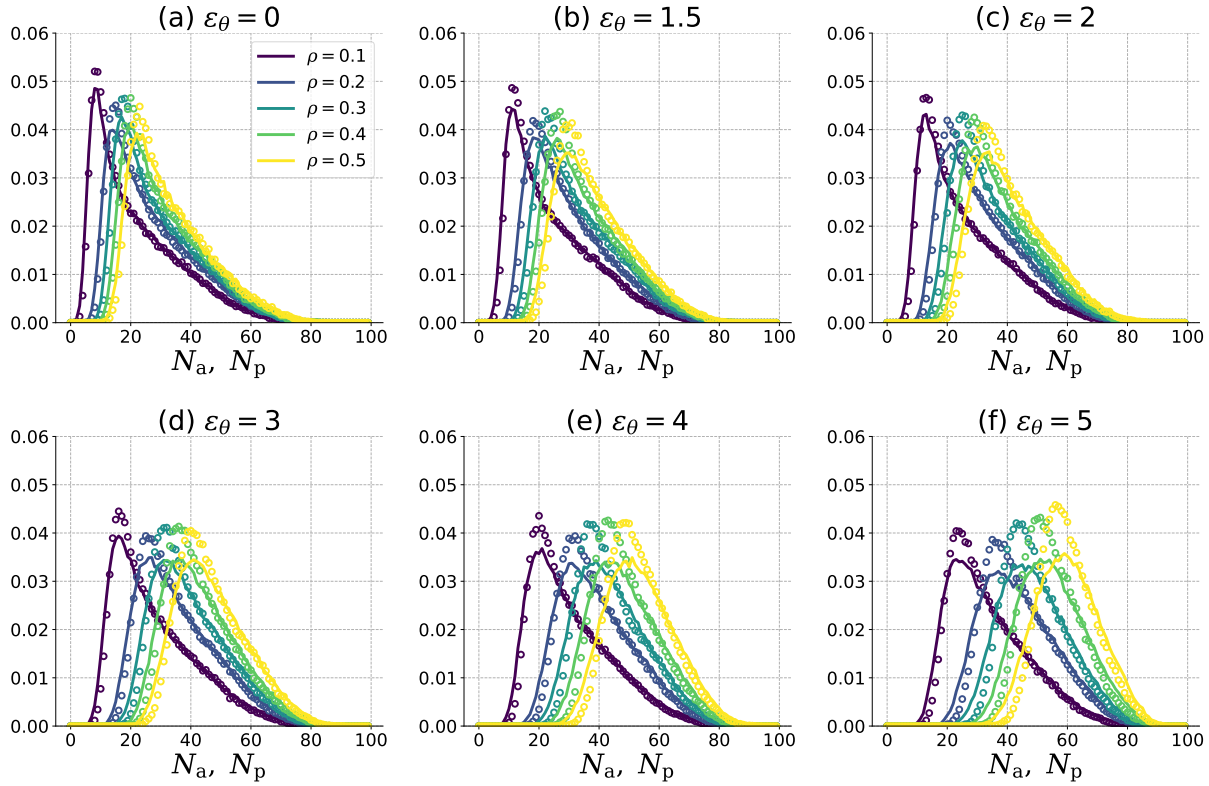

Figure 5.6: Density ρ dependence of probability density distribution of active threading number N_a (points) and passive threading number N_p (solid curves) by varying the bending energy $\varepsilon_\theta = 0$ (a), $\varepsilon_\theta = 1.5$ (b), $\varepsilon_\theta = 2$ (c), $\varepsilon_\theta = 3$ (d), $\varepsilon_\theta = 4$ (e), and $\varepsilon_\theta = 5$ (f). The threshold value is fixed at $l_\mathrm{th} = 0$.

rings that experience penetration by that same ring. For the pair (i, j), we define

$$I_{j\to i}^{(k)} = \begin{cases} 1 & \text{if } l_k \geq l_\mathrm{th} \\ 0 & \text{if } l_k < l_\mathrm{th} \end{cases} \tag{5.10}$$

where l_k represents the life of the k-th loop in PD($j \to i$), and l_th is a threshold value for the life used to characterize the length scale of threading. By summing over loop k and polymer j (i), the active (passive) threading number, $N_{\mathrm{a},j}$ ($N_{\mathrm{p},j}$) for polymer j (i) are obtained, expressed as follows:

$$N_{\mathrm{a},j} = \sum_i \sum_k I_{j\to i}^{(k)}, \quad N_{\mathrm{p},i} = \sum_j \sum_k I_{j\to i}^{(k)}. \tag{5.11}$$

Furthermore, the averages over all ring chains are denoted by N_a and N_p, respectively. Their sta-

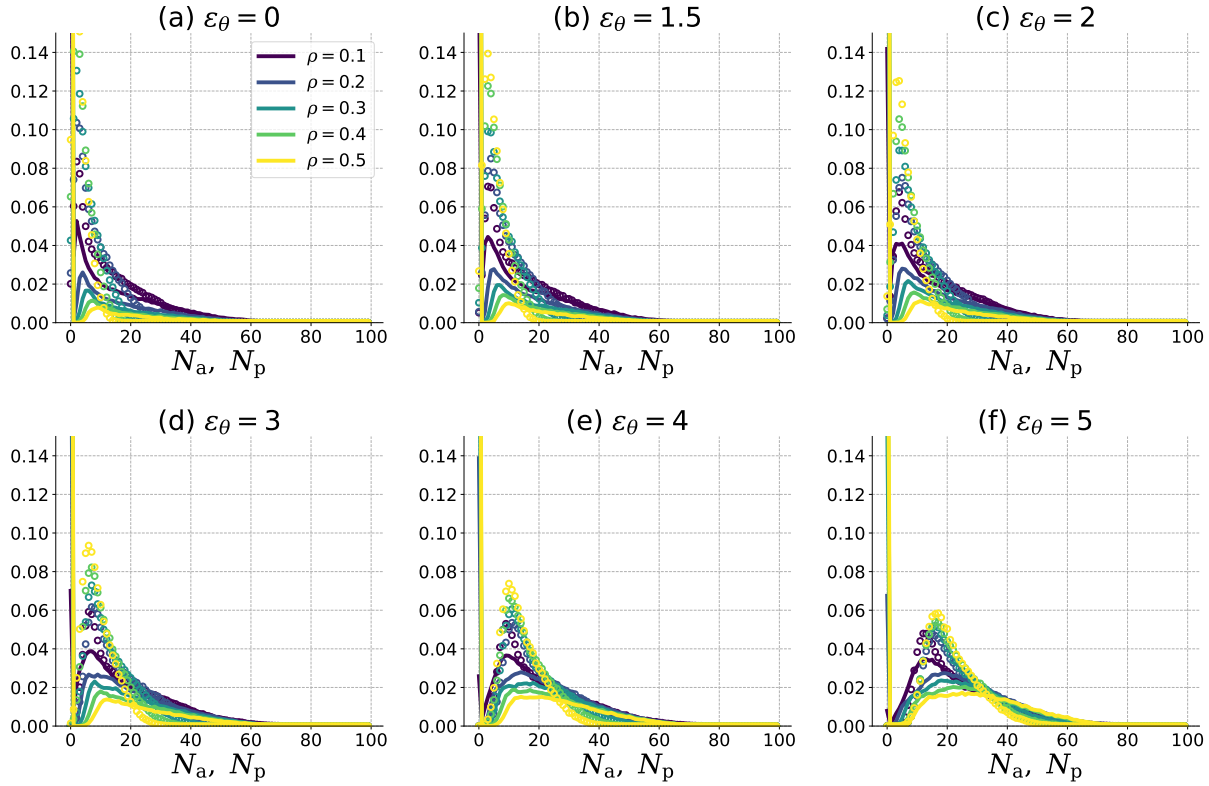

Figure 5.7: Density ρ dependence of probability density distribution of active threading number N_a (points) and passive threading number N_p (solid curves) by varying the bending energy $\varepsilon_\theta = 0$ (a), $\varepsilon_\theta = 1.5$ (b), $\varepsilon_\theta = 2$ (c), $\varepsilon_\theta = 3$ (d), $\varepsilon_\theta = 4$ (e), and $\varepsilon_\theta = 5$ (f). The threshold value is fixed at $l_{th} = 9$.

tistical averages over all chains ensure $\langle N_a \rangle = \langle N_p \rangle$ because, when threading occurs, active and passive threading are always counted once, respectively.

Figure 5.6 presents the probability density distribution of N_a and N_p, respectively. Note that N_a and N_p were calculated by including threading at all length scales, with the threshold l_{th} set to zero. It is demonstrated that for both N_a and N_p, the peak shifts to higher values with increasing chain stiffness ε_θ and density ρ, indicating a greater occurrence of threading. Notably, the density dependence of the distribution becomes more pronounced for stiff rings compared to that of flexible rings. In addition, N_p exhibits a slightly broader distribution than N_a at high density for stiff rings. This asymmetric property between N_a and N_p was found to be pronounced for longer stiff rings, suggesting that the passive threading is significantly influenced by the presence of long-lived loops. In other words, larger loops are likely to be involved in the passive threading.

We further characterize the long-lived active and passive threading structures by introducing the threshold value l_{th}, which has a dimension is σ^2. Since points near the diagonal line are considered noisy, we introduce l_{th} to filter out threading associated with loops of short life, thereby characterizing loops that are mostly correlated with topological constraints. While the results for varying l_{th} are not displayed, the threshold value $l_{\mathrm{th}} = 9$ was determined to capture the most relevant characteristics, and the corresponding results are shown below.

Figure 5.7 illustrates the density dependence of probability density distribution of active and passive threading numbers, N_{a} and N_{b}, at $l_{\mathrm{th}} = 9$. For flexible ring chains, both N_{a} and N_{p} show the tendency of the decrease toward zero as the density ρ increases. This trend is expected to become more pronounced as the threshold value l_{th} increases. This observation suggests that the number of loops necessary for threading becomes minimal in higher densities, consistent with the overlapping structures between the crumbled globules characteristic of flexible ring chains. In contrast, for stiff ring chains, the distribution of N_{a} exhibit a peak at $N_{\mathrm{a}} \approx 20$ across all densities, whereas the distribution of N_{p} shows two distinct peaks, one at $N_{\mathrm{p}} = 0$ and another at $N_{\mathrm{p}} \approx 20$. In addition, the latter peak broadens as the density ρ increases. This observation implies that, when focusing on passive threading of stiff ring chains, they can be categorized into two different types: those having large loops facilitate threading and those lacking such structures. The latter rings are regarded as exhibiting more compact characteristic rather than those of the former.

5.4 Conclusion

In summary, we employed PH analysis to characterize threading from MD simulations of the KG model for ring polymers. Specifically, we focused on the threading structure as influenced by the density ρ and chain stiffness ε_θ, while maintaining the chain length of $N = 400$. Our analyses consists of three components: First, we examined the zero-th Betti number $\beta_0(\alpha)$ to quantify the number of connected components formed by COMs of the polymers. This analysis demonstrates that numerous small clusters of COMs persist for flexible ring chains even at high densities, whereas

a percolated network of COMs develops for stiff ring chains as the density increases. Second, we calculated the first Betti numbers, $\beta_1(\alpha)$ and $\tilde{\beta}_1(\alpha)$, from PD($j \to i$) to characterize the threading structure between pairs of ring chains. It is shown that stiff ring chains exhibit large-scale loops that facilitate threading as the density ρ increases. Furthermore, we also computed the active and passive threading numbers, N_{a} and N_{p}. As both ε_θ and ρ increase, their averages become larger, indicating greater generations of threading, accompanied by the asymmetric behavior of the distributions of N_{a} and N_{p}. Finally, we introduced the threshold value l_{th} to emphasize long-lived threading structures in the calculations of N_{a} and N_{p}. This analysis reveals that the distributions of N_{a} and N_{p} converges to zero for flexible ring chains as the density increases. In contract, for stiff ring chains, the distribution of N_{p} bifurcates into two distinct peaks, indicating heterogeneous threading structure characterized by rings with large-scale loops that facilitate threading and those that have compact ring characteristic. This heterogeneous threading structure observed in stiff ring chains serves as the underlying mechanism for topological glasses, which exhibit heterogeneous rearrangement dynamics of COMs analogous to those of glass-forming liquids.

Chapter 6

General Conclusion

We quantitatively investigated the role of chain stiffness on the glassy dynamics both in linear and ring polymers by using MD simulations. The main results are summarized as follows:

In Chapter 2, we have numerically studied elastic heterogeneities and acoustic excitations in linear polymer glasses, with particular attention to the effects of the chain stiffness. Our main finding is that the degree of heterogeneity in the local shear modulus distribution is insensitive to changes in the bending rigidity. According to the heterogeneous elasticity theory, for unchanging elastic heterogeneities, the vibrational and acoustic properties of amorphous materials are controlled only by global elastic moduli. Consistent with this theoretical prediction, we demonstrated that the BP and properties of the transverse acoustic excitations are both simply scaled only by the global shear modulus. The present work therefore clarified remarkably simple material property relationships in polymer glasses. These originate from the invariance of the local elastic heterogeneities over an extremely wide range of bending rigidity values for polymer chains. Our results also provide good demonstrations that verify the heterogeneous elasticity theory [79–82], which is among the central theories used to describe the mechanical and vibrational properties of amorphous materials. We note that effects of polymerization on vibrational properties can be scaled by global elastic moduli [102, 106].

Chapter 3 focused on the chain length dependence of the Rouse relaxation time and non-Gaussianity for characterizing both the segmental and center-of-mass (COM) mobility with or without chain ends. For linear polymers, the deviation from the Rouse model behavior becomes remarkable with increasing the chain length N by showing the scaling $\tau_p \sim (N/p)^{3.4}$, which is con-

sistent with previously reported results. The NGP shows two peaks: the first peak appears on the time scale where the MSD escapes from the segmental ballistic motion, whereas the second peak corresponds to the realization of the diffusive behavior of the MSD. This indicates that the segment dynamics becomes spatially heterogeneous because of the higher mobility of chain ends in the linear polymer chain. For ring polymers, the Rouse-like behavior with the scaling $\tau_p \sim (N/p)^{2.4}$ was observed. Although the peak of NGP was observed at short times similar to that of linear polymers, the non-Gaussianity was found to be strongly suppressed even for a longer time regime. The segmental dynamics in ring polymers without chain ends becomes spatially homogeneous and the mechanism of the chain motion is essentially different from the reptation model for linear polymers. The center-of-mass dynamics in ring polymers also shows the Gaussian behavior, while a very small non-Gaussianity is observed with increasing chain length.

In Chapter 4, we investigated the glassy dynamics of COM rearrangement in ring polymers with varying the chain stiffness ε_θ and the monomer density ρ. NGP in the distribution of the COM displacement, we have found that more stiff ring chains exhibit a peak in the NGP in long time regimes, which increases with the monomer density. This suggests that the dynamics of stiff ring chains are affected by strong inter-molecular interactions and that the motion of the COM is correlated with each other. In contrast, more semi-flexible ring polymers exhibit relatively small non-Gaussianity, indicating that the COM mobility is almost uncorrelated with each other. The difference in non-Gaussianity between the two types of ring polymers suggests that the nature of the inter-molecular interactions changes significantly depending on the degree of chain stiffness. The behavior of the radius of gyration R_g in relation to ρ depends on the stiffness of the ring polymer chains. In the case of more semi-flexible rings, the R_g follows a master curve described by Eq. (4.8). However, this curve does not apply to stiff ring polymer melts. The deviation from the master curve can be explained by the competition between the shrinkage caused by the excluded volume of neighboring polymers and the expansion due to the chain stiffness. Specifically, semi-flexible ring polymers tend to adopt a compact globule conformation due to the excluded volume interaction with their neighbors, while more stiff rings expand due to the long Kuhn length. We

have also analyzed the dynamics of bond-breakage between the COM of rings defined by using averaged radius of gyration, $\langle R_g^2 \rangle^{1/2}$. The network of virtual bonds in stiff rings are percolating, while those in semi-flexible rings are sparsely distributed. Furthermore, the results for the dynamic susceptibility of bond-breakage are consistent with the non-Gaussianity in the displacement distribution, indicating that the DH of bond-breakage is coupled with the non-Gaussianity in diffusion in ring polymer melts.

Chapter 5 showed the chain stiffness ε_θ and density ρ dependence of the threading structures in ring polymer solutions by using the persistent homology (PH). First, we examined the zero-th Betti number $\beta_0(\alpha)$ to quantify the number of connected components formed by COMs of the polymers. This analysis demonstrates that numerous small clusters of COMs persist for flexible ring chains even at high densities, whereas a percolated network of COMs develops for stiff ring chains as the density increases. Second, we calculated the first Betti numbers, $\beta_1(\alpha)$ and $\tilde{\beta}_1(\alpha)$, from PD($j \to i$) to characterize the threading structure between pairs of ring chains. It is shown that stiff ring chains exhibit large-scale loops that facilitate threading as the density ρ increases. Furthermore, we also computed the active and passive threading numbers, N_a and N_p. As both ε_θ and ρ increase, their averages become larger, indicating greater generations of threading, accompanied by the asymmetric behavior of the distributions of N_a and N_p. Finally, we introduced the threshold value l_{th} to emphasize long-lived threading structures in the calculations of N_a and N_p. This analysis reveals that the distributions of N_a and N_p converges to zero for flexible ring chains as the density increases.

Throughout this study, it is unraveled that the glassy dynamics in ring polymers are significantly affected by the threading with large loops. We characterized the dynamic heterogeneity of COM rearrangement in ring polymers by utilizing the bond-breakage analysis. Stiff ring chains show heterogenous dynamics with dense virtual bonds network. In contrast, semi-flexible ring chains exhibit homogeneous dynamics with sparse virtual bonds. These results are attributed to the deviation of the radius of gyration from the master curve for fully flexible ring chains. While flexible ring chains exhibit a compact globule conformations, stiff ring chains expand and form large loops that facilitate threading. The dynamics of threading have not been fully understood yet, while we are

investigating it by using machine learning to predict the displacement from threading connectivity. We are also planning to examine the dynamic elastic modulus to characterize the properties of TG.

References

[1] P. G. de Gennes, Scaling Concepts in Polymer Physics, Cornell University Press, 1979.

[2] M. Doi, S. F. Edwards, The Theory of Polymer Dynamics, International Series of Monographs on Physics, Oxford University Press, 1986.

[3] M. Cates, J. Deutsch, Conjectures on the statistics of ring polymers, J. Phys. France 47 (1986) 2121–2128.

[4] S. P. Obukhov, M. Rubinstein, T. Duke, Dynamics of a Ring Polymer in a Gel, Phys. Rev. Lett. 73 (1994) 1263–1266.

[5] M. Müller, J. P. Wittmer, M. E. Cates, Topological effects in ring polymers: A computer simulation study, Phys. Rev. E 53 (1996) 5063–5074.

[6] M. Müller, J. P. Wittmer, M. E. Cates, Topological effects in ring polymers. II. Influence of persistence length, Phys. Rev. E 61 (2000) 4078–4089.

[7] T. McLeish, Polymers without beginning or end, Science 297 (2002) 2005–2006.

[8] J. Suzuki, A. Takano, T. Deguchi, Y. Matsushita, Dimension of ring polymers in bulk studied by Monte-Carlo simulation and self-consistent theory, J. Chem. Phys. 131 (2009) 144902.

[9] G. Tsolou, N. Stratikis, C. Baig, P. S. Stephanou, V. G. Mavrantzas, Melt Structure and Dynamics of Unentangled Polyethylene Rings: Rouse Theory, Atomistic Molecular Dynamics Simulation, and Comparison with the Linear Analogues, Macromolecules 43 (2010) 10692–10713.

[10] J. D. Halverson, W. B. Lee, G. S. Grest, A. Y. Grosberg, K. Kremer, Molecular dynamics simulation study of nonconcatenated ring polymers in a melt. I. Statics, J. Chem. Phys. 134 (2011) 204904.

[11] J. D. Halverson, W. B. Lee, G. S. Grest, A. Y. Grosberg, K. Kremer, Molecular dynamics simulation study of nonconcatenated ring polymers in a melt. II. Dynamics, J. Chem. Phys. 134 (2011) 204905.

[12] J. D. Halverson, G. S. Grest, A. Y. Grosberg, K. Kremer, Rheology of Ring Polymer Melts: From Linear Contaminants to Ring-Linear Blends, Phys. Rev. Lett. 108 (2012) 038301.

[13] M. Bernabei, P. Bacova, A. J. Moreno, A. Narros, C. N. Likos, Fluids of semiflexible ring polymers: Effective potentials and clustering, Soft Matter 9 (2013) 1287–1300.

[14] R. Pasquino, T. C. Vasilakopoulos, Y. C. Jeong, H. Lee, S. Rogers, G. Sakellariou, J. Allgaier, A. Takano, A. R. Brás, T. Chang, S. Gooßen, W. Pyckhout-Hintzen, A. Wischnewski, N. Hadjichristidis, D. Richter, M. Rubinstein, D. Vlassopoulos, Viscosity of Ring Polymer Melts, ACS Macro Lett. 2 (2013) 874–878.

[15] A. R. Brás, S. Gooßen, M. Krutyeva, A. Radulescu, B. Farago, J. Allgaier, W. Pyckhout-Hintzen, A. Wischnewski, D. Richter, Compact structure and non-Gaussian dynamics of ring polymer melts, Soft Matter 10 (2014) 3649–3655.

[16] M. Z. Slimani, P. Bacova, M. Bernabei, A. Narros, C. N. Likos, A. J. Moreno, Cluster Glasses of Semiflexible Ring Polymers, ACS Macro Lett. 3 (2014) 611–616.

[17] T. Ge, S. Panyukov, M. Rubinstein, Self-Similar Conformations and Dynamics in Entangled Melts and Solutions of Nonconcatenated Ring Polymers, Macromolecules 49 (2016) 708–722.

[18] D. G. Tsalikis, T. Koukoulas, V. G. Mavrantzas, R. Pasquino, D. Vlassopoulos, W. Pyckhout-Hintzen, A. Wischnewski, M. Monkenbusch, D. Richter, Microscopic Structure, Conformation, and Dynamics of Ring and Linear Poly(ethylene oxide) Melts from Detailed Atomistic

Molecular Dynamics Simulations: Dependence on Chain Length and Direct Comparison with Experimental Data, Macromolecules 50 (2017) 2565–2584.

[19] T. Iwamoto, Y. Doi, K. Kinoshita, A. Takano, Y. Takahashi, E. Kim, T.-H. Kim, S.-i. Takata, M. Nagao, Y. Matsushita, Conformations of Ring Polystyrenes in Semidilute Solutions and in Linear Polymer Matrices Studied by SANS, Macromolecules 51 (2018) 6836–6847.

[20] B. Mei, Z. E. Dell, K. S. Schweizer, Microscopic Theory of Long-Time Center-of-Mass Self-Diffusion and Anomalous Transport in Ring Polymer Liquids, Macromolecules 53 (2020) 10431–10445.

[21] S. H. Jeong, S. Cho, E. J. Roh, T. Y. Ha, J. M. Kim, C. Baig, Intrinsic Surface Characteristics and Dynamic Mechanisms of Ring Polymers in Solution and Melt under Shear Flow, Macromolecules 53 (2020) 10051–10060.

[22] M. Kruteva, J. Allgaier, M. Monkenbusch, L. Porcar, D. Richter, Self-Similar Polymer Ring Conformations Based on Elementary Loops: A Direct Observation by SANS, ACS Macro Lett. 9 (2020) 507–511.

[23] B. Mei, Z. E. Dell, K. S. Schweizer, Theory of Transient Localization, Activated Dynamics, and a Macromolecular Glass Transition in Ring Polymer Liquids, ACS Macro Lett. 10 (2021) 1229–1235.

[24] S. Goto, K. Kim, N. Matubayasi, Effects of chain length on Rouse modes and non-Gaussianity in linear and ring polymer melts, J. Chem. Phys. 155 (2021) 124901.

[25] J. Smrek, I. Chubak, C. N. Likos, K. Kremer, Active topological glass, Nat. Commun. 11 (2020) 26.

[26] R. Staňo, C. N. Likos, J. Smrek, To thread or not to thread? Effective potentials and threading interactions between asymmetric ring polymers, Soft Matter 19 (2022) 17–30.

[27] I. Chubak, S. M. Pachong, K. Kremer, C. N. Likos, J. Smrek, Active Topological Glass Confined within a Spherical Cavity, Macromolecules 55 (2022) 956–964.

[28] P. K. Roy, P. Chaudhuri, S. Vemparala, Effect of ring stiffness and ambient pressure on the dynamical slowdown in ring polymers, Soft Matter 18 (2022) 2959–2967.

[29] X. Cai, C. Liang, H. Liu, G. Zhang, Conformation and structure of ring polymers in semidilute solutions: A molecular dynamics simulation study, Polymer 253 (2022) 124953.

[30] M. Q. Tu, O. Davydovich, B. Mei, P. K. Singh, G. S. Grest, K. S. Schweizer, T. C. O'Connor, C. M. Schroeder, Unexpected Slow Relaxation Dynamics in Pure Ring Polymers Arise from Intermolecular Interactions, ACS Polym. Au (2023).

[31] M. Kruteva, J. Allgaier, D. Richter, Topology Matters: Conformation and Microscopic Dynamics of Ring Polymers, Macromolecules (2023) 7203–7229.

[32] B. Mei, G. S. Grest, S. Liu, T. C. O'Connor, K. S. Schweizer, Unified understanding of the impact of semiflexibility, concentration, and molecular weight on macromolecular-scale ring diffusion, Proc. Natl. Acad. Sci. U.S.A. 121 (2024) e2403964121.

[33] J. D. Cloizeaux, Ring polymers in solution : topological effects 42 433.

[34] A. Baumgärtner, Statistics of self-avoiding ring polymers, J. Chem. Phys. 76 (1982) 4275–4280.

[35] J. M. Deutsch, Equilibrium size of large ring molecules, Phys. Rev. E 59 (1999) R2539–R2541.

[36] A. Y. Grosberg, Critical Exponents for Random Knots, Phys. Rev. Lett. 85 (2000) 3858–3861.

[37] A. Dobay, J. Dubochet, K. Millett, P.-E. Sottas, A. Stasiak, Scaling behavior of random knots, Proc. Natl. Acad. Sci. U.S.A. 100 (2003) 5611–5615.

[38] H. Matsuda, A. Yao, H. Tsukahara, T. Deguchi, K. Furuta, T. Inami, Average size of random polygons with fixed knot topology, Phys. Rev. E 68 (2003) 011102.

[39] N. T. Moore, R. C. Lua, A. Y. Grosberg, Topologically driven swelling of a polymer loop, Proc. Natl. Acad. Sci. U.S.A. 101 (2004) 13431–13435.

[40] N. T. Moore, A. Y. Grosberg, Limits of analogy between self-avoidance and topology-driven swelling of polymer loops, Phys. Rev. E 72 (2005) 061803.

[41] A. Takano, Y. Ohta, K. Masuoka, K. Matsubara, T. Nakano, A. Hieno, M. Itakura, K. Takahashi, S. Kinugasa, D. Kawaguchi, Y. Takahashi, Y. Matsushita, Radii of Gyration of Ring-Shaped Polystyrenes with High Purity in Dilute Solutions., Macromolecules 45 (2012) 369–373.

[42] J. Roovers, Dilute-solution properties of ring polystyrenes, J. Polym. Sci.: Polym. Phys. Ed. 23 (1985) 1117–1126.

[43] A. R. Khokhlov, S. K. Nechaev, Polymer chain in an array of obstacles, Journal de Physique Lettres 112 (1981) 156–160.

[44] T. C. Lubensky, J. Isaacson, Statistics of lattice animals and dilute branched polymers, Phys. Rev. A 20 (1979) 2130–2146.

[45] A. Y. Grosberg, Annealed lattice animal model and Flory theory for the melt of non-concatenated rings: towards the physics of crumpling, Soft Matter 10 (2013) 560–565.

[46] A. Rosa, R. Everaers, Ring Polymers in the Melt State: The Physics of Crumpling, Phys. Rev. Lett. 112 (2014) 118302.

[47] A. Grosberg, Y. Rabin, S. Havlin, A. Neer, Crumpled Globule Model of the Three-Dimensional Structure of DNA, Europhys. Lett. 23 (1993) 373–378.

[48] T. Sakaue, Statistics and geometrical picture of ring polymer melts and solutions, Phys. Rev. E 85 (2012) 021806.

[49] S. Y. Reigh, D. Y. Yoon, Concentration Dependence of Ring Polymer Conformations from Monte Carlo Simulations, ACS Macro Lett. 2 (2013) 296–300.

[50] M. Rubinstein, Dynamics of Ring Polymers in the Presence of Fixed Obstacles, Phys. Rev. Lett. 57 (1986) 3023–3026.

[51] T. A. Kavassalis, J. Noolandi, New View of Entanglements in Dense Polymer Systems, Phys. Rev. Lett. 59 (1987) 2674–2677.

[52] T. A. Kavassalis, J. Noolandi, A new theory of entanglements and dynamics in dense polymer systems, Macromolecules 21 (1988) 2869–2879.

[53] T. A. Kavassalis, J. Noolandi, Entanglement scaling in polymer melts and solutions, Macromolecules 22 (1989) 2709–2720.

[54] T. Sakaue, Ring Polymers in Melts and Solutions: Scaling and Crossover, Phys. Rev. Lett. 106 (2011) 167802.

[55] T. Sakaue, Topological free volume and quasi-glassy dynamics in the melt of ring polymers, Soft Matter 14 (2018) 7507–7515.

[56] K. S. Schweizer, J. G. Curro, Integral equation theories of the structure, thermodynamics, and phase transitions of polymer fluids, Adv. Che. Phys. 98 (1997) 1–142.

[57] R. Verberg, I. M. De Schepper, E. G. D. Cohen, Viscosity of colloidal suspensions, Phys. Rev. E 55 (1997) 3143–3158.

[58] E. G. D. Cohen, R. Verberg, I. M. d. Schepper, Viscosity and diffusion in hard-sphere-like colloidal suspensions, Phys. A 251 (1998) 251–265.

[59] E. J. Saltzman, K. S. Schweizer, Transport coefficients in glassy colloidal fluids, J. Chem. Phys. 119 (2003) 1197–1203.

[60] C. B. Roth, Polymer Glasses, 1st Edition, CRC Press, 2016.

[61] C. Kittel, Introduction to Solid State Physics, 8th Edition, John Wiley and Sons, New York, 2004.

[62] J. Smrek, A. Y. Grosberg, Minimal Surfaces on Unconcatenated Polymer Rings in Melt, ACS Macro Lett. 5 (2016) 750–754.

[63] J. Smrek, K. Kremer, A. Rosa, Threading of Unconcatenated Ring Polymers at High Concentrations: Double-Folded vs Time-Equilibrated Structures, ACS Macro Lett. 8 (2019) 155–160.

[64] D. G. Tsalikis, V. G. Mavrantzas, Threading of Ring Poly(ethylene oxide) Molecules by Linear Chains in the Melt, ACS Macro Lett. 3 (2014) 763–766.

[65] D. G. Tsalikis, V. G. Mavrantzas, D. Vlassopoulos, Analysis of Slow Modes in Ring Polymers: Threading of Rings Controls Long-Time Relaxation, ACS Macro Lett. 5 (2016) 755–760.

[66] F. Landuzzi, T. Nakamura, D. Michieletto, T. Sakaue, Persistence homology of entangled rings, Phys. Rev. Research 2 (2020) 033529.

[67] D. Michieletto, D. Marenduzzo, E. Orlandini, M. Turner, Ring Polymers: Threadings, Knot Electrophoresis and Topological Glasses, Polymers 9 (2017) 349.

[68] D. Michieletto, M. S. Turner, A topologically driven glass in ring polymers, Proc. Natl. Acad. Sci. U.S.A. 113 (2016) 5195–5200.

[69] D. Michieletto, N. Nahali, A. Rosa, Glassiness and Heterogeneous Dynamics in Dense Solutions of Ring Polymers, Phys. Rev. Lett. 119 (2017) 197801.

[70] A. Monaco, A. I. Chumakov, G. Monaco, W. A. Crichton, A. Meyer, L. Comez, D. Fioretto, J. Korecki, R. Rüffer, Effect of Densification on the Density of Vibrational States of Glasses, Phys. Rev. Lett. 97 (2006) 135501.

[71] G. Baldi, V. M. Giordano, G. Monaco, B. Ruta, Sound Attenuation at Terahertz Frequencies and the Boson Peak of Vitreous Silica, Phys. Rev. Lett. 104 (2010) 195501.

[72] A. I. Chumakov, G. Monaco, A. Monaco, W. A. Crichton, A. Bosak, R. Rüffer, A. Meyer, F. Kargl, L. Comez, D. Fioretto, H. Giefers, S. Roitsch, G. Wortmann, M. H. Manghnani, A. Hushur, Q. Williams, J. Balogh, K. Parliński, P. Jochym, P. Piekarz, Equivalence of the Boson Peak in Glasses to the Transverse Acoustic van Hove Singularity in Crystals, Phys. Rev. Lett. 106 (2011) 225501.

[73] O. Yamamuro, T. Matsuo, K. Takeda, T. Kanaya, T. Kawaguchi, K. Kaji, Inelastic neutron scattering study of low energy excitations in glassy 1-butene, J. Chem. Phys. 105 (1996) 732–737.

[74] M. A. Ramos, C. Talón, R. J. Jiménez-Riobóo, S. Vieira, Low-temperature specific heat of structural and orientational glasses of simple alcohols, J. Phys.: Condens. Matter 15 (2003) S1007–S1018.

[75] G. Monaco, V. M. Giordano, Breakdown of the Debye approximation for the acoustic modes with nanometric wavelengths in glasses, Proc. Natl. Acad. Sci. U.S.A. 106 (2009) 3659–3663.

[76] T. Shibata, T. Mori, S. Kojima, Low-frequency vibrational properties of crystalline and glassy indomethacin probed by terahertz time-domain spectroscopy and low-frequency Raman scattering, Spectrochim. Acta A 150 (2015) 207–211.

[77] M. Kabeya, T. Mori, Y. Fujii, A. Koreeda, B. W. Lee, J.-H. Ko, S. Kojima, Boson peak dynamics of glassy glucose studied by integrated terahertz-band spectroscopy, Phys. Rev. B 94 (2016) 224204.

[78] T. Mori, Y. Jiang, Y. Fujii, S. Kitani, H. Mizuno, A. Koreeda, L. Motoji, H. Tokoro, K. Shiraki, Y. Yamamoto, S. Kojima, Detection of boson peak and fractal dynamics of disordered systems using terahertz spectroscopy, Phys. Rev. E 102 (2020) 022502.

[79] W. Schirmacher, Thermal conductivity of glassy materials and the “boson peak”, EPL 73 (2006) 892–898.

[80] W. Schirmacher, G. Ruocco, T. Scopigno, Acoustic Attenuation in Glasses and its Relation with the Boson Peak, Phys. Rev. Lett. 98 (2007) 025501.

[81] S. Köhler, G. Ruocco, W. Schirmacher, Coherent potential approximation for diffusion and wave propagation in topologically disordered systems, Phys. Rev. B 88 (2013) 064203.

[82] W. Schirmacher, T. Scopigno, G. Ruocco, Theory of vibrational anomalies in glasses, J. Non-Cryst. Solids 407 (2015) 133–140.

[83] M. Wyart, Scaling of phononic transport with connectivity in amorphous solids, EPL 89 (2010) 64001.

[84] E. DeGiuli, A. Laversanne-Finot, G. Düring, E. Lerner, M. Wyart, Effects of coordination and pressure on sound attenuation, boson peak and elasticity in amorphous solids, Soft Matter 10 (2014) 5628–5644.

[85] M. Shimada, H. Mizuno, A. Ikeda, Vibrational spectrum derived from local mechanical response in disordered solids, Soft Matter 16 (2020) 7279–7288.

[86] M. Shimada, H. Mizuno, A. Ikeda, Novel elastic instability of amorphous solids in finite spatial dimensions, Soft Matter 17 (2021) 346–364. doi:10.1039/D0SM01583K.

[87] M. Shimada, E. De Giuli, Random quench predicts universal properties of amorphous solids, arXiv (2020). arXiv:2008.11896.

[88] M. Tsamados, A. Tanguy, C. Goldenberg, J.-L. Barrat, Local elasticity map and plasticity in a model Lennard-Jones glass, Phys. Rev. E 80 (2009) 026112.

[89] A. Makke, M. Perez, J. Rottler, O. Lame, J.-L. Barrat, Predictors of Cavitation in Glassy Polymers under Tensile Strain: A Coarse-Grained Molecular Dynamics Investigation, Macromol. Theory Simul. 20 (2011) 826–836.

[90] H. Mizuno, S. Mossa, J.-L. Barrat, Measuring spatial distribution of the local elastic modulus in glasses, Phys. Rev. E 87 (2013) 042306.

[91] H. Wagner, D. Bedorf, S. Küchemann, M. Schwabe, B. Zhang, W. Arnold, K. Samwer, Local elastic properties of a metallic glass, Nat. Mater. 10 (2011) 439–442.

[92] T. C. Hufnagel, Cryogenic rejuvenation, Nat. Mater. 14 (2015) 867–868.

[93] A. Marruzzo, W. Schirmacher, A. Fratalocchi, G. Ruocco, Heterogeneous shear elasticity of glasses: the origin of the boson peak, Sci. Rep. 3 (2013) 2316.

[94] A. Marruzzo, S. Köhler, A. Fratalocchi, G. Ruocco, W. Schirmacher, Vibrational anomalies and marginal stability of glasses, Eur. Phys. J. Special Topics 216 (2013) 83–93.

[95] H. Mizuno, S. Mossa, J.-L. Barrat, Elastic heterogeneity, vibrational states, and thermal conductivity across an amorphisation transition, EPL 104 (2013) 56001.

[96] H. Mizuno, S. Mossa, J.-L. Barrat, Acoustic excitations and elastic heterogeneities in disordered solids, Proc. Natl. Acad. Sci. U.S.A. 111 (2014) 11949–11954.

[97] H. Mizuno, S. Mossa, J.-L. Barrat, Relation of vibrational excitations and thermal conductivity to elastic heterogeneities in disordered solids, Phys. Rev. B 94 (2016) 144303.

[98] A. Shakerpoor, E. Flenner, G. Szamel, Stability dependence of local structural heterogeneities of stable amorphous solids, Soft Matter 16 (2020) 914–920.

[99] G. Kapteijns, D. Richard, E. Bouchbinder, E. Lerner, Elastic moduli fluctuations predict wave attenuation rates in glasses, arXiv (2020). arXiv:2008.08337.

[100] K. Niss, B. Begen, B. Frick, J. Ollivier, A. Beraud, A. Sokolov, V. N. Novikov, C. Alba-Simionesco, Influence of Pressure on the Boson Peak: Stronger than Elastic Medium Transformation, Phys. Rev. Lett. 99 (2007) 055502.

[101] L. Hong, B. Begen, A. Kisliuk, C. Alba-Simionesco, V. N. Novikov, A. P. Sokolov, Pressure and density dependence of the boson peak in polymers, Phys. Rev. B 78 (2008) 134201.

[102] S. Caponi, S. Corezzi, D. Fioretto, A. Fontana, G. Monaco, F. Rossi, Effect of polymerization on the boson peak, from liquid to glass, J. Non-Cryst. Solids 357 (2011) 530–533.

[103] T. Pérez-Castañeda, R. J. Jiménez-Riobóo, M. A. Ramos, Two-Level Systems and Boson Peak Remain Stable in 110-Million-Year-Old Amber Glass, Phys. Rev. Lett. 112 (2014) 165901.

[104] W. Terao, T. Mori, Y. Fujii, A. Koreeda, M. Kabeya, S. Kojima, Boson peak dynamics of natural polymer starch investigated by terahertz time-domain spectroscopy and low-frequency Raman scattering, Spectrochim. Acta A 192 (2018) 446–450.

[105] R. Zorn, H. Yin, W. Lohstroh, W. Harrison, P. M. Budd, B. R. Pauw, M. Böhning, A. Schönhals, Anomalies in the low frequency vibrational density of states for a polymer with intrinsic microporosity – the Boson peak of PIM-1, Phys. Chem. Chem. Phys. 20 (2018) 1355–1363.

[106] S. Corezzi, L. Comez, Scaling behavior of the Raman intensity and heterogeneous elasticity during the chemical vitrification of an epoxy resin, Atti della Accademia Peloritana dei Pericolanti - Classe di Scienze Fisiche, Matematiche e Naturali 98 (2020) 7.

[107] T. S. Jain, J. J. de Pablo, Influence of confinement on the vibrational density of states and the Boson peak in a polymer glass, J. Chem. Phys. 120 (2004) 9371–9375.

[108] B. Schnell, H. Meyer, C. Fond, J. P. Wittmer, J. Baschnagel, Simulated glass-forming polymer melts: Glass transition temperature and elastic constants of the glassy state, Eur. Phys. J. E 34 (2011) 97.

[109] A. Lappala, A. Zaccone, E. M. Terentjev, Polymer glass transition occurs at the marginal rigidity point with connectivity z * = 4 , Soft Matter 12 (2016) 7330–7337.

[110] C. Ness, V. V. Palyulin, R. Milkus, R. Elder, T. Sirk, A. Zaccone, Nonmonotonic dependence of polymer-glass mechanical response on chain bending stiffness, Phys. Rev. E 96 (2017) 030501.

[111] R. Milkus, C. Ness, V. V. Palyulin, J. Weber, A. Lapkin, A. Zaccone, Interpretation of the Vibrational Spectra of Glassy Polymers Using Coarse-Grained Simulations, Macromolecules 51 (2018) 1559–1572.

[112] A. Giuntoli, D. Leporini, Boson Peak Decouples from Elasticity in Glasses with Low Connectivity, Phys. Rev. Lett. 121 (2018) 185502.

[113] N. Tomoshige, H. Mizuno, T. Mori, K. Kim, N. Matubayasi, Boson peak, elasticity, and glass transition temperature in polymer glasses: Effects of the rigidity of chain bending, Sci. Rep. 9 (2019) 19514.

[114] K. Kremer, G. S. Grest, Dynamics of entangled linear polymer melts: A molecular-dynamics simulation, J. Chem. Phys. 92 (1990) 5057–5086.

[115] M. Shimada, H. Mizuno, A. Ikeda, Anomalous vibrational properties in the continuum limit of glasses, Phys. Rev. E 97 (2018) 022609.

[116] S. Plimpton, Fast parallel algorithms for short-range molecular dynamics, J. Comput. Phys. 117 (1995) 1–19.

[117] G. Monaco, S. Mossa, Anomalous properties of the acoustic excitations in glasses on the mesoscopic length scale, Proc. Natl. Acad. Sci. U.S.A. 106 (2009) 16907–16912.

[118] Y. M. Beltukov, C. Fusco, D. A. Parshin, A. Tanguy, Boson peak and Ioffe-Regel criterion in amorphous siliconlike materials: The effect of bond directionality, Phys. Rev. E 93 (2016) 023006.

[119] H. Mizuno, A. Ikeda, Phonon transport and vibrational excitations in amorphous solids, Phys. Rev. E 98 (2018) 062612.

[120] R. A. Riggleman, J. F. Douglas, J. J. de Pablo, Antiplasticization and the elastic properties of glass-forming polymer liquids, Soft Matter 6 (2010).

[121] L. Larini, A. Ottochian, C. De Michele, D. Leporini, Universal scaling between structural relaxation and vibrational dynamics in glass-forming liquids and polymers, Nat. Phys. 4 (2008) 42–45.

[122] H. Shiba, Y. Yamada, T. Kawasaki, K. Kim, Unveiling Dimensionality Dependence of Glassy Dynamics: 2D Infinite Fluctuation Eclipses Inherent Structural Relaxation, Phys. Rev. Lett. 117 (2016) 245701.

[123] J. C. Dyre, Source of non-Arrhenius average relaxation time in glass-forming liquids, J. Non-Cryst. Solids 235-237 (1998) 142–149.

[124] J. C. Dyre, Colloquium: The glass transition and elastic models of glass-forming liquids, Rev. Mod. Phys. 78 (2006) 953–972.

[125] F. Puosi, D. Leporini, Communication: Correlation of the instantaneous and the intermediate-time elasticity with the structural relaxation in glassforming systems, J. Chem. Phys. 136 (2012) 041104.

[126] S. Brown, G. Szamel, Computer simulation study of the structure and dynamics of ring polymers, J. Chem. Phys. 109 (1998) 6184–6192.

[127] S. S. Jang, T. Çağin, W. A. Goddard, III, Effect of cyclic chain architecture on properties of dilute solutions of polyethylene from molecular dynamics simulations, J. Chem. Phys. 119 (2003) 1843–1854.

[128] A. R. Brás, R. Pasquino, T. Koukoulas, G. Tsolou, O. Holderer, A. Radulescu, J. Allgaier, V. G. Mavrantzas, W. Pyckhout-Hintzen, A. Wischnewski, D. Vlassopoulos, D. Richter, Structure and dynamics of polymer rings by neutron scattering: breakdown of the Rouse model, Soft Matter 7 (2011) 11169–11176.

[129] S. Gooßen, A. R. Brás, M. Krutyeva, M. Sharp, P. Falus, A. Feoktystov, U. Gasser, W. Pyckhout-Hintzen, A. Wischnewski, D. Richter, Molecular Scale Dynamics of Large Ring Polymers, Phys. Rev. Lett. 113 (2014) 304.

[130] V. Arrighi, J. S. Higgins, Local Effects of Ring Topology Observed in Polymer Conformation and Dynamics by Neutron Scattering—A Review, Polymers 12 (2020) 1884.

[131] A. Arbe, F. Alvarez, J. Colmenero, Neutron scattering and molecular dynamics simulations: synergetic tools to unravel structure and dynamics in polymers, Soft Matter 8 (2012) 8257–8270.

[132] W. Kob, C. Donati, S. J. Plimpton, P. H. Poole, S. C. Glotzer, Dynamical Heterogeneities in a Supercooled Lennard-Jones Liquid, Phys. Rev. Lett. 79 (1997) 2827–2830.

[133] C. Donati, S. C. Glotzer, P. H. Poole, W. Kob, S. J. Plimpton, Spatial correlations of mobility and immobility in a glass-forming Lennard-Jones liquid, Phys. Rev. E 60 (1999) 3107–3119.

[134] E. J. Saltzman, K. S. Schweizer, Non-Gaussian effects, space-time decoupling, and mobility bifurcation in glassy hard-sphere fluids and suspensions, Phys. Rev. E 74 (2006) 061501.

[135] S. Plimpton, Fast Parallel Algorithms for Short-Range Molecular Dynamics, J. Comput. Phys. 117 (1995) 1–19.

[136] S. K. Sukumaran, G. S. Grest, K. Kremer, R. Everaers, Identifying the primitive path mesh in entangled polymer liquids, J. Polym. Sci. B Polym. Phys. 43 (2005) 917–933.

[137] K. Hagita, T. Murashima, Effect of chain-penetration on ring shape for mixtures of rings and linear polymers, Polymer 218 (2021) 123493.

[138] A. Kopf, B. Dünweg, W. Paul, Dynamics of polymer "isotope" mixtures: Molecular dynamics simulation and Rouse model analysis, J. Chem. Phys. 107 (1997) 6945–6955.

[139] M. J. Wiest, R. S. Burdette, W. T. Liu, R. B. Bird, Effect of ring closure on rheological behavior, J. Non-Newton. Fluid 24 (1987) 279–295.

[140] P. M. Rauscher, K. S. Schweizer, S. J. Rowan, J. J. de Pablo, Dynamics of poly[n]catenane melts, J. Chem. Phys. 152 (2020) 214901.

[141] D. Pan, Z.-Y. Sun, Diffusion and Relaxation Dynamics of Supercooled Polymer Melts, Chin. J. Polym. Sci. 36 (2018) 1187–1194.

[142] M. Aichele, Y. Gebremichael, F. W. Starr, J. Baschnagel, S. C. Glotzer, Polymer-specific effects of bulk relaxation and stringlike correlated motion in the dynamics of a supercooled polymer melt, J. Chem. Phys. 119 (2003) 5290–5304.

[143] S. Peter, H. Meyer, J. Baschnagel, MD simulation of concentrated polymer solutions: Structural relaxation near the glass transition, Eur. Phys. J. E 28 (2009) 147–158.

[144] J.-L. Barrat, J. Baschnagel, A. Lyulin, Molecular dynamics simulations of glassy polymers, Soft Matter 6 (2010) 3430–3446.

[145] J. S. Shaffer, Effects of chain topology on polymer dynamics: Configurational relaxation in polymer melts, J. Chem. Phys. 103 (1995) 761–772.

[146] J. T. Padding, W. J. Briels, Time and length scales of polymer melts studied by coarse-grained molecular dynamics simulations, J. Chem. Phys. 117 (2002) 925–943.

[147] J. T. Kalathi, S. K. Kumar, M. Rubinstein, G. S. Grest, Rouse Mode Analysis of Chain Relaxation in Homopolymer Melts, Macromolecules 47 (2014) 6925–6931.

[148] H.-P. Hsu, K. Kremer, Detailed analysis of Rouse mode and dynamic scattering function of highly entangled polymer melts in equilibrium, Eur. Phys. J. Spec. Top. 226 (2017) 693–703.

[149] Z. Wang, A. E. Likhtman, R. G. Larson, Segmental Dynamics in Entangled Linear Polymer Melts, Macromolecules 45 (2012) 3557–3570.

[150] M. E. Cates, M. Fuchs, K. Kroy, W. C. K. Poon, A. M. Puertas, Theory and simulation of gelation, arrest and yielding in attracting colloids, J. Phys.: Condens. Matter 16 (2004) S4861–S4875.

[151] D. R. Reichman, E. Rabani, P. L. Geissler, Comparison of Dynamical Heterogeneity in Hard-Sphere and Attractive Glass Formers, J. Phys. Chem. B 109 (2005) 14654–14658.

[152] E. Flenner, G. Szamel, Relaxation in a glassy binary mixture: Comparison of the mode-coupling theory to a Brownian dynamics simulation, Phys. Rev. E 72 (2005) 031508.

[153] D. Michieletto, D. Marenduzzo, E. Orlandini, G. P. Alexander, M. S. Turner, Threading Dynamics of Ring Polymers in a Gel, ACS Macro Lett. 3 (2014) 255–259.

[154] D. Michieletto, D. Marenduzzo, E. Orlandini, G. P. Alexander, M. S. Turner, Dynamics of self-threading ring polymers in a gel, Soft Matter 10 (2014) 5936–5944.

[155] E. Lee, S. Kim, Y. Jung, Slowing Down of Ring Polymer Diffusion Caused by Inter-Ring Threading, Macromol. Rapid Commun. 36 (2015) 1115–1121.

[156] D. Michieletto, N. Nahali, A. Rosa, Glassiness and Heterogeneous Dynamics in Dense Solutions of Ring Polymers, Phys. Rev. Lett. 119 (2017) 197801.

[157] T. Sakaue, Topological free volume and quasi-glassy dynamics in the melt of ring polymers, Soft Matter 14 (2018) 7507–7515.

[158] E. Lee, Y. Jung, Slow Dynamics of Ring Polymer Melts by Asymmetric Interaction of Threading Configuration: Monte Carlo Study of a Dynamically Constrained Lattice Model, Polymers 11 (2019) 516.

[159] D. Michieletto, T. Sakaue, Dynamical Entanglement and Cooperative Dynamics in Entangled Solutions of Ring and Linear Polymers, ACS Macro Lett. 10 (2021) 129–134.

[160] J. D. Halverson, J. Smrek, K. Kremer, A. Y. Grosberg, From a melt of rings to chromosome territories: The role of topological constraints in genome folding, Rep. Prog. Phys. 77 (2014) 022601.

[161] J. Kim, J. M. Kim, C. Baig, Intrinsic structure and dynamics of monolayer ring polymer melts, Soft Matter 17 (2021) 10703–10715.

[162] E.-J. Donth, The Glass Transition: Relaxation Dynamics in Liquids and Disordered Materials, Springer Berlin Heidelberg, 2001.

[163] W.-C. Lo, M. S. Turner, The topological glass in ring polymers, EPL 102 (2013) 58005.

[164] L. R. Gómez, N. A. García, T. Pöschel, Packing structure of semiflexible rings, Proc. Natl. Acad. Sci. U.S.A. 117 (2020) 3382–3387.

[165] I. Chubak, C. N. Likos, K. Kremer, J. Smrek, Emergence of active topological glass through directed chain dynamics and nonequilibrium phase segregation, Phys. Rev. Research 2 (2020) 043249.

[166] R. Böhmer, G. Hinze, G. Diezemann, B. Geil, H. Sillescu, Dynamic heterogeneity in supercooled ortho-terphenyl studied by multidimensional deuteron NMR, Europhys. Lett. 36 (1996) 55–60.

[167] R. Richert, M. Richert, Dynamic heterogeneity, spatially distributed stretched-exponential patterns, and transient dispersions in solvation dynamics, Phys. Rev. E 58 (1998) 779–784.

[168] M. D. Ediger, Spatially Heterogeneous Dynamics in Supercooled Liquids, Annu. Rev. Phys. Chem. 51 (2000) 99–128.

[169] M. M. Hurley, P. Harrowell, Kinetic structure of a two-dimensional liquid, Phys. Rev. E 52 (1995) 1694–1698.

[170] R. Yamamoto, A. Onuki, Kinetic Heterogeneities in a Highly Supercooled Liquid, J. Phys. Soc. Jpn. 66 (1997) 2545–2548.

[171] C. Donati, J. F. Douglas, W. Kob, S. J. Plimpton, P. H. Poole, S. C. Glotzer, Stringlike Cooperative Motion in a Supercooled Liquid, Phys. Rev. Lett. 80 (1998) 2338–2341.

[172] M. M. Hurley, P. Harrowell, Non-Gaussian behavior and the dynamical complexity of particle motion in a dense two-dimensional liquid, J. Chem. Phys. 105 (1996) 10521–10526.

[173] M. S. Shell, P. G. Debenedetti, F. H. Stillinger, Dynamic heterogeneity and non-Gaussian behaviour in a model supercooled liquid, J. Phys.: Condens. Matter 17 (2005) S4035–S4046.

[174] P. Chaudhuri, L. Berthier, W. Kob, Universal Nature of Particle Displacements close to Glass and Jamming Transitions, Phys. Rev. Lett. 99 (2007) 060604.

[175] J. D. Halverson, G. S. Grest, A. Y. Grosberg, K. Kremer, Rheology of Ring Polymer Melts: From Linear Contaminants to Ring-Linear Blends, Phys. Rev. Lett. 108 (2012) 038301.

[176] H.-P. Hsu, K. Kremer, Static and dynamic properties of large polymer melts in equilibrium, J. Chem. Phys. 144 (2016) 154907.

[177] D. Parisi, S. Costanzo, Y. Jeong, J. Ahn, T. Chang, D. Vlassopoulos, J. D. Halverson, K. Kremer, T. Ge, M. Rubinstein, G. S. Grest, W. Srinin, A. Y. Grosberg, Nonlinear Shear Rheology of Entangled Polymer Rings, Macromolecules 54 (2021) 2811–2827.

[178] R. Faller, A. Kolb, F. Müller-Plathe, Local chain ordering in amorphous polymer melts: Influence of chain stiffness, Phys. Chem. Chem. Phys. 1 (1999) 2071–2076.

[179] R. Everaers, S. K. Sukumaran, G. S. Grest, C. Svaneborg, A. Sivasubramanian, K. Kremer, Rheology and Microscopic Topology of Entangled Polymeric Liquids, Science 303 (2004) 823–826.

[180] J. Aronovitz, D. Nelson, Universal features of polymer shapes, J. Phys. France 47 (1986) 1445–1456.

[181] J. Rudnick, G. Gaspari, The aspherity of random walks, J. Phys. A: Math. Gen. 19 (1986) L191.

[182] G. Gaspari, J. Rudnick, A. Beldjenna, The shapes of open and closed random walks: A 1/d expansion, J. Phys. A: Math. Gen. 20 (1987) 3393.

[183] O. Jagodzinski, E. Eisenriegler, K. Kremer, Universal shape properties of open and closed polymer chains: Renormalization group analysis and Monte Carlo experiments, J. Phys. I France 2 (1992) 2243–2279.

[184] M. Bishop, J. P. J. Michels, The shape of ring polymers, J. Chem. Phys. 82 (1985) 1059–1061.

[185] M. Bishop, C. J. Saltiel, Polymer shapes in two, four, and five dimensions, J. Chem. Phys. 88 (1988) 3976–3980.

[186] G. Zifferer, W. Preusser, Monte Carlo Simulation Studies of the Size and Shape of Ring Polymers, Macromol. Theory Simul. 10 (2001) 397–407.

[187] K. Alim, E. Frey, Shapes of Semiflexible Polymer Rings, Phys. Rev. Lett. 99 (2007) 198102.

[188] E. J. Rawdon, J. C. Kern, M. Piatek, P. Plunkett, A. Stasiak, K. C. Millett, Effect of Knotting on the Shape of Polymers, Macromolecules 41 (2008) 8281–8287.

[189] D. Michieletto, D. Marenduzzo, E. Orlandini, Is the kinetoplast DNA a percolating network of linked rings at its critical point?, Phys. Biol. 12 (2015) 036001.

[190] R. Yamamoto, A. Onuki, Dynamics of highly supercooled liquids: Heterogeneity, rheology, and diffusion, Phys. Rev. E 58 (1998) 3515–3529.

[191] H. Shiba, T. Kawasaki, A. Onuki, Relationship between bond-breakage correlations and four-point correlations in heterogeneous glassy dynamics: Configuration changes and vibration modes, Phys. Rev. E 86 (2012) 041504.

[192] T. Kawasaki, A. Onuki, Slow relaxations and stringlike jump motions in fragile glass-forming liquids: Breakdown of the Stokes-Einstein relation, Phys. Rev. E 87 (2013) 012312.

[193] H. Shiba, Y. Yamada, T. Kawasaki, K. Kim, Unveiling Dimensionality Dependence of Glassy Dynamics: 2D Infinite Fluctuation Eclipses Inherent Structural Relaxation, Phys. Rev. Lett. 117 (2016) 245701.

[194] Z. E. Dell, K. S. Schweizer, Intermolecular structural correlations in model globular and unconcatenated ring polymer liquids, Soft Matter 14 (2018) 9132–9142.

[195] C. Jeong, J. F. Douglas, Relation between Polymer Conformational Structure and Dynamics in Linear and Ring Polyethylene Blends, Macromol. Theory Simul. 26 (2017) 1700045.

[196] A. Borger, W. Wang, T. C. O'Connor, T. Ge, G. S. Grest, G. V. Jensen, J. Ahn, T. Chang, O. Hassager, K. Mortensen, D. Vlassopoulos, Q. Huang, Threading–Unthreading Transition of Linear-Ring Polymer Blends in Extensional Flow, ACS Macro Lett. 9 (2020) 1452–1457.

[197] T. C. O'Connor, T. Ge, G. S. Grest, Composite entanglement topology and extensional rheology of symmetric ring-linear polymer blends, J. Rheol. 66 (2022) 49–65.

[198] G. S. Grest, T. Ge, S. J. Plimpton, M. Rubinstein, T. C. O'Connor, Entropic Mixing of Ring/Linear Polymer Blends, ACS Polym. Au 3 (2023) 209–216.

[199] A. Y. Grosberg, S. K. Nechaev, E. I. Shakhnovich, The role of topological constraints in the kinetics of collapse of macromolecules, J. Phys. France 49 (1988) 2095–2100.

[200] H. Edelsbrunner, D. Letscher, A. Zomorodian, Topological persistence and simplification, in: Proceedings 41st Annual Symposium on Foundations of Computer Science, 2000, pp. 454–463.

[201] H. Edelsbrunner, J. Harer, Computational Topology: An Introduction, American Mathematical Society, Providence, R.I, 2010.

[202] Y. Hiraoka, T. Nakamura, A. Hirata, E. G. Escolar, K. Matsue, Y. Nishiura, Hierarchical structures of amorphous solids characterized by persistent homology, Proc. Natl. Acad. Sci. U.S.A. 113 (2016) 7035–7040.

[203] O. Kratky, G. Porod, Röntgenuntersuchung gelöster Fadenmoleküle, Recueil des Travaux Chimiques des Pays-Bas 68 (1949) 1106–1122.

[204] S. Goto, K. Kim, N. Matubayasi, Unraveling the Glass-like Dynamic Heterogeneity in Ring Polymer Melts: From Semiflexible to Stiff Chain, ACS Polym. Au 3 (2023) 437–446.

[205] I. Obayashi, T. Nakamura, Y. Hiraoka, Persistent Homology Analysis for Materials Research and Persistent Homology Software: HomCloud, J. Phys. Soc. Jpn. 91 (2022) 091013.

[206] M. Ceriotti, M. Parrinello, T. E. Markland, D. E. Manolopoulos, Efficient stochastic thermostatting of path integral molecular dynamics, J. Chem. Phys. 133 (2010) 124104.

List of Publications

Main papers:

1. N. Tomoshige*, S. Goto*, H. Mizuno, T. Mori, K. Kim, and N. Matubayasi, "Understanding the scaling of boson peak through insensitivity of elastic heterogeneity to bending rigidity in polymer glasses", *Journal of Physics: Condenced Matter*, **33** (27), 274002 (2021). https://doi.org/10.1088/1361-648x/abfd51

   *N. Tomoshige and S. Goto contributed equally to this work.

2. S. Goto, K. Kim, and N. Matubayasi, "Effects of chain length on Rouse modes and non-Gaussianity in linear and ring polymer melts", *The Journal of Chemical Physics*. **155** (12), 124901 (2021). https://aip.scitation.org/doi/10.1063/5.0061281

3. S. Goto, K. Kim, and N. Matubayasi, "Unraveling the Glass-like Dynamic Heterogeneity in Ring Polymer Melts: From Semiflexible to Stiff Chain", *ACS Polymers Au*. **3** (6), 437–446 (2023). https://doi.org/10.1021/acspolymersau.3c00013

4. S. Goto, T. Nakamura, D. Michieletto, K. Kim, and N. Matubayasi, "Persistent Homology Reveals the Origin of Topological Glasses in Ring Polymer Melts", arXiv:2411.10970 (2024), submitted to *Macromolecules*.

Acknowledgements

I would like to express my deepest gratitude to Professor Nobuyuki Matubayasi and Associate Professor Kang Kim for their invaluable guidance and support throughout my Ph.D. journey. I am grateful to Assistant Professor Kento Kasahara for his insightful comments and suggestions. I also acknowledge my colleague, Kazuya Okita, and all other members of Matubayasi laboratory for their friendship.

Special thanks are given to the following colleagues for discussions: Dr. Takenobu Nakamura, Professor Davide Michieletto, Mr. Naoya Tomoshige, Assistant Professor Hideyuki Mizuno, Assistant Professor Tatsuya Mori, Research Associate Professor Takuma Yagasaki, Dr. Kazuo Yamada, and Dr. Hidekazu Kojima. I was supported by the JST, the establishment of university fellowships towards the creation of science technology innovation, the Program for Leading Graduate Schools "Interactive Materials Science Cadet Program," and Sumitomo Chemical Co., Ltd. The numerical calculations were performed at the RIKEN Center for Computational Science, at the Research Center for Computational Science, Okazaki Research Facilities, National Institutes of Natural Sciences, and at the Cybermedia Center, Osaka University.

I would like to thank my wife and my family for their moral support and warm encouragement.

Finally, I dedicate this thesis to my unborn son. May it serve as a reminder that perseverance and curiosity can overcome any challenge. I eagerly await the day I can share my love of learning and discovery with you.

Shota Goto

Division of Chemical Engineering

Graduate School of Engineering Science

Osaka University, Toyonaka, Osaka 560-8531, Japan

Appendices

A Formulation of the Rouse model for ring polymer chain

In the Rouse model, the equation of motion for the polymer chain composed of N beads is given by the following Langevin equation:

$$\zeta \frac{d\boldsymbol{r}_n}{dt} = -k(2\boldsymbol{r}_n - \boldsymbol{r}_{n-1} - \boldsymbol{r}_{n+1}) + \boldsymbol{w}_n(t), \tag{A.1}$$

where $\boldsymbol{r}_n$ represents the coordinates of the n-th bead for $n = 1, 2, 3, \cdots, N$ and ζ denotes the effective hydrodynamic friction coefficient. Furthermore, two successive beads are connected by a harmonic spring with the modulus k. Here, the random force $\boldsymbol{w}_n$ acting on the bead is related to the temperature T and friction coefficient ζ by obeying the fluctuation-dissipation theorem:

$$\langle \boldsymbol{w}_n(t) \cdot \boldsymbol{w}_m(t') \rangle = 6k_{\mathrm{B}} T \zeta \delta_{nm} \delta(t - t'). \tag{A.2}$$

According to the statistical description for the freely-jointed chain model, the spring constant k is equal to $3k_{\mathrm{B}}T/b^2$ with the mean square distance b^2 between two beads. Note that the periodic boundary conditions

$$\boldsymbol{r}_0 = \boldsymbol{r}_N, \quad \boldsymbol{r}_{N+1} = \boldsymbol{r}_1 \tag{A.3}$$

should be imposed on the ring polymer chain. If we define two $N \times 3$ matrices, $\boldsymbol{R} = (\boldsymbol{r}_1, \boldsymbol{r}_2, \boldsymbol{r}_3, \cdots, \boldsymbol{r}_N)^{\mathrm{T}}$ and $\boldsymbol{W} = \zeta^{-1}(\boldsymbol{w}_1, \boldsymbol{w}_2, \boldsymbol{w}_3, \cdots, \boldsymbol{w}_N)^{\mathrm{T}}$ (the superscript T denotes the transpose), Eq.(A.1) can be expressed as

$$\frac{d\boldsymbol{R}}{dt} = -\frac{k}{\zeta}\boldsymbol{A}\boldsymbol{R} + \boldsymbol{W}, \tag{A.4}$$

with the matrix $N \times N$ $\boldsymbol{A}$:

$$\boldsymbol{A} = \begin{pmatrix} 2 & -1 & 0 & \cdots & 0 & 0 & -1 \\ -1 & 2 & -1 & \cdots & 0 & 0 & 0 \\ 0 & -1 & 2 & \cdots & 0 & 0 & 0 \\ 0 & 0 & -1 & \cdots & 0 & 0 & 0 \\ \vdots & & & \ddots & & & \vdots \\ 0 & 0 & 0 & \cdots & -1 & 2 & -1 \\ -1 & 0 & 0 & \cdots & 0 & -1 & 2 \end{pmatrix}. \tag{A.5}$$

Equation (A.4) can be solved by the diagonalization of the matrix $\boldsymbol{A}$. The eigenvalue λ equation is given as

$$(\boldsymbol{A} - \lambda \boldsymbol{E})\boldsymbol{F} = 0, \tag{A.6}$$

with the eigenvector $\boldsymbol{F} = (f_1, f_2, f_3, \cdots, f_N)^{\mathrm{T}}$ and the unit matrix $\boldsymbol{E}$. If the function form of f_n is assumed to be

$$f_n = z^n, \tag{A.7}$$

with the complex number z, Eq. (A.6) reduces to the following multiple linear equations:

$$(2 - \lambda)z - z^2 - z^N = 0, \tag{A.8}$$

$$\vdots$$

$$-z^{n-1} + (2 - \lambda)z^n - z^{n+1} = 0, \tag{A.9}$$

$$\vdots$$

$$-z - z^{N-1} + (2 - \lambda)z^N = 0. \tag{A.10}$$

From Eq. (A.9), the characteristic equation

$$-1 + (2 - \lambda)z - z^2 = 0, \tag{A.11}$$

is obtained. The two roots are denoted as z_1 and z_2, then

$$z_1 + z_2 = 2 - \lambda, \quad z_1 z_2 = 1. \tag{A.12}$$

Furthermore, the function form of z is assumed to be

$$z_1 = e^{i\theta}, \quad z_2 = e^{-i\theta} \tag{A.13}$$

such that $z_1 z_2 = 1$ with the imaginary unit i and an arbitrary argument θ in the complex plane. We obtain the identity:

$$e^{iN\theta} = 1 \tag{A.14}$$

to satisfy Eqs. (A.8), (A.9), and (A.10) in a consistent manner. The argument θ should be

$$\theta = \frac{2\pi p}{N}, \tag{A.15}$$

where p denotes the Rouse mode index with $p = 0, 1, 2, \cdots, N-1$. Thus, the eigenvalue of the mode p is obtained as

$$\lambda_p = 2 - (z_1 + z_2) = 2\left(1 - \cos\left(\frac{2\pi p}{N}\right)\right) = 4\sin^2\left(\frac{\pi p}{N}\right). \tag{A.16}$$

Note that $\lambda_p = \lambda_{N-p}$. Accordingly, the Rouse modes are symmetric with respect to the reflection at $p = N/2$ and the two modes of $p = n$ and $p = N - n$ are degenerate for ring polymers.

The general solution for the element of the eigenvector $\boldsymbol{F}$ can be given by

$$f_{n,p} = Ae^{in\theta} + A^* e^{-in\theta}, \tag{A.17}$$

with a complex constant A. Note that Eq. (A.17) ensures $f_{n,p} = f_{n,p}^*$, where the superscript * denotes

the complex conjugate. The orthogonal condition for $f_{n,p}$ is given by

$$\sum_{n=1}^{N} f_{n,p} f_{n,q}^{*} = \delta_{p,q}. \tag{A.18}$$

The l.h.s of Eq. (A.18) can be expressed as

$$\begin{aligned}\sum_{n=1}^{N} (Ae^{i2\pi np/N} + A^{*}e^{-i2\pi np/N}) \times (A^{*}e^{-i2\pi nq/N} + Ae^{i2\pi nq/N}) \\ = \sum_{n=1}^{N} \Big(A^{2}e^{i2\pi n(p+q)/N} + AA^{*}e^{i2\pi n(p-q)/N} \\ + A^{*}Ae^{-i2\pi n(p-q)/N} + (A^{*})^{2}e^{-i2\pi n(p+q)/N} \Big).\end{aligned} \tag{A.19}$$

To obtain the condition for determining A, we assume the special case $p + q = N$ ($p \neq q$); then, Eq. (A.19) further reduces to

$$\sum_{i=1}^{N} (A^{2} + (A^{*})^{2}), \tag{A.20}$$

where $\sum_{n=1}^{N} e^{i2n(p-q)/N} = 0$ is used. Thus, the first relationship $A^{2} + (A^{*})^{2} = 0$ is obtained from the orthogonal condition, Eq. (A.18). Furthermore, the normalization condition for $f_{n,p}$ is given by

$$\sum_{n=1}^{N} f_{n,p} f_{n,p}^{*} = 1, \tag{A.21}$$

which can be expressed at $p \neq 0$ or $N/2$ as

$$\sum_{n=1}^{N} \Big(A^{2}e^{i4\pi np/N} + 2AA^{*} + (A^{*})^{2}e^{-i4\pi np/N} \Big) \quad = \quad \sum_{i=1}^{N} 2AA^{*} \quad = \quad 1, \tag{A.22}$$

and the second relationship $AA^{*} = 1/(2N)$ is obtained. We again use $\sum_{i=1}^{N} e^{i4\pi np/N} = 0$ in the cases of $p \neq 0$ and $p \neq N/2$. Note that $AA^{*} = 1/(2N)$ is also obtained in the two cases $p = 0$ and $p = N/2$ according to $A^{2} + (A^{*})^{2} = 0$. From the two relationships, the complex constant A can be

determined, and its expression is chosen from four candidates: $A = (1+i)/(2\sqrt{N})$, $(-1-i)/(2\sqrt{N})$, $(-1+i)/(2\sqrt{N})$, and $(1-i)/(2\sqrt{N})$. The functional form of $f_{n,p}$ is then determined as

$$f_{n,p} = \sqrt{\frac{1}{N}}\left[\cos\left(\frac{2\pi np}{N}\right) + \sin\left(\frac{2\pi np}{N}\right)\right], \tag{A.23}$$

and Eq. (A.23) satisfies Eq. (A.18). Note that a different expression for $f_{n,p}$ is described and utilized in the path integral molecular dynamics. [206]

Here, we define the block matrix composed of the orthonormal eigenvectors, $\boldsymbol{U} = (\boldsymbol{U}_0, \boldsymbol{U}_1, \cdots, \boldsymbol{U}_{N-1})$, with $\boldsymbol{U}_p = (f_{1,p}, f_{2,p}, \cdots, f_{N,p})^{\mathrm{T}}$, which diagonalizes the matrix $\boldsymbol{A}$ as

$$\boldsymbol{U}^{\mathrm{T}}\boldsymbol{A}\boldsymbol{U} = \begin{pmatrix} \lambda_0 & 0 & \cdots & 0 \\ 0 & \lambda_1 & \cdots & 0 \\ \vdots & \vdots & \ddots & \vdots \\ 0 & 0 & \cdots & \lambda_{N-1} \end{pmatrix}. \tag{A.24}$$

The normal coordinates are finally described as

$$\boldsymbol{X} = \boldsymbol{U}^{\mathrm{T}}\boldsymbol{R}, \tag{A.25}$$

with the element

$$\boldsymbol{X}_p = \sqrt{\frac{1}{N}}\sum_{n=1}^{N} \boldsymbol{r}_n(t)\left[\cos\left(\frac{2\pi np}{N}\right) + \sin\left(\frac{2\pi np}{N}\right)\right], \tag{A.26}$$

for the ring polymer chain.

From Eq. (A.4), the normal coordinates of mode p obeys the following equation:

$$\frac{d\boldsymbol{X}_p}{dt} = -\frac{k}{\zeta}\lambda_p \boldsymbol{X}_p + \boldsymbol{W}_p, \tag{A.27}$$

where $\boldsymbol{W}_p = \boldsymbol{U}^{\mathrm{T}}\boldsymbol{W}$ is the random force, which satisfies

$$\langle \boldsymbol{W}_p(t) \cdot \boldsymbol{W}_q(t') \rangle = 6k_{\mathrm{B}}T\zeta^{-1}\delta_{p,q}\delta(t-t'). \tag{A.28}$$

The formal solution of Eq. (A.27) is given by

$$\boldsymbol{X}_p(t) = \boldsymbol{X}_p(0)\exp\left(-t/\tau_p\right) + \int_0^t dt' \boldsymbol{W}_p(t')\exp\left(-(t-t')/\tau_p\right), \tag{A.29}$$

where

$$\tau_p = \frac{\zeta}{k\lambda_p} = \frac{\zeta}{4k\sin^2\left(\frac{\pi p}{N}\right)} \tag{A.30}$$

represents the Rouse relaxation time. The autocorrelation function of $\boldsymbol{X}_p(t)$ is generally described by

$$\langle \boldsymbol{X}_p(t) \cdot \boldsymbol{X}_p(0) \rangle = \frac{3k_{\mathrm{B}}T}{k\lambda_p}\exp\left(-t/\tau_p\right). \tag{A.31}$$

The static correlation of the Rouse mode is expressed as

$$\langle \boldsymbol{X}_p(0)^2 \rangle = \frac{3k_{\mathrm{B}}T}{k\lambda_p} = \frac{b^2}{4\sin^2\left(\frac{\pi p}{N}\right)} \tag{A.32}$$

from the the initial value of Eq. (A.31).

B Persistent diagrams of ring polymers

Figures B1, B2, B3, and B4 present the probability density distributions of PD(i), PD($i \cup j$), and PD($j \to i$) at combinations of (ε_θ,ρ) = (1.5, 0.1), (1.5, 0.5), (5, 0.1), and (5, 0.5), respectively. The general shape of PD(i) remains consistent regardless of variations in density ρ or chain hardness ε_θ. The area with the highest frequency appears close to the diagonal with a prominent vertical distribution at $b \approx 0.22$. The distribution along the diagonal line represents loops that are formed and quickly disappear. These short-lived loops, characterized by small values of life l, are typically regarded as noise because they do not significantly contribute to threading structures. In contrast, the distribution along $b \approx 0.22$ is interpreted as loops generated by the inherent stiffness of the polymer chain backbone. Specifically, this value corresponds to the characteristic loop size related to the average bond length, $l_\mathrm{b} = 0.965 \approx 2\sqrt{0.22}$ of the KG model. The loops observed in the intermediate region, between the diagonal line and $b \approx 0.22$, are thought to be associated with secondary structures [202], such as the folding or compact configurations of ring polymers. These loops arise from internal conformational changes, bringing different parts of the polymer chain closer together, forming transient or quasi-stable folded structures. Unlike short-lived loops near the diagonal line, these intermediate loops contribute to the overall topological complexity of the system.

In the PD($i \cup j$), the distribution along the diagonal is more extended compared to that of PD(i). In addition, the intermediate distribution exhibits a more elongated shape. This is attributed to the creation of new loops caused by the contact between pairs of ring chains. These newly formed loops arise from the threading of ring chains, leading to an increase in the complexity of the structures, characterized by longer life l, due to the interaction between different chains. The distribution PD($j \to i$), representing the difference between PD(i) and PD($i \cup j$), does not exhibit significant changes compared to the shape of PD(i). This indicates that the loops of one ring polymer are significantly influenced by the threading interaction with other ring polymers. A detailed discussion regarding the chain stiffness ε_θ and density ρ is provided in the main text, where the analysis of the

zero-th and first Betti numbers offers further insights.

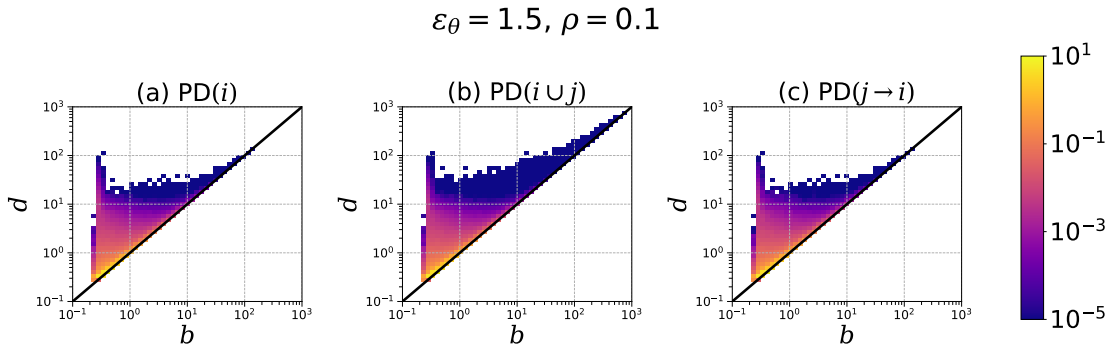

Figure B1: Persistent diagrams, PD(i) (a), PD($i \cup j$), and PD($i \to j$), with $\varepsilon = 1.5$ and $\rho = 0.1$.

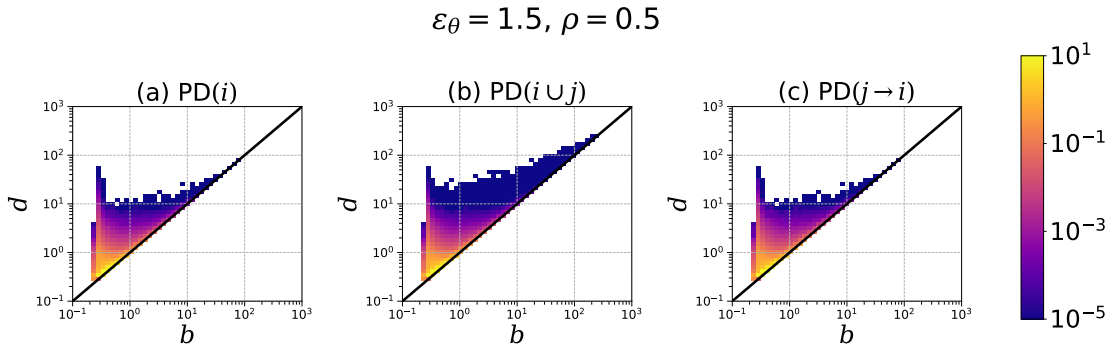

Figure B2: Persistent diagrams, PD(i) (a), PD($i \cup j$), and PD($i \to j$), with $\varepsilon = 1.5$ and $\rho = 0.5$.

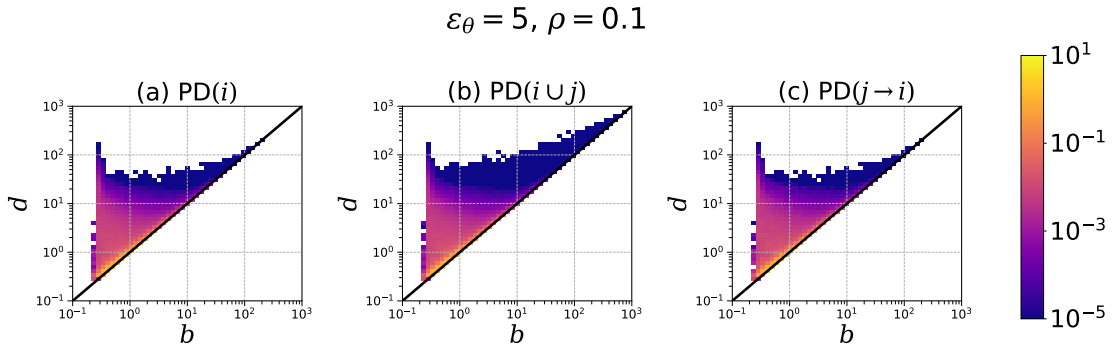

Figure B3: Persistent diagrams, PD(i) (a), PD($i \cup j$), and PD($i \to j$), with $\varepsilon = 5$ and $\rho = 0.1$.

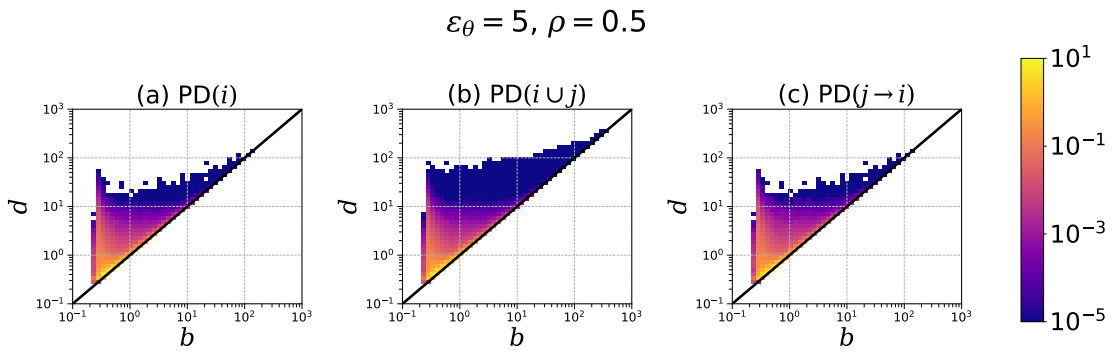

Figure B4: Persistent diagrams, PD(i) (a), PD($i \cup j$), and PD($i \to j$), with $\varepsilon = 5$ and $\rho = 0.5$.